

UNIVERSITÉ LIBRE DE BRUXELLES

**Losses of heat and particles in the
presence of strong magnetic field
perturbations**

IN CANDIDACY FOR THE DEGREE OF DOCTOR OF
PHILOSOPHY

Author:
Abhinav GUPTA

Supervisor:
Prof. Dr. Mikhail TOKAR

Performed at
Institut für Energieforschung-4, Forschungszentrum Jülich,
Germany

Abstract

Thermonuclear fusion has potential to offer an economically, environmentally and socially acceptable supply of energy. A promising reactor design to execute thermonuclear fusion is the toroidal magnetic confinement device, tokamak. The tokamak still faces challenges in the major areas which can be categorised into confinement, heating and fusion technology. This thesis addresses the problem of confinement, in particular the role of transport along magnetic field lines perturbed by diverse MHD instabilities.

Unstable modes such as ideal ballooning-peeling, tearing etc., break closed magnetic surfaces and destroy the axisymmetry of the magnetic configuration in a tokamak, providing deviation of magnetic field lines from unperturbed magnetic surfaces. Radial gradients of plasma parameters have nonzero projections along such lines and drive parallel particle and heat flows which contribute to the radial transport. Such transport can significantly affect confinement as this takes place by the development of neoclassical tearing modes (NTMs) in the core and edge localised modes (ELMs) at the plasma periphery.

In this thesis, transport of heat through non-overlapped magnetic island chains is first investigated using the 'Optimal path' approach, which is based on the principle of minimum entropy production. This model shows how the effective heat conduction through islands increases with parallel heat conduction and with the perturbation level. A more standard analytical approach for the limit cases of "small" and "large" islands is also presented. Transport of heat through internally heated magnetic islands is next investigated by further development of the 'Optimal path' method. In addition the approach by R. Fitzpatrick, has been extended for this investigation. By application of these approaches to experimental observations made at TEXTOR tokamak, heat flux limit, limiting parallel heat conduction in low collisional plasmas, is elucidated.

Models to study transport of heat and particles due to ELMs have also been developed. Energy losses during ELMs have been estimated considering contribution from parallel conduction due to electrons and parallel convection of ions, with constant level of the magnetic field perturbation, steady profiles for density and temperature, and by accounting for the heat flux limit. The estimate shows good agreement with experimental observations. The model is developed further by accounting for the time evolution of the perturbation level due to ballooning mode, and of density and temperature profiles.

Résumé

La fusion thermonucléaire a le potentiel d'offrir une source d'énergie économique, acceptable écologiquement et socialement. Une voie prometteuse est le dispositif de confinement magnétique toroïdal, ou tokamak. La faisabilité d'un réacteur de type tokamak fait encore face à des défis dans les domaines majeurs que sont le confinement, le chauffage et l'ingénierie. Cette thèse s'adresse à la problématique du confinement, en particulier au rôle du transport parallèle aux lignes de champ magnétique perturbées par des instabilités MHD.

Les modes instables tels que le ballooning-peeling, tearing etc..., détruisent les surfaces magnétiques et détruisent la symétrie axiale de la configuration tokamak, ce qui entraîne une déviation des lignes de champ magnétique. Les gradients radiaux des paramètres plasma ont alors des projections non nulles le long de ces lignes, ce qui entraîne la présence de flux parallèles de particules et de chaleur qui contribuent au transport radial. Ce transport peut affecter sensiblement le confinement, comme cela se produit lors du développement de modes tearing néoclassiques (NTMs) dans la zone de cœur et lors du développement d'instabilités de bord de type ELM à la périphérie.

Dans cette thèse, le transport de chaleur à travers les chaînes d'îlots magnétiques est d'abord étudié par l'approche de chemin optimal ("Optimal path"), qui est basée sur le principe de production d'entropie minimale. Ce modèle montre comment la conduction effective de chaleur à travers les îlots augmente avec la conduction parallèle de chaleur et avec l'amplitude de la perturbation. Une approche plus standard est aussi présentée pour les cas limites de "petits" et "grands" îlots. Le transport de chaleur à travers les îlots chauffés intérieurement est ensuite étudié par un raffinement de l'approche "Optimal path". L'approche de R. Fitzpatrick est aussi étendue à cet effet. En appliquant ces approches à des observations expérimentales effectuées sur le tokamak TEXTOR, la limite de flux de chaleur associée à la conduction de chaleur parallèle dans les plasmas peu collisionnels est estimée.

Des modèles sont aussi développés pour l'étude du transport de chaleur et de particules par ELMs. Des pertes d'énergie lors d'ELMs ont été estimées en considérant la contribution de la perte conductive parallèle due aux électrons et à la convection parallèle des ions, en considérant une perturbation constante du champ magnétique, des profils de densité et de température stationnaires, et en tenant compte de la limite de flux de chaleur. Les estimations sont en accord avec les observations expérimentales. Le modèle est ensuite étendu avec la prise en compte de l'évolution temporelle de la perturbation due au mode ballooning, ainsi que la prise en compte des profils de densité et de température.

Contents

1	Introduction	7
1.1	Why Fusion ?	7
1.2	Fusion in plasma	8
1.3	Tokamak	9
1.4	Thesis outline	11
1.4.1	Publications	12
2	Instabilities and transport	13
2.1	Plasma description	13
2.2	Instabilities	17
2.2.1	MHD equilibrium	17
2.2.2	MHD Stability	18
2.2.3	Peeling modes	20
2.2.4	Ballooning modes	21
2.2.5	Tearing modes	21
2.2.6	Drift waves	22
2.3	Transport	23
2.3.1	Drift motion	23
2.3.2	Classical and neoclassical transport	24
2.3.3	Transport due to instabilities	28
3	Magnetic islands	31
3.1	Magnetic island geometry	31
3.2	Fitzpatrick's model for transport through magnetic islands	35
3.3	Transport across non-overlapped islands	39
4	Transport from internally heated magnetic islands	45
4.1	Transport through heated magnetic islands	46
4.2	Extension of Fitzpatrick's model for heated magnetic islands	52
5	ELMs	57
5.1	Phenomenology and mechanisms	57
5.2	Theories	60
5.3	Model for ion convective heat loss during ELM crash	63
5.4	Model of the time variation of the field line inclination	68
5.5	0-D model for time evolution of all ETB parameters during elms	71

6	Summary	75
A	Magnetic islands	85
	A.1 Transport across non overlapped magnetic islands	85
B	Heat flux limit	87
	B.1 Transport through heated magnetic islands	87
	B.2 Extension of fitzpatrick's model	91
C	ELMs	97
	C.1 Discretized equations for the model of ion convective heat loss .	97
	C.1.1 Equations in dimensionless variables	97
	C.1.2 Profiles	98
	C.1.3 Electric field	98
	C.2 Discretized equations for time evolution of n, T and α_{elm}	99
	C.3 Simple model for ballooning modes	100
	C.3.1 Particle losses due to ballooning mode	104
	C.3.2 Averaging over poloidal angle	105

Chapter 1

Introduction

1.1 Why Fusion ?

The growing need for energy is a fact unknown to few. The exploitation of resources by developed countries and the desire to achieve a good living standard among the developing nations, requires energy sources of enormous potential.

The contribution of different energy sources to the primary energy production in the world are (in percentage) oil 40, coal 27, gas 21, fission 6 and hydroelectricity 6, approximately. The number of years of use, at the current rate of consumption, for coal is around 270, 40-50 for crude oil, 60-70 for natural gas, 40-50 for Uranium (2400-3000 if breeder technology is employed). We observe that 90 percent of our energy is currently produced by burning fossil fuel, this could pose serious problems in future due to their short span of usability. Other problems are environmental consequences of massive use of fossil fuels due to the gigantic release of carbon dioxide in the atmosphere.

Possible alternatives to burning fossil fuels are long term energy sources, namely renewables, fission and fusion. Methods for renewables are usage of photovoltaic panels, wind power plants and biomass. The natural obstacles are energy density and/or fluctuation in time. In the case of fission, highly radioactive waste is produced. Although considerable progress has been made in the safety and environmental aspects of producing energy from fission public non-acceptance poses problems that are potentially difficult to cope with.

Energy production must not be only economically, but also environmentally and socially acceptable. To be able to supply this energy, fusion is an option. It is characterised by exclusive properties, some of which represent distinct advantages over the other major energy sources. The properties can be grouped around three aspects: 1. Almost inexhaustible supply of cheap fuels, Deuterium and Lithium, that are widely abundant. 2. Fusion reactors offer inherent passive safety and are not based on chain reactions. 3. Fusion power is environmentally acceptable, no contribution to greenhouse effect, to acid rain and/or to the destruction of the ozone layer.

1.2 Fusion in plasma

Fusion reactions occur in stars where hydrogen and helium convert to heavier nuclei. The H and He nuclei are held together by gravity long enough for sufficient reactions to occur. For instance, in the core of the Sun the temperature is 10-15 million K , which along with the extreme pressure and density, allows matter to be converted into large amounts of energy.

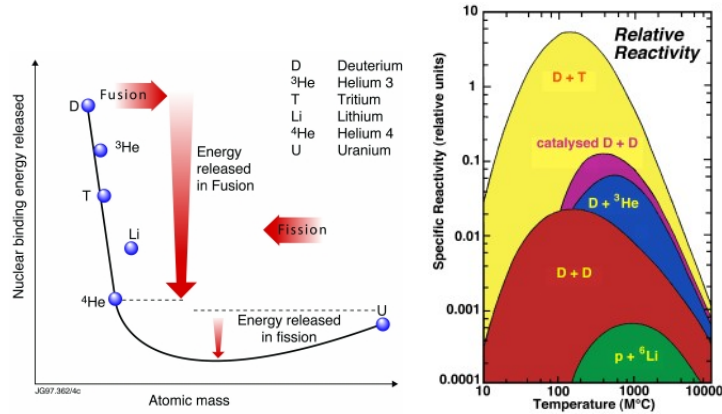
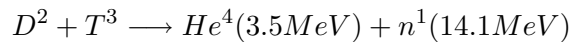


Figure 1.1: Fusion reaction (left), and relative reactivity of different reactants (right)

A figure of merit for a reaction is the 'reactivity' - the product of the probability of reaction and the energy delivered per reaction. This consideration shows, that the fusion reaction between deuterium (D) and tritium (T) has maximum reactivity at around 100 million K .



The next most reactive is D+D with a reactivity about 40 times smaller, and D+³He, an isotope of helium, with a reactivity about 85 times smaller fig. 1.1. In fusion reactions, since the nuclei are positively charged, the Coulomb force has to be overcome before the reactions can occur. The Coulomb potential energy to be overcome can be estimated as $E_{coul} = z_1 z_2 e^2 / 4\pi\epsilon_0 r_0$, where $z_1 e$, $z_2 e$ are the charges of the two nuclei and r_0 the collision radius. Consequently, the nuclei have to be accelerated to considerable energy in order to penetrate the Coulomb barrier. If for example a beam of deuterons from an accelerator is directed at a target of solid tritium or deuterium, most of the energy is lost in ionising and heating the target and in elastic collisions. The solution is to form a Maxwellian plasma in which fast particles in the tail of the distribution can undergo fusion. Elastic collisions do not change the distribution if it is Maxwellian, and the energy used to heat the plasma is retained until the particles react or escape from the chamber.

A plasma is a quasineutral gas of charged and neutral particles which exhibits collective behaviour [37]. A fundamental characteristic of plasma is

its ability to shield out electric potentials that are applied to it. The Debye length is a measure of the shielding thickness of the sheath (or charge cloud) formed around an electric field in a plasma. If the dimension L of a system is much larger than λ_D ($L \gg \lambda_D$), then local concentrations of charge or external potentials are shielded out in a distance short compared with L . The plasma is 'quasineutral' enough so that one can take $n_i = n_e = n$, where n is a common density called plasma density.

The picture of Debye shielding is valid only if there are enough particles in the charge cloud, hence in addition 'collective behaviour' requires $N_D \gg 1$, where $N_D = n\lambda_D^3/4/3$. Some ionised gases do not qualify as plasmas because the charged particles collide so frequently with neutral atoms that their motion is governed by ordinary hydrodynamic forces rather than by electromagnetic forces. If ν is the frequency of typical plasma oscillations and τ is the mean time between collisions with neutral atoms, we require $\nu\tau > 1$ for the gas to behave like a plasma.

The confinement of a high temperature plasma is extremely difficult and the plasma energy leaks out by various means, such as heat conduction, particle diffusion, radiation emission, etc. Suppose a plasma of temperature T and density n is maintained during a energy confinement time $\tau_E = W/E_l$ where W is the stored energy in the plasma, and fusion persists during that time. If we denote E_f as the energy produced by the nuclear reaction, E_l as the energy lost, ηE_f a fraction of energy confined to heat the plasma and $\eta' E_l$ a fraction collected and used to heat the plasma, then the condition for heating the plasma called the Lawson criteria, is given by $\eta E_f > (1 - \eta') E_l$. After certain assumptions it is more commonly estimated as a figure of merit

$$nT\tau_E > 5.10^{21} \text{ keVs/m}^3$$

Other important parameters are, beta $\beta = P/(B^2/2\mu_0)$ the ratio of the kinetic pressure to the magnetic pressure, and the Q-value $Q = E_f/E_l$ which gives a measure of the quality of the fuel.

1.3 Tokamak

The tokamak is a toroidal magnetic confinement device, the principal magnetic field is in the toroidal direction and is produced by coils wounded poloidally around the torus [45]. The charged particles experience a lorentz force $F_L = q(\mathbf{v} \times \mathbf{B} + \mathbf{E})$, where q and \mathbf{v} are the charge and velocity of the particle, and \mathbf{B} and \mathbf{E} are the magnetic and electric fields. In a magnetic field, $\mathbf{E} \approx 0$, the charged particles have a helical orbit, the particles gyrating about the guiding centre of their motion, the guiding centre moving along the magnetic field.

In presence of other forces, particles undergo a drift in the guiding centre motion, given by the drift velocity $\mathbf{v}_D = \mathbf{F} \times \mathbf{B}/qB^2$, where \mathbf{F} is the force in the direction perpendicular to \mathbf{B} (see section 2.3). In a tokamak the magnetic field lines are curved and in addition have a gradient with the field intensity dropping with the major radius R_0 . Both result in a force directed outwards

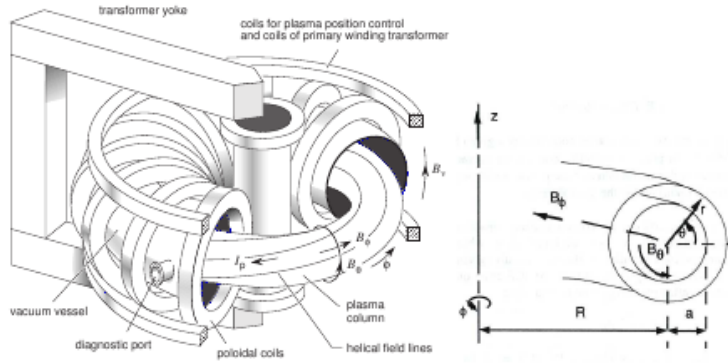


Figure 1.2: Tokamak

giving rise to a vertical drift $m(v_{\parallel}^2 + v_{\perp}^2)/qRB^2$, where m , v_{\parallel} and v_{\perp} are mass, parallel and perpendicular velocities, of the particle. The drifts are in different direction for electrons and ions, and produces a charge separation, the resulting electric field induces a horizontally directed $E \times B$ drift, $\mathbf{v}_E = \mathbf{E} \times \mathbf{B}/B^2$, driving an outgoing plasma flow. The $E \times B$ drift enhances the charge separation effectuating a 'interchange instability'.

The drift can be evaded by twisting the magnetic field lines helically, the particles moving along the field lines short-circuit the charge separation by Debye shielding, so that the electric field does not grow, whereby this 'interchange instability' is suppressed. The twist can be achieved by driving a current parallel to \mathbf{B} , generated by means of a transformer where the plasma is the secondary, inducing a poloidal magnetic field component B^{θ} which is typically an order of magnitude smaller than the toroidal component B^{φ} .

The resulting magnetic field line follows a helical path as it goes around the torus on associated magnetic surface of minor radius r . The safety factor is defined as $q = \Delta\varphi/\Delta\vartheta$, i.e. a ratio of the change in the toroidal angle to a change in the poloidal angle when following a field line. To estimate q the equation of the field line is used, $Rd\varphi/r d\vartheta = B^{\varphi}/B^{\theta}$, and thus one obtains an average $q = 1/2\pi \oint (rB^{\varphi}/RB^{\theta})d\vartheta$ for a magnetic field line. For a large aspect-ratio tokamak ($R/r > 1$), $q = rB^{\varphi}/R_0B^{\theta}$. On magnetic surfaces called resonant surfaces $q = m/n$, where m and n are integer numbers, and on such surfaces field lines close upon themselves after n toroidal revolutions corresponding to m poloidal revolutions, about the torus.

The helical field lines form closed flux surfaces which may be elliptical. The ellipticity is denoted by $\kappa = b/a$, where a is the minor radius of the plasma edge surface in the median plane, and b is its minor radius in the vertical direction. The shape is often more like a D, and such shapes may be characterised by an additional parameter, the triangularity δ .

There are various challenges to be faced in designing a fusion reactor, and some of them may be divided into three general areas namely plasma confinement, plasma heating and fusion technology. Confinement has to do with satisfying the Lawson criterion. Plasma heating is related to confinement

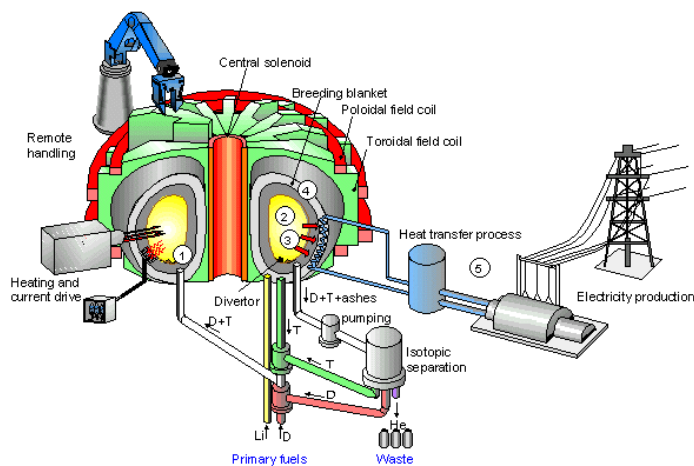


Figure 1.3: Tokamak Reactor

since even a slow heating process would be effective if confinement time was long. Fusion technology has to do with the engineering design of a reactor apart from the physics aspects. In addition are two subcategories plasma diagnostics and plasma purity.

The development of reactor levels of τ_e and β , are important for an attractive reactor. Equally critical are impurity minimisation and control, low recirculating power for plasma production and control, the development of radiation resistant, low-activation materials, and high reliability and maintainability.

The magnet coils are protected from nuclear radiation by a moderation of the neutrons (blanket) and by a shield which absorbs neutrons and gamma rays. In the case of D-T plasma, the blanket contains lithium to breed tritium to replace that burned in fusion reactions. In most configurations the outer magnetic flux surfaces are diverted onto targets, which absorb the heat, thus isolating most of the chamber wall from direct contact with the plasma. The first wall and the blanket and shield elements form a vacuum chamber. A coolant, liquid or gas, removes heat deposited to the wall, blanket, shields, and divertor targets and transports it to heat exchangers and generators which produce electricity.

1.4 Thesis outline

So long as the magnetic surfaces remain closed, transport is limited to classical, neoclassical and anomalous mechanisms (see section 2.3). But, diverse MHD instabilities such as ideal ballooning-peeling, tearing modes, etc. break closed magnetic surfaces and destroy the axisymmetry of the magnetic configuration in a tokamak. The resulting powerful transport along magnetic field lines can contribute essentially to particle and heat losses from the plasma and significantly affect confinement as this takes place by the development of

neoclassical tearing modes (NTMs) in the core [26] and edge localised modes (ELMs) at the plasma periphery [13]. Therefore the transport characteristics parallel to the magnetic field are very important for understanding and quantitative description of such phenomena. Parallel transport is also relevant for mechanisms of ELM mitigation with external magnetic field perturbations [64]. Investigation of such transport due to MHD instabilities, namely magnetic islands and ELMs, is the main consideration of this thesis.

In chapter 2 a theoretical basis for the description of plasma, instabilities and transport is given which assists in understanding the following chapters. In chapter 3 transport of heat originating from core plasma passing through magnetic islands is investigated using the 'Optimal path' approach, which is based on the principle of minimum entropy production. A more detailed analytical approach by R. Fitzpatrick [28] is also presented, which however is limited to the cases of large and small islands. In chapter 4 heat flux limit, limiting parallel heat conduction in low collisional plasmas is elucidated using the 'Optimal path' method, and is validated by making an extension of the approach by R. Fitzpatrick for the case of magnetic islands heated internally at the resonant surface. In chapter 5 models to study transport of heat and particles due to ELMs have been developed. In the end a summary of the thesis is presented.

1.4.1 Publications

- A. Gupta, M. Tokar, *Heat conduction in a configuration with non-overlapped magnetic islands*, Physics of Plasmas **15**, 034503 (2008)
- A. Gupta, M. Tokar, *A model for energy losses by type-I ELMs*, 35th EPS Conference on Plasma Physics, P1.011 (2008)
- M. Tokar, A. Gupta, *Elucidation of heat-flux limit from magnetic-island heating*, Phys. Rev. Lett., **99**, 225001 (2007)
- M. Tokar, A. Gupta et al, *A model for particle and heat loss by type-I ELMs*, Plasma Phys. Control. Fusion **49**, 395 (2007)
- M. Tokar, T.E. Evans, A. Gupta et al, *Mechanisms of ELMs mitigation by external magnetic field perturbations*, Phys. Rev. Lett., **98**, 095001 (2007)
- M. Tokar, T.E. Evans, A. Gupta et al, *Modelling of pedestal transport during ELMs suppression by external magnetic field perturbations*, Nuclear Fusion, **48**, 024006 (2008)

Chapter 2

Instabilities and transport

2.1 Plasma description

In the description of plasma we restrict ourselves primarily to plasma consisting of charged particles which can be represented by point charge and point mass. Each particle is assumed to obey the classical nonrelativistic equations of motion and the plasma has no net charge, namely there are equal number of negative and positive charges.

The most detailed description is to follow the motion of each constituent particle, including the mutual interactions with other particles. In this description the plasma is represented by a distribution function in Γ -space (the phase space of all the particles) and the electromagnetic fields of all the particles. The system of equations corresponding to such a description is called the Klimontovich system of equations [2]. Consider an sth species of particles ($s = e$ for electron and i for ion) and let the number of such particles in the spatial region $\mathbf{r} \sim \mathbf{r} + d\mathbf{r}$ and the velocity region $\mathbf{v} \sim \mathbf{v} + d\mathbf{v}$ at time t be $\hat{f}_s(\mathbf{r}, \mathbf{v}, t)d^3\mathbf{r}d^3\mathbf{v}$. The volume element is chosen sufficiently small such that only one particle or less can exist inside it, that is, it is a δ function. Let there be a total of N_s particles and let the position and velocity of the jth particle at time t be $\mathbf{r}_j(t)$ and $\mathbf{v}_j(t)$, then the distribution function \hat{f}_s can be written as

$$\hat{f}_s(\mathbf{r}, \mathbf{v}, t) = \sum_{j=1}^{N_s} \delta[\mathbf{r} - \mathbf{r}_j(t)]\delta[\mathbf{v} - \mathbf{v}_j(t)] \quad (2.1)$$

Differentiate with respect to time, where $d\mathbf{r}_j/dt = \mathbf{v}_j$ and $d\mathbf{v}_j/dt = [\hat{\mathbf{E}}(\mathbf{r}_j, t) + \mathbf{v}_j \times \hat{\mathbf{B}}(\mathbf{r}_j, t)]q_s/m_s \equiv \hat{\mathbf{k}}_s(\mathbf{r}, \mathbf{v}, t)$, here q_s, m_s are the charge and mass of the sth species of particle and the hat stands for microscopic quantities, implying that the fields produced by point charges, as well as external fields are included. Summing up over j , i.e. all the particles, one obtains

$$\frac{\partial \hat{f}_s}{\partial t} + \mathbf{v} \cdot \frac{\partial \hat{f}_s}{\partial \mathbf{r}} + \hat{\mathbf{k}}_s(\mathbf{r}, \mathbf{v}, t) \cdot \frac{\partial \hat{f}_s}{\partial \mathbf{v}} = 0 \quad (2.2)$$

The electromagnetic fields $\hat{\mathbf{E}}$ and $\hat{\mathbf{B}}$ satisfy Maxwell's equations:

$$\begin{aligned}\nabla \times \hat{\mathbf{E}}(\mathbf{r}_j, t) &= -\frac{\partial \hat{\mathbf{B}}(\mathbf{r}_j, t)}{\partial t} & \nabla \cdot \hat{\mathbf{E}}(\mathbf{r}_j, t) &= \frac{\hat{\sigma}_e(\mathbf{r}_j, t)}{\epsilon_0} \\ \nabla \times \hat{\mathbf{B}}(\mathbf{r}_j, t) &= -\frac{1}{c^2} \frac{\partial \hat{\mathbf{E}}(\mathbf{r}_j, t)}{\partial t} + \mu_0 \hat{\mathbf{J}}(\mathbf{r}_j, t) & \nabla \cdot \hat{\mathbf{B}}(\mathbf{r}_j, t) &= 0\end{aligned}\quad (2.3)$$

where $\hat{\mathbf{J}}$ and $\hat{\sigma}_e$ are the microscopic current density and charge density and are given in terms of \hat{f}_s as

$$\begin{aligned}\hat{\mathbf{J}}(\mathbf{r}_j, t) &= \sum_s q_s \int \mathbf{v} \hat{f}_s(\mathbf{r}, \mathbf{v}, t) d^3\mathbf{v} \\ \hat{\sigma}_e(\mathbf{r}_j, t) &= \sum_s q_s \int \hat{f}_s(\mathbf{r}, \mathbf{v}, t) d^3\mathbf{v}\end{aligned}\quad (2.4)$$

The above equations (2.2,2.3,2.4) constitute the Klimontovich system of equations. Given the particle distribution \hat{f}_s , it determines $\hat{\mathbf{J}}$ and $\hat{\sigma}_e$ which in turn determine $\hat{\mathbf{E}}$ and $\hat{\mathbf{B}}$; the acceleration $\hat{\mathbf{k}}_s$ is then expressed in terms of \hat{f}_s which has to satisfy (2.2) for self-consistency. The solution of Klimontovich system of equations depends on the $6N$ ($N = \sum_s N_s$) initial parameters $[\mathbf{r}_j, \mathbf{v}_j]$, which is impossible to know. Although these equations can completely describe the plasma, the direct information given by such description is often useless because of the details it contains.

A more useful description which treats the plasma as phase space continuum, is the μ -space description where a single particle phase space distribution is used to describe the behaviour in the presence of an averaged electromagnetic field consistent with the continuum particle distribution. In this case we can either include the collisional effect (Boltzmann equation) or neglect it (Vlasov or collisionless Boltzmann equation). In the presence of a strong magnetic field, we can further simplify the equation by considering only the time-averaged guiding centre motion (drift-kinetic equation). The μ -space description can be obtained from the Γ -space Klimontovich equations by averaging their solutions over the ensemble of initial parameters. The resulting distribution function and the field variables then become smooth functions of \mathbf{r} and \mathbf{v} . The equations (2.3, 2.4) can be averaged, with same form of the equations holding for the averaged quantities as they are linear with respect to the quantities with hats. However because of its non-linearity, taking the average of (2.2) we have

$$\frac{\partial f_s}{\partial t} + \mathbf{v} \cdot \frac{\partial f_s}{\partial \mathbf{r}} + \langle \hat{\mathbf{k}}_s \cdot \frac{\partial \hat{f}_s}{\partial \mathbf{v}} \rangle = 0 \quad (2.5)$$

The last term differs from $\mathbf{k}_s \cdot \frac{\partial f_s}{\partial \mathbf{v}}$. The difference $\langle \hat{\mathbf{k}}_s \cdot \frac{\partial \hat{f}_s}{\partial \mathbf{v}} \rangle_{corr} \equiv \langle \hat{\mathbf{k}}_s \cdot \frac{\partial \hat{f}_s}{\partial \mathbf{v}} \rangle - \mathbf{k}_s \cdot \frac{\partial f_s}{\partial \mathbf{v}}$, which is called two-body correlation term or the term representing the discreteness effect of the plasma. The ideal plasma is a continuum in phase space and has no discrete properties, hence, the two body correlation effect is

totally negligible when compared with the effect of the average electromagnetic field. The resulting system of equations is the same as (2.2, 2.3 and 2.4), with the hats removed, and are called the Vlasov system of equations or the collisionless Boltzmann equations.

The most widely used description is similar to that of an ordinary macroscopic fluid. Here the plasma is represented by a continuum in real space and only the macroscopic quantities such as density, fluid velocity, temperature, and the electromagnetic fields consistent with the macroscopic variables are used to describe the plasma behaviour. There are two types of macroscopic descriptions: one is to treat the plasma as a two-component fluid consisting of an electron fluid and an ion fluid, and the other is to treat it as a one-component fluid by assuming local charge neutrality. The former is useful to derive the electrostatic response of a plasma, whereas the latter, usually called the magnetohydrodynamic (MHD) model, can describe a plasma in the presence of a strong inhomogeneous magnetic field.

The distribution function describing the dynamics of charged particles in phase space (μ -space) is given by $f_s(\mathbf{r}, \mathbf{v}, t)$. A macroscopic (fluid) description of the plasma can be obtained by integration of f_s , and its various moments with respect to \mathbf{v} , over the velocity space. The zeroth moment yields the density

$$n_s(\mathbf{r}, t) = \int f_s(\mathbf{r}, \mathbf{v}, t) d^3\mathbf{v} \quad (2.6)$$

the first moment gives the mean velocity

$$\bar{\mathbf{v}}_s(\mathbf{r}, t) = \frac{1}{n_s} \int \mathbf{v} f_s(\mathbf{r}, \mathbf{v}, t) d^3\mathbf{v} \quad (2.7)$$

the second moment leads to the pressure tensor

$$\overleftrightarrow{\mathbf{P}}_s(\mathbf{r}, t) = m_s \int \tilde{\mathbf{v}} \tilde{\mathbf{v}} f_s(\mathbf{r}, \mathbf{v}, t) d^3\mathbf{v} \quad (2.8)$$

and the third moment provides the heat flux density

$$\mathbf{q}_{H,s}(\mathbf{r}, t) = \frac{m_s}{2} \int \tilde{\mathbf{v}} \tilde{\mathbf{v}} \tilde{\mathbf{v}} f_s(\mathbf{r}, \mathbf{v}, t) d^3\mathbf{v} \quad (2.9)$$

with m_s the particle mass and $\tilde{\mathbf{v}} = \mathbf{v} - \mathbf{v}_s$. The pressure tensor can be written in the form $\overleftrightarrow{\mathbf{P}}_s = p_s + \overleftrightarrow{\boldsymbol{\pi}}_s$, where p_s is the scalar pressure and $\overleftrightarrow{\boldsymbol{\pi}}_s$ is the stress tensor, with zero trace. The time variation of f_s is given by the kinetic equation (Boltzmann):

$$\frac{\partial f_s}{\partial t} + \mathbf{v} \cdot \frac{\partial f_s}{\partial \mathbf{r}} + F_s \cdot \frac{\partial f_s}{\partial \mathbf{v}} = C_s \quad (2.10)$$

The term $C_s(\mathbf{r}, \mathbf{v}, t)$ accounts for sources and sinks of particles and for collisions with other species. $F_s(\mathbf{r}, \mathbf{v}, t)$ is the external force acting on particles, excluding collisions. An integration of 2.10 over the velocity space leads to the mass conservation equation:

$$\frac{\partial n_s}{\partial t} + \nabla \cdot \Gamma_s = S_s \quad (2.11)$$

where $S_s(\mathbf{r}, t)$ contains the source and sink terms. The $m_s \mathbf{v}$ moment of 2.10, gives the momentum equation:

$$\rho_s \frac{d\bar{\mathbf{v}}_s}{dt} = n_s q_s (\mathbf{E} + \bar{\mathbf{v}}_s \times \mathbf{B}) - \nabla \cdot \mathbf{P}_s + \mathbf{R}_s \quad (2.12)$$

where \mathbf{F}_s is the lorentz force, \mathbf{R}_s is the force due to collisions with other species, and $\rho_s = m_s n_s$. The $m_s v^2$ moment of 2.10, leads to the heat balance:

$$\frac{3}{2} n_s \frac{dT_s}{dt} + p_s \nabla \cdot \bar{\mathbf{v}}_s + \nabla \cdot q_{H,s} + \mathbf{P}_s : \nabla \bar{\mathbf{v}}_s = Q_{H,s} \quad (2.13)$$

where $Q_{H,s} = 1/2 \int m v^2 C_s d^3 \mathbf{v}$ is the heat generated in a gas of particles of species s by collisions with particles of other species. Hereafter the distribution function is assumed to be locally Maxwellian:

$$f_s(\mathbf{r}, \mathbf{v}) = n_s(\mathbf{r}) \left[\frac{m_s}{2\pi T_s(\mathbf{r})} \right]^{3/2} \exp \left\{ -\frac{m_s [\mathbf{v} - \bar{\mathbf{v}}_s(\mathbf{r})]^2}{2T_s(\mathbf{r})} \right\} \quad (2.14)$$

by substituting 2.14 in 2.8, the pressure tensor becomes isotropic and corresponds to a scalar pressure $P_s = n_s T_s$. We proceed to obtain the one-fluid MHD equations from the above set of two-fluid equations, and hereafter denote $\bar{\mathbf{v}}_s$ by \mathbf{u}_s . Summing the electron and ion continuity equations (2.11):

$$\frac{\partial \rho}{\partial t} + \nabla \cdot (\rho \mathbf{u}) = S \quad (2.15)$$

where $\rho = \rho_i + \rho_e \approx \rho_i$, $\mathbf{u} = (\mathbf{u}_i \rho_i + \mathbf{u}_e \rho_e) / \rho \approx \mathbf{u}_i$, and S is the source term. When the collisional momentum exchange is considerable $\mathbf{R}_e = -\mathbf{R}_i$, where $\mathbf{R}_e = -n_e m_e (\mathbf{u}_e - \mathbf{u}_i) / \tau_{ei}$, here τ_{ei} is the collision time between electron and ion. Neglecting the electron inertia term ($\rho_e d\mathbf{u}_e / dt \ll \rho_i d\mathbf{u}_i / dt$), combining the equations of motion for electrons and ions (2.12) we get momentum conservation, and the electrons motion equation gives the ohm's law:

$$\rho \frac{d\mathbf{u}}{dt} = -\nabla P + \sigma_e \mathbf{E} + \mathbf{J} \times \mathbf{B} \quad (2.16)$$

$$\mathbf{E} + \mathbf{u} \times \mathbf{B} = \frac{1}{en} (\mathbf{J} \times \mathbf{B} - \nabla P_e + \mathbf{R}) \quad (2.17)$$

where $\sigma_e = -en_e + Zen_i$, $\mathbf{J} = -en_e \mathbf{u}_e + Zen_i \mathbf{u}_i$, $P = P_e + P_i$ and $\mathbf{R} = en\eta \mathbf{J}$, here $\eta = m_e / n_e^2 \tau_{ei}$ is the resistivity. Assumption of an adiabatic fluid and adding up the adiabatic laws ($d(P_s n_s^{-\gamma}) / dt = 0$) for electrons and ions gives for the energy conservation:

$$\frac{d(Pn^{-\gamma})}{dt} = 0 \quad (2.18)$$

The resistive one fluid MHD equations are closed with the equations (2.15, 2.16, 2.17, 2.18) and the Maxwell equations for averaged electromagnetic fields:

$$\begin{aligned}\nabla \times \mathbf{E} &= -\frac{\partial \mathbf{B}}{\partial t} & \nabla \cdot \mathbf{E} &= \frac{\sigma_e}{\epsilon_0} \\ \nabla \times \mathbf{B} &= -\frac{1}{c^2} \frac{\partial \mathbf{E}}{\partial t} + \mu_0 \mathbf{J} & \nabla \cdot \mathbf{B} &= 0\end{aligned}\quad (2.19)$$

One fluid MHD neglecting resistivity is called the ideal MHD. In the Ohm's law 2.17, when the current drift velocity $\mathbf{u}_d = \mathbf{J}/en$ is much smaller than \mathbf{u} , and $\beta_e = nT_e/(B^2/2\mu_0) < 1$, the right hand side is left with $\eta\mathbf{J}$, which is further neglected in the ideal MHD. To determine \mathbf{J} , the amperes law is used, where the displacement current is neglected, which is valid for $u^2/c^2 \ll 1$. The term $\sigma_e E$ is assumed to be negligibly small in 2.16. Then the ideal MHD equations are

$$\begin{aligned}\frac{\partial \rho}{\partial t} + \nabla \cdot (\rho \mathbf{u}) &= 0 & \rho \frac{d\mathbf{u}}{dt} &= -\nabla P + \mathbf{J} \times \mathbf{B} \\ \frac{d(Pn^{-\gamma})}{dt} &= 0 & \mathbf{E} &= -\mathbf{u} \times \mathbf{B} \\ \nabla \times \mathbf{E} &= -\frac{\partial \mathbf{B}}{\partial t} & \nabla \times \mathbf{B} &= \mu_0 \mathbf{J}\end{aligned}\quad (2.20)$$

Though ideal MHD does not include kinetic effects, it is the simplest and the most useful theory to describe plasmas confined by a magnetic field.

2.2 Instabilities

2.2.1 MHD equilibrium

MHD equilibrium is defined by a stationary state without plasma flow, i.e., $\partial/\partial t = 0$ and $\mathbf{u}_0 = 0$. Then the ideal MHD equation for force balance (2.20) gives:

$$\nabla P = \mathbf{J} \times \mathbf{B} \quad (2.21)$$

From 2.21 we have $\mathbf{B} \cdot \nabla P = 0$ and $\mathbf{J} \cdot \nabla P = 0$, which means that magnetic field lines and current stay on isobaric surfaces. To calculate the magnetic configuration in a tokamak it is useful to introduce the poloidal flux function $\Psi = \int_S \mathbf{B}^\theta \cdot d\mathbf{S}$. It describes the poloidal flux per radian toroidal angle φ through a surface going from the magnetic axis to a point (z, r) . The axisymmetry imposes $\partial/\partial \varphi = 0$. The definition of the flux function and the right-handed cylindrical coordinate system (r, φ, z) allows us to write the magnetic field as

$$\mathbf{B} = \frac{\nabla \Psi \times \mathbf{e}^\varphi}{r} + B^\varphi \mathbf{e}_\varphi \quad \Leftrightarrow \quad B^r = -\frac{\partial \Psi}{r \partial z}, B^z = \frac{\partial \Psi}{r \partial r} \quad (2.22)$$

Substitution of 2.22 in $\mathbf{B} \cdot \nabla P = 0$ leads to $\nabla \Psi \times \nabla P = 0$, which implies $\Psi = \Psi(p)$ or $p = p(\Psi)$. The latter form states that pressure is a flux function. Defining $f = rB^\varphi$ and using Amperes law 2.20, \mathbf{J} can be written as

$$\mathbf{J} = \frac{\nabla f \times \mathbf{e}^\varphi}{\mu_0 r} + J^\varphi \mathbf{e}_\varphi \quad \Leftrightarrow \quad J^r = -\frac{\partial f}{\mu_0 r \partial z}, J^z = \frac{\partial f}{\mu_0 r \partial r} \quad (2.23)$$

Substituting 2.23 in $\mathbf{J} \cdot \nabla P = 0$ gives $\nabla f \times \nabla P = 0$, thus $f = f(p)$ and using $p = p(\Psi)$, it follows that $f = f(\Psi)$ is a flux function as well. Including 2.22 and 2.23 in the force balance equation 2.21, we end up with a partial differential equation describing equilibrium, the Grad-Shafranov equation:

$$r \frac{\partial}{\partial r} \left(\frac{\partial \Psi}{r \partial r} \right) + \frac{\partial^2 \Psi}{\partial z^2} = -\mu_0 r^2 \frac{dp}{d\Psi} - f \frac{df}{d\Psi} \quad (2.24)$$

This equation has three variables ψ, f, p corresponding to $\mathbf{B}, \mathbf{J}, p$ so that two of the three variables should be known in order to resolve the third one. In reality real estimates are taken for $p, \mathbf{J}, \mathbf{B}$, based on measurements of density, temperature, the external- \mathbf{B} fields and q . In an iterative process $p, \mathbf{J}, \mathbf{B}$ subsequently converge to a self-consistent solution. As a result one gets the total magnetic equilibrium field within the plasma, the current density profile, and the pressure p as a flux function. The solutions show that magnetic flux surfaces are nested, and the magnetic axis is shifted from the axis of the plasma, the so called Shafranov shift [3].

2.2.2 MHD Stability

Equilibrium means that all forces in the system are balanced. However, it does not guarantee that the system will return to the equilibrium state if it is perturbed. In a stability analysis of a plasma, the plasma is assumed to be in equilibrium, and it is disturbed by a small perturbation. The stability of the plasma is determined by its response to the perturbation. If the perturbation grows, the plasma is unstable. If the perturbation decays or leads to non-growing oscillations near the equilibrium, the plasma is stable for given perturbation. Only if the plasma is stable against all possible perturbations, it can be considered stable.

In the linear analysis, the equilibrium quantities, by definition, do not depend on time and the perturbed quantities are time dependent. In this analysis a quantity can be written as $Q(\mathbf{r}, t) = Q_0(\mathbf{r}) + Q_1(\mathbf{r}, t)$, here $Q_1/Q_0 \ll 1$, where the subscripts 0, 1 represent the equilibrium and the perturbed part, respectively. All second order terms $Q_1(\mathbf{r}, t) \cdot Q_1(\mathbf{r}, t)$ are considered small enough to be neglected.

If the displacement of the plasma is denoted by $\xi(\mathbf{r}, t)$ then the perturbed velocity is $\mathbf{v}_1 = \partial \xi / \partial t$. The force and the energy change due to the displacement can be written as:

$$\mathbf{F} = \mathbf{J}_0 \times \mathbf{B}_1 + \mathbf{J}_1 \times \mathbf{B}_0 - \nabla p_1 \quad \delta W = -\frac{1}{2} \int \xi \cdot \mathbf{F} d\mathbf{r} \quad (2.25)$$

From the ideal MHD equations (2.20), linearised with respect to the perturbation and the Amperes law taken into account, one gets:

$$p_1 = -\xi \cdot \nabla p_0 - \gamma p_0 \nabla \cdot \xi \quad \mathbf{B}_1 = \nabla \times (\xi \times \mathbf{B}_0) \quad (2.26)$$

$$\mathbf{J}_1 = \nabla \times \mathbf{B}_1 / \mu_0 \quad (2.27)$$

Thus the force operator can be written as:

$$\mathbf{F} = \frac{1}{\mu_0} (\nabla \times \mathbf{B}_0) \times \mathbf{B}_1 + \frac{1}{\mu_0} (\nabla \times \mathbf{B}_1) \times \mathbf{B}_0 + \nabla (\xi \cdot \nabla p_0 + \gamma p_0 \nabla \cdot \xi) \quad (2.28)$$

Equation 2.28 can be used to determine how the plasma state develops in time for a given perturbation, but to test the plasma response to all possible perturbations is very difficult and better methods have to be used [18].

The linear stability can be studied by assuming that the instabilities grow exponentially. All perturbations, and consequently the perturbed momentum equation can be written as:

$$Q_1(\mathbf{r}, t) = Q_1(\mathbf{r}) e^{-i\omega t} \quad -\omega^2 \rho_0 \xi = \mathbf{F}(\xi) \quad (2.29)$$

Equation 2.29 is an eigenvalue problem for the eigenvalue ω^2 . The sign of ω^2 determines the stability of the plasma. If ω^2 is positive, the plasma displacement and the resulting force counter each other, which means that the plasma remains stable. However, if ω^2 is negative the plasma displacement and the resulting force grow together, thus the plasma is unstable.

It can be shown that the energy principle can be applied to investigate stability of a ideal plasma [1]. The change in potential energy associated with a perturbation ξ , can be found from substitution of 2.28 in 2.25, along with application of suitable vector relations together with Gauss's theorem:

$$\begin{aligned} \delta W = \frac{1}{2} \int \left(\frac{B_1^2}{\mu_0} + \gamma p_0 (\nabla \cdot \xi)^2 + (\xi \cdot \nabla p_0) \nabla \cdot \xi - \mathbf{J}_0 \cdot (\mathbf{B}_1 \times \xi) \right) d\mathbf{r} \quad (2.30) \\ + \frac{1}{2} \int \left(p_1 + \frac{\mathbf{B}_0 \cdot \mathbf{B}_1}{\mu_0} \right) \xi \cdot d\mathbf{S} \end{aligned}$$

The stability of the plasma can be determined from the change of potential energy δW . Since the energy is conserved, a negative change of the potential energy corresponds to a positive change in the plasma kinetic energy, which corresponds to a unstable situation. If there exists any (allowable) perturbation that makes δW negative the plasma is unstable. So, in order to know the stability of the plasma, $\delta W(\xi)$ is minimised with respect to ξ , and the plasma is stable if $\delta W(\xi)_{min} \geq 0$.

In 2.30 the surface term is zero if the normal displacement at the surface is zero, as it would be at a perfect conductor. When there is a vacuum region outside the plasma the surface term represents the transfer of energy to the vacuum region, and can be written as:

$$\delta W_v = \frac{1}{2} \int_{vac} \frac{B_1^2}{\mu_0} \quad (2.31)$$

The vacuum term is always positive definite and thus stabilising. If there are no currents at the boundary, all potentially destabilising terms are included in the plasma term, which written in an intuitive form [7] is:

$$\delta W_p = \frac{1}{2} \int_{plasma} \left[\frac{B_{1,\perp}^2}{\mu_0} + \frac{B_0^2}{\mu_0} |\nabla \cdot \xi_\perp + 2\xi_\perp \cdot \kappa|^2 + \gamma p_0 (\nabla \cdot \xi)^2 \right. \quad (2.32) \\ \left. - 2(\xi_\perp \cdot \nabla p_0)(\kappa \cdot \xi_\perp^*) - J_\parallel (\xi_\perp^* \times \mathbf{b}) \cdot \mathbf{B}_{1,\perp} \right] d\mathbf{r}$$

where $\mathbf{b} = \mathbf{B}/B$, and $\kappa = \mathbf{b} \cdot \nabla \mathbf{b}$ is the curvature of the magnetic field. The first term is the energy required to bend the magnetic field lines, the second term is the energy required to compress the magnetic field and the third term is the compressional energy of the plasma. These three terms are stabilising. The last two terms can be destabilising. Instabilities caused by the fourth term are called pressure driven modes, because ∇p is the source of free energy. The last represents current driven modes, where J_\parallel is the source of free energy.

A hot plasma, with a large current running through it, is a large source of free energy. If the confinement of the plasma is lost, this energy is deposited onto the walls of the device in a very short time and can cause serious damage. Therefore, it is very important to keep the plasma stable so that a small perturbation from the equilibrium does not lead to a complete loss of confinement, a so-called disruption. Instabilities whose growth can be limited to a small region of the plasma can be tolerated in the plasma operation. They increase the transport of particles and energy out of the plasma, but do not lead to a catastrophic end of a discharge. While the increase of energy transport always degrades the plasma confinement, sometimes the increase in particle transport can be beneficial, for instance, to remove helium ash from the plasma. Increased transport due to small instabilities can also prevent other more destructive instabilities from developing. Examples of such non-catastrophic MHD instabilities are neo-classical tearing modes (NTMs) [19] and edge localised modes (ELMs) [30]. In the following sections instabilities relevant to the work of this thesis are discussed briefly, a detailed discussion is beyond the scope of this thesis. Coupled Peeling-Ballooning modes are widely considered to be responsible for ELMs. Tearing modes lead to the development of magnetic islands. Drift waves are one of the most important mechanisms responsible for anomalous transport.

2.2.3 Peeling modes

Peeling modes are kink-type instabilities occurring in the edge region of the plasma [11]. The destabilising energy comes from the last term of 2.32, and therefore the peeling modes are current driven. The peeling modes have typically low or intermediate toroidal mode numbers $n = 1 - 10$. The poloidal number depends on the rational surface at which the peeling mode is localised, so that $q = m/n$. Due to the low mode number, the wavelength is long. In a peeling mode the edge plasma peels off from the rest of the plasma.

From the fourth term of 2.32, one sees that if the average curvature ($\int[(\mathbf{b} \cdot \nabla \mathbf{b}) \cdot \nabla p] d\mathbf{r} < 0$) on a flux surface is favourable, the pressure gradient has a stabilising effect on the peeling modes because there is little variation in ξ with the poloidal angle due to the long wavelength. In the H-mode plasma, steep pedestal pressure gradient drive bootstrap current, causing large localised current density at the edge than in the surrounding plasma, and thus the instability is localised at the edge. Increased transport, flattens the pressure profile, thus edge current density gradient decreases until the plasma is stabilised again.

2.2.4 Ballooning modes

The ballooning modes are pressure-driven instabilities that can occur in a toroidal device. The destabilising energy comes from the fourth term of 2.32. The modes are localised to the region of unfavourable curvature ($(\mathbf{b} \cdot \nabla \mathbf{b}) \cdot \nabla p > 0$) in order to minimise the stabilising effect of the favourable curvature. In order to be localised on the unfavourable curvature region, the amplitude variation along the field line must be maximised. Therefore, the most unstable ballooning modes have high toroidal mode numbers [12]. The mode structure is such that there are very fine structures in the poloidal direction, but in the toroidal direction the wavelength is long. In a tokamak, since the toroidal magnetic field is much stronger than the poloidal field, the mode structure changes slowly along the field line, and the stabilising energy from the field line bending is minimised.

In determining stability against ballooning modes, the stabilising field line bending and the pressure gradient drive compete with each other. For circular plasmas, this means that ballooning modes are stabilised by the shear of the magnetic field. Strong shear, means as magnetic field lines are followed they move away from each other and the mode cannot be localised on the unfavourable side. What stabilises the ballooning mode is the local shear. So even when the global shear goes to zero, a large pressure gradient creates a large variation of local shear in the region where ballooning modes are localised, and the plasma enters a second stability region. Plasma shaping, for e.g. increased triangularity, can result in a magnetic field covering larger distance in regions of favourable curvature, hence increasing stability. A more detailed description of ballooning modes is given in the Appendix C.

2.2.5 Tearing modes

The tearing instability in a tokamak is driven by the radial gradient of the equilibrium current density. The name derives from tearing and rejoining of magnetic field lines which occur during the instability as a consequence of finite resistivity. Consider a plasma with a perturbation of first order, where a perturbed movement of the plasma with velocity \mathbf{v}_1 , causes a electric field \mathbf{E}_1 which induces a magnetic field \mathbf{B}_1 . In an ideal plasma with conductivity $\sigma = \infty$, this is the case for kink instabilities. In a resistive plasma $\sigma \neq \infty$

the magnetic field perturbation can be induced through a perturbed \mathbf{J}_1 . From Ohm's law 2.17 and Faraday's law 2.19 it is seen:

$$\partial \mathbf{B}_1 / \partial t = \nabla \times (\mathbf{v}_1 \times \mathbf{B}_0 - \mathbf{J}_1 / \sigma) \quad (2.33)$$

Due to finite resistivity the conservation of the magnetic flux is no more valid, it can be generated or inhibited by a plasma instability, which will lead to change of the magnetic topology and formation of magnetic islands.

2.2.6 Drift waves

Spatial nonuniformity causes a diamagnetic current in a plasma. For e.g in the case of nonuniform density, due to gyro-motion there are more particles moving in one of the directions of $\nabla n \times \mathbf{b}$ than in the opposite one, and a net drift of plasma results. Electrons and ions gyrate and hence drift in opposite directions, thus a diamagnetic current is produced.

The cylindrical plasma is represented in a cylindrical coordinate system (r, ϑ, z) , and correspondingly in a slab model in cartesian system with (x, y, z) , respectively. Such a model can be used to simulate plasma if the spatial scale of interest across the magnetic field is much shorter than the radius of the cylinder. Consider a plasma of uniform temperature but nonuniform density with density gradient in the x -direction, a static magnetic field \mathbf{B} exists in the z -direction and a consequent diamagnetic current in the y -direction. We assume that the T_e is finite and $T_i \rightarrow 0$. In the unperturbed system $\mathbf{E}_0 = 0$ and further absence of magnetic perturbation is assumed. From the electron equation of motion 2.12 in a stationary state

$$0 = -en_e(\mathbf{u}_e^0 \times \mathbf{B}) - \nabla P_e \quad \Rightarrow \quad \mathbf{u}_e^0 = -\frac{T_e}{m_e |\Omega_e| n_0} \frac{dn_0}{dx} \hat{\mathbf{y}} \quad (2.34)$$

where Ω_e is the electron cyclotron frequency. This velocity is called the electron diamagnetic drift velocity.

Drift waves are quasi-electrostatic waves which in the above used slab geometry, propagate mainly in the y -direction with a phase velocity close to the electron diamagnetic drift velocity. They also propagate in the z -direction, but the wavelength in this direction is much longer. We denote the wavenumber $\mathbf{k} = (0, k_y, k_z)$, then the parallel phase velocity ω/k_z is close to the thermal speed of the electrons, $1/k_y$ is of the same order or less than the inverse of the ion Larmor radius.

One can derive the dispersion relation using linearised two-fluid model. Taking into account the magnetic Lorentz force, and neglecting the ion temperature in 2.12, we get

$$\begin{aligned} m_i n_0 \frac{\partial \mathbf{u}_i^1}{\partial t} &= en_0 (-\nabla \phi^1 + \mathbf{u}_i^1 \times \mathbf{B}_0) \\ m_e n_0 \frac{\partial \mathbf{u}_e^1}{\partial t} &= -en_0 (-\nabla \phi^1 + \mathbf{u}_e^1 \times \mathbf{B}_0) - T_e \nabla n_e^1 \end{aligned} \quad (2.35)$$

we combine these equations with the ion continuity equation and charge neutrality condition:

$$\frac{\partial n_i^1}{\partial t} + n_0 \nabla \cdot \mathbf{u}_i^1 + \mathbf{u}_i^1 \cdot \nabla n_0 = 0 \quad n_i^1 = n_e^1 \quad (2.36)$$

We ignore the electron inertia in 2.35, whose z -component then yields the Boltzmann relation $n_e^1/n_0 \sim e\phi_e^1/T_e$, while the perpendicular component yields the electron drift across the magnetic field. We use a Fourier representation

$$(n^1, \mathbf{u}^1, \phi^1) = (\tilde{n}^1, \tilde{\mathbf{u}}^1, \tilde{\phi}^1) \exp(i\mathbf{k} \cdot \mathbf{r} - i\omega t) \quad (2.37)$$

where \mathbf{r} stands for the position vector (x, y, z) . Applying 2.37 to 2.35 and 2.36, for the case when $\omega \ll \Omega_i = eB_0/m_i$ one gets:

$$\tilde{\mathbf{u}}_{i\perp}^1 = i \frac{\hat{\mathbf{z}} \times \mathbf{k} \tilde{\phi}^1}{B_0} + \frac{\omega}{B_0 \Omega_i} k_y \hat{\mathbf{y}} \tilde{\phi}^1 \quad \tilde{u}_{iz}^1 = \frac{ek_z}{m_i \omega} \tilde{\phi}^1 \quad (2.38)$$

In the first equation, the first term represents the $\mathbf{E} \times \mathbf{B}$ drift and the second term is the polarisation drift (see next section). Together 2.35, 2.36, 2.37 and 2.38, assuming $\omega^2 \ll \Omega^2(k_z/k_y)^2$, give:

$$\frac{\tilde{n}_i^1}{n_0} = \left(\frac{k_z^2 T_e}{\omega^2 m_i} - \frac{k_y T_e}{\omega e B_0 n_0} \frac{dn_0}{dx} \right) \frac{e \tilde{\phi}^1}{T_e} \quad (2.39)$$

from which using $c_s^2 = T_e/m_i$ and 2.34, the dispersion relation is obtained:

$$\omega^2 - \omega_* \omega - k_z^2 c_s^2 = 0 \quad (2.40)$$

where $\omega_* = k_y u_{ey}^0$ is called the drift frequency.

2.3 Transport

The transport processes in tokamak plasmas are quite complicated, partly due to geometrical effects and more seriously due to electromagnetic fluctuations.

2.3.1 Drift motion

When force \mathbf{F} is applied to a charged particle in a direction perpendicular to the static magnetic field \mathbf{B} , a guiding centre motion is induced in the direction perpendicular to both \mathbf{B} and \mathbf{F} , called the particle drift. The guiding centre equation of motion for this situation is written as

$$m \frac{d\bar{\mathbf{v}}}{dt} = \mathbf{F} + q \bar{\mathbf{v}}_{\perp} \times B \quad (2.41)$$

where the left hand side vanishes at steady state. Taking the vector product of the resulting equation with \mathbf{b} , and applying relevant vector identity one gets the drift velocity:

$$\bar{\mathbf{v}}_{\perp} = \frac{\mathbf{F} \times B}{qB^2} \quad (2.42)$$

An effective force \mathbf{F} can be provided due to presence of a static or time varying electric field, curvature or gradient of the magnetic field and other possible sources.

2.3.2 Classical and neoclassical transport

Consider a plasma immersed in a uniform magnetic field along the z -axis, $B_0\hat{\mathbf{e}}_z$. In the absence of collisions, a charged particle executes a rotation around its guiding centre which moves along a magnetic line of force. Collisions can displace the guiding centre perpendicular to the field line. If we assume that collisions are sufficiently rare, the sequence of displacements can be treated as random events, and introduce the probability $g(\Delta\mathbf{r}, \tau)$ for the particle to be displaced by $\Delta\mathbf{r}$ in time τ , being the mean time between collisions. Then the particle density at position $\mathbf{r} = (x, y) = (r \cos \vartheta, r \sin \vartheta)$ and time t can be written as:

$$n(\mathbf{r}, t) = \int d(\Delta\mathbf{r})n(\mathbf{r} - \Delta\mathbf{r}, t - \tau)g(\Delta\mathbf{r}, \tau) \quad (2.43)$$

Due to axisymmetry, $g(\Delta\mathbf{r}, \tau)$ can be assumed independent of ϑ , i.e. $g(\Delta r, \tau)$. We further assume that the dispersion of the radial displacement is proportional to τ and can be given as:

$$\int d(\Delta\mathbf{r})g(\Delta r, \tau)(\Delta r)^2 = 2D\tau = \langle(\Delta r)^2\rangle \quad D = \langle(\Delta r)^2\rangle/2\tau \quad (2.44)$$

where D is called the diffusion coefficient. The expression for D in 2.44, is useful for a wide class of problems to estimate transport coefficient in the context of random walk. In the example of cross field diffusion, in a uniform magnetic field the classical diffusion coefficient can be written as:

$$D_c = \nu\rho_L^2 \quad \rho_L^2 = \langle(\Delta r)^2\rangle/2 \quad \tau = 1/\nu \quad (2.45)$$

where ρ_L is the Larmor radius and ν is the electron-ion collision frequency. Classical diffusion can be explained more elaborately using two-fluid equations (2.11, 2.12, 2.13). When inertia terms are neglected, the equations of motion for electron and ion fluids, under the quasi-neutrality condition $n = n_e = n_i$ become:

$$\begin{aligned} -ne(\mathbf{E} + \mathbf{u}_e \times \mathbf{B}) - \nabla P_e + nm_e\nu_{ei}(\mathbf{u}_i - \mathbf{u}_e) &= 0 \\ ne(\mathbf{E} + \mathbf{u}_i \times \mathbf{B}) - \nabla P_i - nm_i\nu_{ie}(\mathbf{u}_i - \mathbf{u}_e) &= 0 \end{aligned} \quad (2.46)$$

In a cylindrically symmetric plasma column with uniform magnetic field $B_0\hat{\mathbf{z}}$, only a radial electric field is produced, since density and temperature depend only on r . The ϑ -component of 2.46 are written as:

$$-neu_{er}B_0 + nm_e\nu_{ei}(u_{i\vartheta} - u_{e\vartheta}) = 0 \quad neu_{ir}B_0 - nm_i\nu_{ie}(u_{i\vartheta} - u_{e\vartheta}) = 0 \quad (2.47)$$

Summing up these equations 2.47, considering $m_e \nu_{ei} = m_i \nu_{ie}$ we have $u_{ir} = u_{er}$. This means $\Gamma_e = \Gamma_i$, i.e. the diffusion is ambipolar. In fully ionised plasma in cylindrical geometry, the ambipolar diffusion is established at steady state due to conservation in electron-ion collisions. The radial components of 2.46 are written as:

$$-ne(E_r + u_{e\vartheta}B_0) - \frac{dP_e}{dr} = 0 \quad ne(E_r + u_{i\vartheta}B_0) - \frac{dP_i}{dr} = 0 \quad (2.48)$$

Equations 2.48 give us $u_{e\vartheta}$ and $u_{i\vartheta}$, which combined with 2.47 gives:

$$\Gamma_{er} = \frac{m_e \nu_{ei}}{e^2 B_0^2} \frac{d(P_e + P_i)}{dr} \quad (2.49)$$

The radial electric field causes a drift in the ϑ direction. In axisymmetric toroidal plasmas the ambipolar condition is also satisfied automatically. If $\Gamma_e \neq \Gamma_i$, charge separation occurs which produces a local electric field imposing $\Gamma_e = \Gamma_i$.

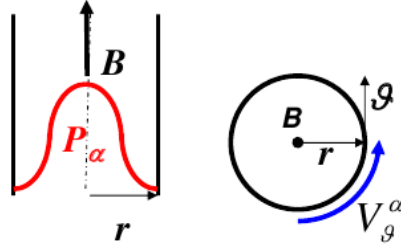


Figure 2.1: Classical transport: In a cylindrical geometry the pressure profile has only a radial gradient which leads to a poloidal diamagnetic drift in opposite directions for electrons and ions. The resulting poloidal frictional force along with the magnetic field leads to a net radial drift

Let us consider transport in a tokamak geometry, where the particle and heat fluxes are substantially larger than those which would occur in a cylinder. The transport in a cylinder is called classical and that in a torus is called neoclassical. Three collisional regimes can be identified: (i) The collisional, Pfirsch-Schüller, regime where a typical particle undergoes a collision before it moves a path of length L_c . (ii) The Banana regime in which a trapped particle completes a bounce orbit in less than a collision time. (iii) The plateau regime where the collision frequency lies between the limits (i) and (ii). Whereas the Pfirsch-Schüller regime can be treated using the equations of resistive MHD, the banana and plateau regimes require kinetic description. However here only heuristic estimates are given.

(i) Pfirsch-Schüller regime ($\nu > v_T/Rq$): relatively short mean free path $\lambda = v_T \tau < L_c$. The particle drifts across the magnetic surface with a velocity on the order of $v_\perp = v_T^2 / \omega_c R_0$. The maximum displacement takes place when v_\perp is multiplied by the time of flight along a section of the field line in which

the curvature does not change its sign, which is of the order of $t = L_c^2/D_{\parallel}$, where D_{\parallel} is the coefficient of longitudinal diffusion. Thus $\Delta r \sim v_{\perp}t$ and $D = (\Delta r)^2/t = \nu\rho^2q^2$. The total diffusion coefficient including the classical diffusion, is $D^{PS} = D_c(1 + \alpha_n q^2)$, where α_n is a constant near unity. To obtain a more complete expression for D^{PS} one needs to consider convection caused by the toroidal curvature.

(ii) The banana regime has the lowest collisionality $\nu < \epsilon^{3/2}v_T/Rq$. The deviation of the particle orbit from the flux surfaces is determined by the drift velocity due to gradient and curvature of \mathbf{B} :

$$\mathbf{v}_d = \mathbf{v}_G + \mathbf{v}_c = \frac{W_{\perp}(\mathbf{B} \times \nabla B)}{eB^3} + \frac{2W_{\parallel}(\mathbf{R}_c \times B)}{eB^2R_c^2} \quad (2.50)$$

where W_{\perp} and W_{\parallel} are perpendicular and parallel energy of the particle, respectively. The predominant magnetic field variation in an axisymmetric toroidal system results from $B = B_t = B_0(1 - r/R \cos \vartheta)$. The parallel velocity can be expressed as:

$$v_{\parallel} = \pm(2(W - W_{\perp})/m)^{1/2} = \pm(2(W - \mu B)/m)^{1/2} \quad (2.51)$$

where μ denotes the magnetic moment and it is conserved as an adiabatic invariant. Equation 2.51 shows that when $\mu B = W$ is satisfied or when $\mu B_0/W > 1/\epsilon$, where $\epsilon = r/R$, the parallel velocity vanishes and the particle will be trapped in the local mirror field. This implies the drift in the guiding centre motion due to magnetic field inhomogeneity is approximately vertical: positively (negatively) charged particles drift downward (upward). The net radial drift of trapped particles during a bounce, and a poloidal circuit of untrapped particles, is zero because in the presence of poloidal magnetic field, the lowest order motion of the g.c. causes it to spend equal times above and below the magnetic axis.

The guiding centre orbit of trapped particles on the poloidal plane is called a banana orbit. For $\nabla\mathbf{B}$ drift, the drift speed is of the order of mv_{\perp}^2/eB_0R while the bounce time is $\tau_B \sim L_c/v_{\parallel}$ where $L_c = qR$ corresponds to the connection length, i.e. the length of the field line starting from the outermost region and ending at the innermost region of the cross section. For trapped particles with $\mu B_0/W = 1 - \epsilon$, from 2.51 one gets:

$$v_{\parallel} = (r/R)^{1/2}v_T \quad d = v_d\tau_B = \rho_L B_0/B^{\vartheta}(r/R)^{1/2} \quad (2.52)$$

where d is the banana width, which becomes much larger than ρ_L since $B^{\vartheta}/B_0 = (r/qR) \ll (r/R)^{1/2}$ with the safety factor $q \geq 1$ in tokamaks not very close to the plasma axis. From 2.51, a particle is trapped if at $\vartheta = 0$ its pitch angle α satisfies

$$\sin \alpha = (W_{\perp}(\vartheta = 0)/W)^{1/2} \geq (B_{min}/B_{max})^{1/2} = ((1 - \epsilon)/(1 + \epsilon))^{1/2} \quad (2.53)$$

The fraction of trapped particles can be estimated from

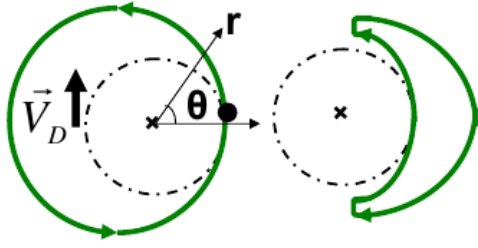


Figure 2.2: Poloidal projection of untrapped and trapped particle trajectories. Diffusion of trapped particles is higher due to higher collision frequency and characteristic length

$$f_{trap} = (1 - \int_0^{\alpha_0} \sin \alpha d\alpha) = (2\epsilon/(1 + \epsilon))^{1/2} \simeq (2\epsilon)^{1/2} \quad (2.54)$$

where $\alpha_0 = \sin^{-1}(B_{min}/B_{max})^{1/2}$, and an isotropic particle distribution has been assumed. One can calculate an effective collision frequency for scattering a trapped particle out of the trapped region [37], $\nu_{eff} = R\nu_c/r$. The diffusion coefficient for trapped particles can thus be estimated. The characteristic length is d , the characteristic time $1/\nu_{eff}$, and only a fraction $(2\epsilon)^{1/2} \sim (r/R)^{1/2}$ of the particles are trapped, therefore:

$$D = \nu_{eff} d^2 (r/R)^{1/2} = (B_0/B^\theta)^2 (r/R)^{1/2} D_c \quad (2.55)$$

which is the diffusion coefficient in the banana regime.

(iii) In the plateau regime $\epsilon^{3/2}v_T/Rq < \nu < v_T/Rq$: diffusion is dominated by a class of slow circulating particles. These are particles which have such a low v_{\parallel} that they suffer small angle collisions with $\Delta v_{\parallel} \sim v_{\parallel}$ during one small transit round the torus. Since coulomb collisions are diffusive in velocity space this characteristic value of v_{\parallel} round the torus: $\nu(v_T/v_{\parallel})^2 \sim v_{\parallel}/Rq$, thus the resonant velocity is given by $v_{\parallel}/v_T \sim (\nu Rq/v_T)^{1/3}$. Due to magnetic drift, a particle with this resonant velocity drifts a radial distance $d \sim v_d \tau$ in a transit time $\tau \sim Rq/v_{\parallel}$, the fraction of resonant particles is $\sim v_{\parallel}/v_T$, the diffusion coefficient $D^P \sim v_d^2 Rq v_{\parallel}/v_T v_{\parallel} \sim v_T q \rho^2/R$, i.e. formally independent of collision frequency.

An interesting feature of the neoclassical transport is the bootstrap current. In tokamaks the trapped electrons carry a diamagnetic current in the toroidal direction associated with their banana orbits. Collisions between trapped and passing particles transfer momentum to untrapped electrons. This must be balanced by the loss of momentum due to collisions between electrons and ions leading to a toroidal current, the bootstrap current.

Classical and Neoclassical transport mechanisms are always present in tokamak plasmas. But, the observed transport levels are higher and are believed to be driven by instabilities. We discuss enhanced transport due to electro-magnetic fluctuations and due to drift waves (for generality).

2.3.3 Transport due to instabilities

Small fluctuations of the electric and magnetic field lead to small fluctuations in the particle velocity and radial position. For low frequency fluctuations, $\omega \ll \omega_{ci}$, so that particles gyro-motion is fast enough and can not be disturbed by the slower fluctuations, a particle's radial velocity is given as:

$$\tilde{v}_r = (\tilde{E}^\theta + v_\parallel \tilde{B}^r)/B \quad (2.56)$$

The fluctuations in the particle's radial motion can lead to both anomalous particle transport and associated thermal transport. However, the net transport depends not just on the level of the fluctuations but also on the correlation between various quantities. Consider the radial particle flux $\Gamma = nu_r$ where u_r denotes the fluid velocity. In a turbulent plasma, each quantity can be written as a time averaged part plus a fluctuating part, e.g. $n = \langle n \rangle + \tilde{n}$, where the average is made over a time scale which is long compared to the frequency of the fluctuations, so that $\langle \tilde{n} \rangle = 0$ and $n = \langle n \rangle$ is the average or macroscopic density. The net particle flux can be written as:

$$\Gamma = \langle (\langle n \rangle + \tilde{n})(\langle u_r \rangle + \tilde{u}_r) \rangle = \langle n \rangle \langle u_r \rangle + \langle \tilde{n} \tilde{u}_r \rangle \quad (2.57)$$

The contribution from the turbulence thus depends on the correlation between the density and radial velocity fluctuations:

$$\Gamma = \langle nu_r \rangle = \int_{-\infty}^{\infty} n^*(\omega) u_r(\omega) d\omega \quad (2.58)$$

where $\tilde{n}(\omega)$ and $\tilde{u}_r(\omega)$ are Fourier components with respect to the angular frequency ω . On assumption that the the flux is ambipolar

$$\Gamma = \frac{\langle \tilde{n} \tilde{E}^\theta \rangle}{B} + \frac{\langle \tilde{J}_\parallel \tilde{B}^r \rangle}{eB} \quad \tilde{J}_\parallel = -e \int_{-\infty}^{\infty} v_\parallel \tilde{f}_e dv_\parallel \quad (2.59)$$

\tilde{J}_\parallel is the fluctuation in the parallel electron current and \tilde{f}_e is the fluctuating part of the electron distribution function. The particle diffusion coefficient is then defined by $D = -\Gamma / (d \langle n \rangle / dr)$. When this significantly exceeds the neoclassical level, it is called anomalous diffusion. This definition is a bit idealised as the turbulent flux can depend on many different quantities.

For low frequency electrostatic ($\tilde{B} = 0$) microturbulence such as drift wave turbulence, the heat flux depends on the correlation between the fluctuating radial velocity $\tilde{u}_r = \tilde{E}^\theta / B$ and the pressure fluctuations \tilde{P} . The heat flux can be written as:

$$Q_r = 5 \langle \tilde{E}^\theta \tilde{P} \rangle / 2B \quad Q_r = 5T\Gamma_r / 2 + q_r \quad (2.60)$$

where Q_r is the total heat flux and q_r is the conductive part. In addition to 2.60, the radial magnetic field fluctuations in finite β plasmas generate another heat flux which results from that part of the large classical conductivity that is now directed radially. The classical conductive heat flux is:

$$\mathbf{q} = -\kappa_{\parallel}\nabla_{\parallel}T - \kappa_{\perp}\nabla_{\perp}T \quad (2.61)$$

where κ_{\parallel} and κ_{\perp} are the conductivity parallel and perpendicular to the magnetic field, respectively. The contribution to the radial heat flux from the magnetic fluctuations is obtained from 2.61 when the unit vector along the magnetic field \mathbf{b} , as well as the temperature, are written as an average plus a fluctuating part $\mathbf{b} = \langle\mathbf{b}\rangle + \tilde{B}^r\hat{\mathbf{r}}/B$, where $\langle\mathbf{b}\rangle$ is in the direction of the unperturbed magnetic field. The radial component of the heat flux is obtained by multiplying $\tilde{B}^r\hat{\mathbf{r}}/B$ by 2.61

$$q_r = -\kappa_{\parallel}\langle|\tilde{B}^r/B|^2\rangle d\langle T\rangle/dr - \kappa_{\perp}\langle|\tilde{B}^r/B|d\tilde{T}/dr\rangle \quad (2.62)$$

where $\langle\nabla_{\parallel}\rangle\langle T\rangle = 0$ and the third order correlations terms which can arise from fluctuations of κ_{\parallel} have been neglected. In 2.62, the first term represents the enhanced radial contribution of transport along perturbed field lines and will be considered in our investigations. The second term represents the enhanced contribution of transport perpendicular to field lines. Similar consideration can estimate classical particle fluxes due to magnetic fluctuations.

We see now how drift waves that were discussed earlier (in section 2.2), can lead to anomalous transport. The drift wave is a quasi-electrostatic wave which propagates perpendicular to both the magnetic field and the density gradient. Electrons move along the field line to compensate for the charge separation by the ion $\mathbf{E} \times \mathbf{B}$ drift along the density gradient, i.e. to keep charge neutrality. Neglecting electron inertia, the Boltzmann relation $\tilde{n}_k/\langle n\rangle \sim e\tilde{\phi}_k/T_e$ is maintained. However, by some means (e.g. electron-ion collisions), the potential propagation is delayed behind the density propagation. Then the $\mathbf{E} \times \mathbf{B}$ drift tends to enhance the density perturbation, since the drift from the high (or low) density side takes place at the crest (or trough) of the perturbation. The growth rate is naturally expected to be proportional to the phase delay $\gamma(\mathbf{k}) \sim \delta(k)$.

Transport due to electrostatic drift waves can be estimated by quasilinear calculations. An underlying assumption of the quasilinear theory is that there exists a spectrum of linearly unstable normal modes whose amplitude is small enough so that the interaction of the modes with each other can be neglected. Quasilinear theory also assumes that the particles respond linearly to the wave.

Assuming quasi-neutrality and that the radial velocity fluctuation is due to the fluctuating $\mathbf{E} \times \mathbf{B}$ drift, the fluctuation-induced particle flux can be written from the first term of 2.59 as:

$$\Gamma = -D\frac{d\langle n\rangle}{dr} = \frac{\langle\tilde{n}\tilde{E}^{\theta}\rangle}{B} \quad (2.63)$$

In low frequency drift waves, the electrons reach a nearly Boltzmann distribution, and the density perturbation with the wave number \mathbf{k} can be approximated as:

$$\tilde{n}_k = \langle n\rangle\frac{e\tilde{\phi}_k(1 - i\delta_k)}{T_e} \quad (2.64)$$

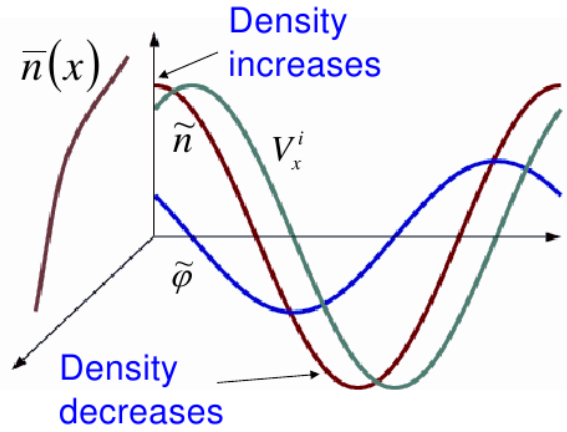


Figure 2.3: Drift waves grow when there is a phase shift between \tilde{n}_k and $\tilde{\phi}_k$

where $\tilde{\phi}_k$ is the fluctuation in the potential and δ_k is a real small quantity which stands for the phase difference between \tilde{n}_k and $\tilde{\phi}_k$. The particle flux thus becomes:

$$\Gamma = \langle n \rangle \frac{T_e}{eB} \sum_k k_{\vartheta} \delta_k |\tilde{n}_k / \langle n \rangle|^2 \frac{e \tilde{\phi}_k (1 - i \delta_k)}{T_e} \quad (2.65)$$

where k_{ϑ} is the poloidal wavenumber. The growth rate of the drift wave is determined by δ_k . Usually $\delta_k \sim \gamma(\mathbf{k}) / \omega_r(\mathbf{k}) \sim \gamma(\mathbf{k}) / \omega_{*e}$. Here $\omega_{*e} = k_{\vartheta} T_e / e B L_n$ is the drift frequency. The diffusion coefficient can thus be approximated as:

$$D \sim L_n^2 \sum_k \gamma(\mathbf{k}) |\tilde{n}_k / \langle n \rangle|^2 \quad (2.66)$$

where $L_n = \langle n \rangle / (d\langle n \rangle / dr)$ is the scale length of the density gradient. This expression is often used as a basis for estimating the amount of transport to be expected from observed or estimated levels of density fluctuations. Quasilinear calculation of the fluxes is very sensitive to the assumption of linear electron response, as can be seen from its direct proportionality to δ_k . Moreover the fluxes are also directly dependent on the fluctuation level $|\tilde{n} / \langle n \rangle|$, which is not determined in the quasilinear theory. A frequently used estimate of the fluctuation level is the 'mixing length' limit, and gives the diffusion coefficient as:

$$|\tilde{n} / \langle n \rangle| = 1 / k_{\perp} L_n \quad \Rightarrow \quad D = \gamma(k) / k_{\perp}^2 \quad (2.67)$$

where k_{\perp} is the perpendicular wavenumber. In this limit, the perturbed density gradient $k_{\perp} \tilde{n}$ is comparable to the mean density gradient, which is the free energy source of the drift wave instability. Comparing the D here with the random walk argument the correlation length is $1 / k_{\perp}$ and the correlation time is $1 / \gamma$.

Chapter 3

Magnetic islands

The first case of enhanced transport in plasmas due to MHD instabilities which we consider here is that in the presence of magnetic islands.

3.1 Magnetic island geometry

Magnetic islands are well known phenomena in hot fusion plasmas generated by resonant perturbations of the magnetic field. The latter arise from different sources such as MHD instabilities developing spontaneously when some parameters approach a critical level, e.g., neoclassical tearing modes [8, 9, 23, 26, 38, 46], or special coils introduced in order to control the plasma behaviour [20, 27, 29, 48]. Recently such coils have been successfully used for mitigation or even complete suppression of the edge localised modes in DIII-D [44, 57] and JET [61] tokamaks.

In order to analyse transport through a magnetic island, it is useful to understand the geometry of an island in a field aligned coordinate system. Here instead of the toroidal coordinate system (r, ϑ, φ) , one uses the coordinates (r, ζ, η) where η is field aligned, and ζ is perpendicular to it as well as to r , fig. 3.1. The physical coordinates of a point in the respective coordinate systems would be $(r, r d\vartheta, R d\varphi)$ and (r, ζ_*, η_*) . Since r is common to both coordinate systems, the other two components of both can be mapped on a two-dimensional plane, as (ϑ, φ) and (ζ, η) lie on the same plane, since field lines follow the concentric magnetic surfaces in case of unperturbed systems. From $d\mathbf{l} \times \mathbf{B} = 0$ one can see that \mathbf{B} has an inclination $\alpha = \cos^{-1} B^\varphi/B$, to the toroidal coordinate $R d\varphi$ on a magnetic surface.

Observing the projections of an arbitrary point located on the two-dimensional plane, on the coordinate axis of both coordinate systems, one obtains $\zeta_* = r\vartheta \cos \alpha - R\varphi \sin \alpha$ and $\eta_* = r\vartheta \sin \alpha + R\varphi \cos \alpha$, whereupon considering $\cos \alpha = B^\varphi/B \simeq 1$, $\sin \alpha = B^\vartheta/B$ and $q = \Delta\varphi/\Delta\vartheta \equiv B^\varphi r/B^\vartheta R$, one obtains $\zeta_* = r(\vartheta - \varphi/q)$ and $\eta_* = r^2\vartheta/Rq + R\varphi$. Separating r from the expression for ζ_* we get the commonly used dimensionless coordinate $\zeta = \vartheta - \varphi/q$.

As mentioned before magnetic islands are generated by resonant perturbations of the magnetic field. The magnetic field perturbations can be repre-

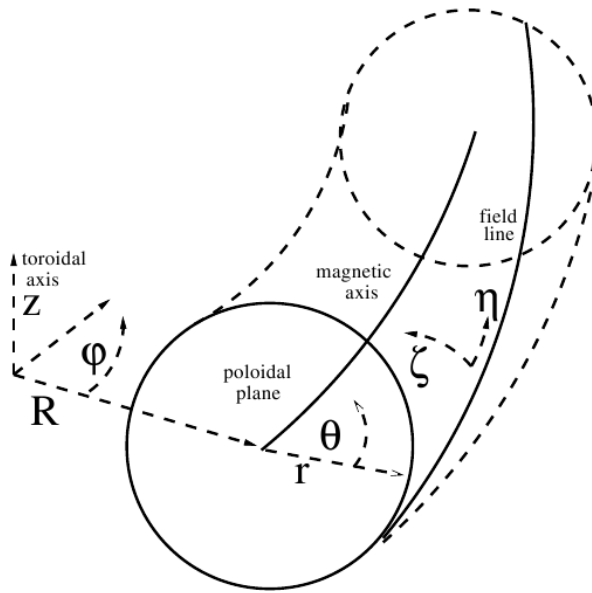


Figure 3.1: Helical coordinate system: showing the toroidal (r, ϑ, φ) and field aligned (r, ζ, η) coordinate systems

sented as a series of Fourier harmonics:

$$\tilde{\mathbf{B}} = \sum_{m,n} \tilde{\mathbf{B}}_{m,n} \sin \zeta \quad (3.1)$$

where $\zeta = m\vartheta - n\varphi$ is the harmonic phase with periods m and n in the poloidal and toroidal directions ϑ and φ , respectively. For the formation of magnetic islands it is essential that such perturbations have radial components \tilde{B}^r which are not present in the main tokamak field composed of the poloidal and toroidal components B^ϑ and B^φ , respectively. Due to \tilde{B}^r field lines deviate in the radial direction. This is especially pronounced in the vicinity of the resonant magnetic surfaces (RS - also denoted by subscript s) where the safety factor q , is equal to the ratio m/n . Here the corresponding Fourier harmonic is constant along field lines. In such a situation the field line would experience a constant radial deviation from the unperturbed surface, but this is avoided due to the nonzero magnetic shear $s = rdq/qdr$, the field lines now have a component $\Delta B^\zeta = B_r^\zeta - B_s^\zeta$, with respect to alignment of the magnetic field on the resonant surface, which moves the field line in ζ , where the radial perturbation $\tilde{B}^r = \tilde{B}_{m,n}^r \sin \zeta$ differs. Consequently field lines move up and down relative to the unperturbed magnetic surface, going back to the starting phase ζ_0 , where they intersect the resonant surface. The fact that resonance with the magnetic perturbation weakens with the distance from the RS, which implies $\tilde{B}_{m,n}^r$ decreases as the magnetic field moves away from the RS, also plays a role in the island geometry, but to simplify our explanation we do not concern ourselves with the radial variation of the perturbation.

For example, consider a perturbation with a particular fourier harmonic

$\tilde{B}_{m,n}$, where the radial perturbation at any point in phase space (r, ζ, η) is given by $(\tilde{B}^r = \tilde{B}_{m,n}^r \sin \zeta)$. To begin with, consider a field line intersecting the resonant surface at the phase angle $\zeta \sim \zeta_0$, measured from the O-point $\zeta = 0$, and located between the O-point and the X-point $\zeta = \pi$. For such a field line $\tilde{B}^r > 0$, i.e. it moves radially outwards relative to the magnetic axis, and since $s \Rightarrow q' > 0$ it now has a component $\Delta B^\zeta < 0$ which means that it is deviating from its original direction towards a $-\zeta$ direction, this can be appreciated from $\Delta\zeta/\Delta r = -q'\Delta\vartheta/q$, where Δr , $\Delta\vartheta$ and $\Delta\zeta$ are the corresponding radial, poloidal and phase deviation w.r.t. the unperturbed magnetic surface. The \tilde{B}^r decreases with decreasing ζ . Eventually both $\zeta, \tilde{B}^r = 0$, a point where the field line reaches a maximum outward radial deviation. At this point since the field line has a component $B^\zeta = \sum \Delta B^\zeta \Delta r < 0$, it continues to move towards $\zeta < 0$, with which $\tilde{B}^r < 0$ increases in magnitude and the radial deviation of the field line decreases, consequently $\Delta\zeta/\Delta r > 0 \Rightarrow \Delta B^\zeta > 0$, thus the field line moves towards the resonant surface and a lower phase angle, but at the same time aligns towards the field line direction on the resonant surface, which it finally achieves on reaching the resonant surface i.e. $B^\zeta = 0$.

At the resonant surface now $\zeta \sim -\zeta_0 < 0$ and therefore $\tilde{B}^r < 0$, the field line moves radially towards the magnetic axis, and due to shear the field line now has a component $\Delta B^\zeta > 0$ which means that it is deviating from its direction on the resonant surface towards a $+\zeta$ direction. The $\tilde{B}^r < 0$ decreases in magnitude with increasing ζ , until finally both $\zeta, \tilde{B}^r = 0$, a point where the field line reaches a maximum inward radial deviation. At this point since the field line has a component $B^\zeta = \sum \Delta B^\zeta \Delta r > 0$, it continues to move towards $\zeta > 0$, with which $\tilde{B}^r > 0$ increases in magnitude and the radial deviation of the field line decreases, consequently $\Delta\zeta/\Delta r < 0 \Rightarrow \Delta B^\zeta < 0$, thus the field line moves towards the resonant surface and a higher phase angle, but at the same time aligns towards the field line direction on the resonant surface, which it finally achieves on reaching the resonant surface i.e. $B^\zeta = 0$. At this point the phase angle corresponds to $\zeta \sim \zeta_0$, and the magnetic field line in end effect traces a path which appears like an island fig. 3.2.

Let us see what happens with a magnetic field line not crossing a resonant surface, but is close to the resonant surface. Such a field line is out of phase with the harmonic perturbation $\tilde{B}^r = \tilde{B}_{m,n}^r \sin \zeta$. Consider a starting phase ζ_0 , with respect to the resonant surface, like for the case above, where now this field line intersects the unperturbed surface at this radial position. Since the magnetic field line is close to the magnetic surface one can assume that the radial perturbation level is very similar as for a field line intersecting the resonant surface. Like for the case discussed above the field line deviates away from the magnetic axis till it reaches the O-point whereon it starts deviating radially towards the magnetic axis. When it reaches $-\zeta_0$, the field line as it was out of phase with the perturbation is still moving in $-\zeta$ direction until it reaches a point in the phase space (r, ζ) just above the X-point. Since the field line is above the X-point, it is directed in $-\zeta$ direction due to shear s , and at the X-point $\tilde{B}^r < 0$ changes to $\tilde{B}^r > 0$. Hence the field line deviates again away from the magnetic axis and reaches the phase ζ_0 , whereon it undergoes

the same cycle of deviations, an end effect of waving of the magnetic field line w.r.t to the resonant surface. Similar argument is valid for field lines further away from the resonant surface, with the amplitude of \tilde{B}^r decreasing with distance from it.

To get insight into the description of the behaviour of the perturbed field lines we make a short analysis. The perturbed magnetic field on the resonant magnetic surface is given by:

$$\tilde{B}^r = \tilde{B}_s^r \sin \zeta \quad (3.2)$$

The cross product of displacement along the field line on the resonant surface with the magnetic field yields zero, since they are essentially in the same direction, this gives us the field line equations:

$$d\mathbf{l} \times \mathbf{B} = 0 \quad \Rightarrow \quad \frac{dr}{\tilde{B}^r} = \frac{Rd\varphi}{B^\varphi} = \frac{rd\vartheta}{B^\vartheta} \quad (3.3)$$

The safety factor at the resonant magnetic surface ($r = r_s$) is, $q_s = B_\varphi r_s / B_\vartheta R = m/n$. Close to the resonant magnetic surface, the Poloidal magnetic field changes radially due to magnetic shear $s = rdq/qdr$. Making a Taylor expansion of B^ϑ close to the resonant surface, where $x = r - r_s$:

$$\begin{aligned} B^\vartheta &= B_s^\vartheta + \left. \frac{dB^\vartheta}{dr} \right|_{r_s} \cdot x & B^\vartheta &\equiv \frac{B^\varphi r}{qR} \\ \left. \frac{dB^\vartheta}{dr} \right|_{r_s} &= \frac{B^\varphi}{q_s R} - \left. \frac{B^\varphi r_s}{q_s^2 R} \frac{dq}{dr} \right|_{r_s} = \frac{B_s^\vartheta}{r_s} (1 - s_s) \\ B^\vartheta &= B_s^\vartheta \left[1 + \frac{x}{r_s} (1 - s_s) \right] \end{aligned} \quad (3.4)$$

Differentiating the equation $\zeta = m\vartheta - n\varphi$ to get a relation between change in ζ of the deviating field line w.r.t. φ on the resonant magnetic surface, one gets:

$$\frac{d\vartheta}{d\varphi} = \frac{1}{m} \frac{d\zeta}{d\varphi} + \frac{1}{q_0} \quad (3.5)$$

From (3.2, 3.3, 3.4, 3.5), with the assumption $x \ll r_s$, we get for the radial deviation of a field line from the resonant surface:

$$x = \frac{w}{2} \left[\xi^2 - \sin^2 \frac{\zeta}{2} \right]^{1/2} \quad (3.6)$$

here, $w = 4 \left(r_s R \tilde{B}_s^r / s_s n B^\varphi \right)^{1/2}$ and $\xi = \delta/w$, where δ is the width of a sub-magnetic surface formed as a result of the perturbation of the resonant surface and w is the width of the island separatrix. At any phase angle ζ_0 , the width of the separatrix $w_* = w \cos(\zeta_0/2)$, the width of the magnetic surface $\delta_* = w \left[\xi^2 - \sin^2(\zeta_0/2) \right]^{1/2}$ and $\xi_* = \delta_*/w$.

The equation 3.6, can also be written as:

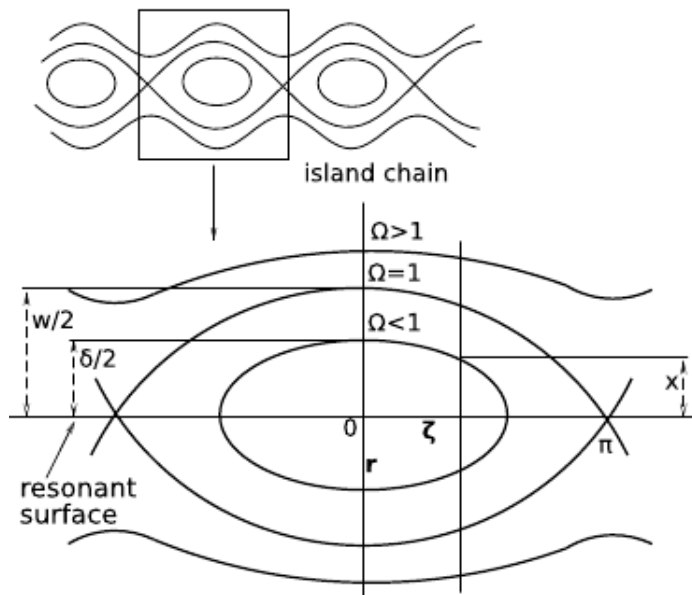


Figure 3.2: Island geometry, as seen on a plane in the phase space r, ζ

$$\Omega = 8 \left(\frac{x}{w} \right)^2 - \cos \zeta \quad (3.7)$$

Here Ω is a label for the magnetic surface. $\Omega = 1$ is called separatrix since it separates the regions of qualitatively different behaviour: for $\Omega > 1$ the perturbation does not change the topology of original magnetic surfaces and waves them slightly in the radial direction; for $\Omega < 1$ the topology is changed so that magnetic surfaces encircle the short-circuited field line passing through the point $\zeta = 0$ on the RS. The cross-section of the separatrix by the plane r, ζ looks like a chain of m magnetic islands with the radial width w .

The deviation of magnetic field lines from unperturbed magnetic surfaces results in an enhancement of the effective particle and heat losses from the plasma. Radial gradients of plasma parameters have nonzero projections along such lines and drive parallel particle and heat flows which contribute to the radial transport. We proceed now with analysis of such transport.

3.2 Fitzpatrick's model for transport through magnetic islands

Fitzpatrick's analysis is an analytical approach to investigate transport through magnetic islands. The basis of this model is described here since it has been extended in the next chapter to determine the heat flux limit for the specific case of an heated magnetic island. Critical assumptions about the temperature at certain points in the analysis, may lead to some doubt about the accuracy of the predictions of this otherwise rigorous model.

The heat flow in the plasma in the presence of RMP is governed by

$$\mathbf{q} = -\kappa_{\parallel}\nabla_{\parallel}T - \kappa_{\perp}\nabla_{\perp}T \quad (3.8)$$

where $\nabla_{\parallel}T \equiv (\mathbf{b} \cdot \nabla T)\mathbf{b}$ and $\nabla_{\perp}T \equiv \nabla T - \nabla_{\parallel}T$, with $\mathbf{b} = \mathbf{B}/|B| \simeq \mathbf{B}/B^z$. In regions of the plasma where there are no significant sources and sinks of heat $\nabla \cdot \mathbf{q} = 0$, so eq. 3.8 yields:

$$\kappa_{\parallel}\nabla_{\parallel}^2T + \kappa_{\perp}\nabla_{\perp}^2T = 0 \quad (3.9)$$

In the vicinity of the rational surface, $\mathbf{b} \cdot \nabla \simeq -(ns_s/R_0r_s)x(\partial/\partial\zeta)_{\Omega}$ and $\nabla_{\perp}^2 \simeq \hat{\mathbf{r}}(\partial^2/\partial x^2)_{\zeta}$, in the thin island limit $w \ll r_s$. For a resonant perturbation ($\delta T \sim 1/x$) the parallel conduction part of (3.9) dominates the perpendicular conduction whenever $|x| \gg x_c \sim (\kappa_{\perp}/\kappa_{\parallel})^{1/4}(R_0r_s/ns_s)^{1/2}$. This implies that, far from the rational surface ($x \gg x_c$), the parallel conductivity forces temperature to be a function of the perturbed flux surfaces, and conversely so close to the rational surface ($x \ll x_c$).

Outside the island ($|x| \gg x_c, w$), the temperature remains a function of helically displaced perturbed magnetic surfaces. If $T_0(r)$ is the unperturbed equilibrium temperature profile, the temperature perturbation associated with a RMP is given by:

$$\delta T(r, \zeta) \simeq -\nabla T_0 \cdot \xi = -T'_0(r)\xi_r \quad (3.10)$$

Far from the island ($|x| \gg x_c, w$ or $\Omega \gg 1$) magnetic surfaces are slightly waved by RMP. From 3.7 one finds for the radial displacement ξ_r of a point with the phase ζ from the unperturbed surface placed at $x = w\sqrt{\frac{\Omega}{8}}$:

$$\xi_r = w\sqrt{\frac{\Omega + \cos\zeta}{8}} - w\sqrt{\frac{\Omega}{8}} \approx w\sqrt{\frac{\Omega}{8}}\frac{\cos\zeta}{2\Omega} = \frac{w^2 \cos\zeta}{16x}$$

where Taylor's expansion has been done by taking into account that $|\cos\zeta|/\Omega \ll 1$. High parallel heat conduction preserves the constant temperature on perturbed magnetic surfaces equal to the temperature without RMP at the minor radius $r = r_s + x$, $T_0(r) \approx T_0(r_s) + T'_0(r_s)x$. Thus

$$T(r, \zeta) = T_0(r) + T'_0(r_s)\xi_r = T_0(r_s) + \tilde{T}(x, \zeta) \quad (3.11)$$

where

$$\tilde{T}(r, \zeta) = T'_s x + w^2 T'_s \cos\zeta / 16x \quad (3.12)$$

and $T'_s = T'_0(r_s)$ is the equilibrium temperature gradient at the resonance surface. The temperature profile given by equation 3.11 provides the boundary condition for the temperature in the region beyond the island which to lowest order has to be antisymmetric about the rational surface, $\tilde{T}(-x, \zeta) = -\tilde{T}(x, \zeta)$. On the contrary, the island temperature profile is assumed to be symmetric about the O-point, $\tilde{T}(x, -\zeta) = \tilde{T}(x, \zeta)$ and periodic in the helical phase angle $\tilde{T}(x, \zeta + 2\pi) = \tilde{T}(x, \zeta)$, this is expected from the symmetry of the island structure.

Let $X = 4x/w_c$ and $w_c = (\kappa_{\perp}/\kappa_{\parallel})^{1/4}(8R_0r_s/n_s s_s)^{1/2}$. Close to the resonance surface, $|x| \ll r_s$ the heat diffusion equation 3.9 can be written as:

$$\frac{1}{4} \left[\left(\frac{w}{w_c} \right)^2 \sin \zeta \frac{\partial}{\partial X} + X \frac{\partial}{\partial \zeta} \right]^2 \tilde{T} + \frac{\partial^2 \tilde{T}}{\partial X^2} = 0 \quad (3.13)$$

The last term corresponds to heat diffusion perpendicular to magnetic field lines effected by radial temperature gradient and depends on κ_{\perp} . The terms in the bracket depend on κ_{\parallel} and correspond to heat diffusion along the field lines, the first term due to the radial temperature gradient and the second term due to the temperature gradient along the field lines.

Small island limit.- In this limit ($w \ll w_c$), the temperature is not a function of the island flux surfaces, due to small perturbation of magnetic surfaces, the parallel thermal conductivity is not effective enough to equilibrate the temperature along the flux surfaces. The periodicity of the temperature perturbation in ζ allows a fourier decomposition, which also satisfies the symmetry requirement:

$$\tilde{T}(X, \zeta) = \sum_{\nu=0}^{\infty} \tilde{T}_{\nu}(X) \cos \nu \zeta \quad (3.14)$$

By taking into account terms of the zeroth and first order we substitute the approximate solution $\tilde{T}(r, \zeta) = \tilde{T}_0(X) + \tilde{T}_1 \cos \zeta$ into equation 3.13. From the equality of terms independent of ζ and proportional to $\cos \zeta$ on the left hand side (LHS) and right hand side (RHS) of this equations one get:

$$\frac{d^2 \tilde{T}_0}{dX^2} \simeq 0 \quad \frac{d^2 \tilde{T}_1}{dX^2} - \frac{X^2 \tilde{T}_1}{4} \simeq -\frac{1}{4} \left(\frac{w}{w_c} \right)^2 X \frac{d\tilde{T}_0}{dX} \quad (3.15)$$

Since X is dimensionless, it is seen from the above equations that $\tilde{T}_{\nu}/\tilde{T}_0 \sim (w/w_c)^{2\nu}$. This confirms that contributions with $\nu \geq 2$ can indeed be neglected in $\tilde{T}(r, \zeta)$. Application of the antisymmetric boundary condition 3.12 yields $\tilde{T}_0 \simeq w_c T'_s X/4$. Thus for the first order component we have $\tilde{T}_1 \simeq w^2 T'_s f(X)/16w_c$ where the function f is governed by the equation:

$$\frac{d^2 f}{dX^2} - \frac{X^2 f}{4} = -X \quad (3.16)$$

The physical constraints on the solution of (3.16) are $f(0) = 0$ and $f \rightarrow 0$ as $|X| \rightarrow \infty$, i.e. at the resonant surface and far from the resonant surface the island does not disturb the unperturbed equilibrium temperature. For $X \rightarrow 0$ one can neglect in equation 3.16 the second term on the LHS and with the boundary condition at $X = 0$ this results in $f \approx CX - X^3/6$. For large X the first term on the LHS can be neglected and $f \approx 4/X$ in agreement with the boundary condition 3.12. Both asymptotic solutions above have to be conjugated at some point X_* under the assumption of the continuity of f and its derivative. This results in $X_* = \sqrt[4]{24} \approx 2.2$ and $C = 4/X_*^2 + X_*^2/6 \approx 1.63$. The maximum $f_{max} = (2C)^{3/2}/3 \approx 1.96$ is achieved at $X_{max} = \sqrt{2C} \approx 1.8$. These estimates are in rough agreement with the results of numerical

evaluation of $f(X)$ in Ref. [28] in the region $X > 0$ providing $C \approx 1.2$, $f_{max} = 1.44$ and $X_{max} \simeq 2$.

Thus, in the small island limit

$$\delta T(r, \zeta) \equiv T(r, \zeta) - T_0(r) \simeq \frac{1.2w^2 T'_s x \cos \zeta}{4w_c^2} \quad (3.17)$$

in the vicinity of the rational surface, for $|x| \ll w_c/2$, and

$$\delta T(x, \zeta) \simeq \frac{w^2 T'_s \cos \zeta}{16x} \quad (3.18)$$

far from the island for $|x| \gg w_c/2$.

Large island limit.- In this limit ($w \gg w_c$), the temperature is a function of the island flux surfaces i.e. $\tilde{T} = \tilde{T}(\Omega)$, this can be seen from (3.13) written in a different form:

$$\frac{1}{4} \left(\frac{w}{w_c}\right)^2 \frac{\partial}{\partial \zeta} (\Omega - \cos \zeta)^{1/2} \frac{\partial \tilde{T}}{\partial \zeta} + \frac{\partial}{\partial \Omega} (\Omega - \cos \zeta)^{1/2} \frac{\partial \tilde{T}}{\partial \Omega} = 0 \quad (3.19)$$

On flux surfaces situated inside the separatrix ($\Omega < 1$), the temperature is antisymmetric $\tilde{T}(-x, \zeta) = -\tilde{T}(x, \zeta)$ about the resonant surface, and together with $\tilde{T} = \tilde{T}(\Omega)$ this leads to $\tilde{T} = 0$, which means that the temperature is flattened within the island separatrix. Averaging (3.19) over the helical phase angle ζ , making use of the periodicity constraint $\tilde{T}(x, \zeta + 2\pi) = \tilde{T}(x, \zeta)$

$$\frac{d}{d\Omega} \left(\oint (\Omega - \cos \zeta)^{1/2} \frac{d\zeta}{2\pi} \frac{d\tilde{T}}{d\Omega} \right) = 0 \quad (3.20)$$

Carrying out integration over Ω gives

$$\frac{d\tilde{T}}{d\Omega} = \pm \frac{c}{\left(\oint (\Omega - \cos \zeta)^{1/2} \frac{d\zeta}{2\pi} \right)} \quad (3.21)$$

where c is a constant, and \pm corresponds to $x \gtrless 0$. The integral can be written as a standard elliptical integral:

$$\oint (\Omega - \cos \zeta)^{1/2} \frac{d\zeta}{2\pi} = \frac{(8)^{1/2} k E(1/k)}{\pi} \quad (3.22)$$

where $k = ((\Omega+1)/2)^{1/2}$, $\alpha = \pi/2 - \zeta/2$ and $E(l) = \int_0^{\pi/2} (1-l^2 \sin^2 \alpha)^{1/2} d\alpha$. For the limit $w \ll |x| \ll r_s$, the temperature profile can be described by, $\tilde{T}(r, \zeta) = T'_s x + w^2 T'_s \cos \zeta / 16x$, which provides us with a boundary condition. Differentiating this temperature profile with Ω , considering $\Omega = 8(x/w)^2 + \cos \zeta$ and $w \ll |x|$, one obtains $c = w T'_s / (32)^{1/2}$ for (3.21), which along with (3.22) gives:

$$\frac{d\tilde{T}}{d\Omega} = \pm \frac{\pi w T'_s}{16k E(1/k)} \quad (3.23)$$

Close to the island the periodicity of the temperature perturbation in ζ allows a fourier decomposition, which also satisfies the symmetry requirement:

$$\delta T(x, \zeta) = \sum_{\nu=1}^{\infty} \delta T_{\nu}(x) \cos \nu \zeta \quad (3.24)$$

From $T(r, \zeta) = T_0(r) + \delta T(r, \zeta) = T_0(r_s) + \tilde{T}(x, \zeta)$, one can by substitution for $\delta T(r, \zeta)$ find the fourier coefficients $\delta T_{\nu}(x)$, considering that terms that remain constant in ζ cancel out in the cyclic integral:

$$\delta T_{\nu}(x) = \frac{1}{\pi} \oint \tilde{T}(x, \zeta) \cos \nu \zeta d\zeta \quad (3.25)$$

Considering the symmetry of cosine about $\zeta = \pi$, and carrying out the integration by parts yields:

$$\delta T_{\nu}(x) = \pm \frac{wT'_s}{16\nu} \int_0^{\zeta_c} \frac{\cos(\nu-1)\zeta - \cos(\nu+1)\zeta}{kE(1/k)} d\zeta \quad (3.26)$$

Since (3.23) is valid only for regions outside the island separatrix, the integration limits are restricted:

$$\zeta_c = \cos^{-1}(1 - 8x^2/w^2) \quad |x| < w/2 \quad \zeta_c = \pi \quad |x| > w/2 \quad (3.27)$$

In the asymptotic limit $x \gg w/2$, (3.26) yields

$$\delta T_1(x) \simeq \frac{w^2 T'_s}{16x} \quad \delta T_{\nu>1}(x) \simeq wT'_s \delta[(\frac{w}{x})^3] \quad (3.28)$$

In the opposite limit $x \ll w/2$, (3.26) yields

$$\delta T_{\nu}(x) \simeq \frac{8wT'_s}{3} (\frac{x}{w})^3 \quad (3.29)$$

Fitzpatrick's approach discussed above provides solution for the heat transport equation for the cases of large and small island limits, that is when either the temperature can be assumed to be a function of the flux surfaces or not. Solutions for the intermediate regime have not been found yet and therefore we propose in the next section an alternative method to approach this problem.

3.3 Transport across non-overlapped islands

In this section we propose a model in order to assess the effective radial heat conduction in a configuration where the heat flux from the plasma core comes through non-overlapped island chains. On the one hand, compared to previous analytical studies [17, 28] (see previous section), the present approach treats on the same foot cases with arbitrary parameter $\varsigma = 4\kappa_{||}b_r^2/\kappa_{\perp}$, where κ_{\perp} and $\kappa_{||}$ are the heat conduction components perpendicular and parallel to

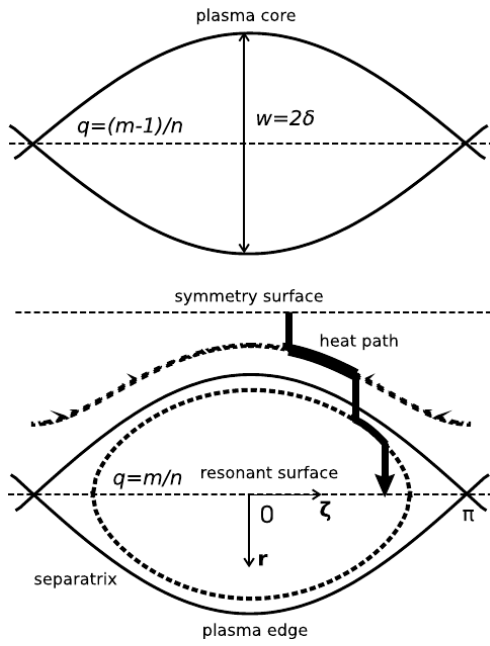


Figure 3.3: Transport paths through a magnetic island

the magnetic field. The parameter ζ is equal to $(w/w_c)^4$ with w_c being the critical island width introduced in Ref. [28]. There the limit cases of "small", $w \ll w_c$ ($\zeta \ll 1$), and "large", $w \gg w_c$ ($\zeta \gg 1$), islands have been considered analytically. On the other hand, it illustrates in a more transparent way than a pure numerical approach [60, 62, 75] what parameters are of concern for the effective transport characteristics, and provides a computationally economical method to find the dependencies on these parameters.

The "optimal path" method applied below was used in Ref.[33, 58] for assessment of transport characteristics in a stochastic magnetic field. It asserts that in a region where heat sources are negligible, in particular, at the plasma edge, the heat supplied from the plasma core is transferred predominantly along paths providing the minimum temperature change. There is a direct relation between this approach and the principle of minimum entropy production [4]. Under conditions in question, i.e., for zero heat source, the entropy production rate per unit volume, θ , is given by the relation $\theta = \mathbf{q} \cdot \nabla (1/T)$ [6], where \mathbf{q} is the heat flux density and T is the single fluid temperature. By applying this relation to a toroidal shell between two close radial positions, $r_{1,2}$, so that $r_2 - r_1 \ll r_{1,2}$, one gets for the total entropy production rate in this shell:

$$\int \theta dV = \frac{P\Delta T}{T_1 T_2} \quad (3.30)$$

with P being the total power transferred through the shell, $T_{1,2}$ the averaged temperatures on its boundary surfaces and $\Delta T = T_1 - T_2$. Thus, the minimum entropy production rate accords to the minimum temperature

change ΔT .

Henceforth we consider the case of $m \gg 1$ so that b_r is not very different for the adjacent RS and the islands have close dimensions in the radial and ζ directions. All heat paths can be combined from elementary sections connecting the symmetry plane and the RS of one of the island chains, see Fig.3.3. The distance between these two surfaces, $x_0 = w/(2\sigma_{Ch})$ where σ_{Ch} is the so called Chirikov parameter [29]. The situation with non-overlapped island chains considered here corresponds to $\sigma_{Ch} < 1$. Henceforth we take into account only heat paths which are composed from sections aligned either in the radial direction or are parallel to the magnetic field. In the former case the radial flux with the density q_r is mostly transported by the perpendicular heat conduction:

$$q_r \approx -\kappa_{\perp} \partial T / \partial r \quad (3.31)$$

and in the latter one - by the parallel one:

$$q_r \approx -(\kappa_{\parallel} \nabla_{\parallel} T) B_r / B = -\kappa_{\parallel} b_r^2 \sin^2 \zeta \partial T / \partial r \quad (3.32)$$

We consider paths including one or two parallel sections which can be placed either inside or outside the island, see Fig.3.3. The initial and final positions of these section are varied in the whole space from the symmetry surface to the RS and optimal paths with the minimum total temperature change are selected. The selection procedure does not exclude sections of zero length. Therefore, depending on the perturbation strength and initial phase of the path at the symmetry surface, the optimal one can be a combination of up to two parallel and three radial segments. The approach can be straightforwardly generalised on a larger number of parallel sections. This leads to noticeable increase of computation time but, presumably, does not provide any significant improvement, as it follows from comparison of results obtained for paths with one and two parallel segments.

The total temperature change along all radial sections of such a path follows from integration of 3.31. With constant κ_{\perp} , one gets for the temperature change along a path aligned in the radial direction:

$$\Delta_{\perp} T = \frac{q_r}{\kappa_{\perp}} \left[x_0 - \sum_{j=1}^{j_{max}} (x_b^j - x_t^j) \right]$$

where $x_{b,t}^j$ are the distances from the RS of the beginning and terminating points of the parallel section j and $j_{max} = 1$ or 2 in this study. By using the relation 3.7 we get from 3.32 for the parallel path sections:

$$\Delta_{\parallel}^j T = \frac{q_r w}{8\kappa_{\parallel} b_r^2} \eta_j$$

with

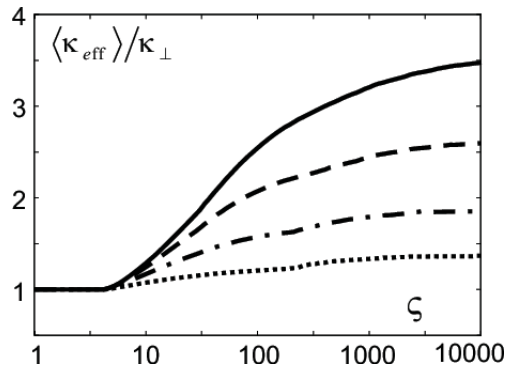


Figure 3.4: The ratio of the effective radial heat conduction to the perpendicular one as a function of the parameter $\zeta = 4\kappa_{\parallel}b_r^2/\kappa_{\perp}$ computed for different magnitudes of the Chirikov parameter σ_{Ch} : $\sigma_{Ch} = 0.9$ (solid curve), 0.8 (dashed curve), 0.6 (dash-dotted curve) and 0.3 (dotted curve).

$$\eta_j = \frac{w}{4a} \ln \frac{(a+x_b^j)(a-x_t^j)}{(a+x_t^j)(a-x_b^j)} + \frac{w}{2c} \left(\arctan \frac{x_b^j}{c} - \arctan \frac{x_t^j}{c} \right)$$

for a section inside the island and

$$\eta_j = \frac{w}{4a} \ln \frac{(a+x_b^j)(a-x_t^j)}{(a+x_t^j)(a-x_b^j)} + \frac{w}{4c} \ln \frac{(x_b^j-c)(x_t^j+c)}{(x_t^j-c)(x_b^j+c)}$$

for that outside.

Here

$$a = \sqrt{\frac{1 - \cos \zeta_j}{2} \frac{w^2}{4} + (x_b^j)^2}$$

$$c = \sqrt{\left| \frac{1 + \cos \zeta_j}{2} \frac{w^2}{4} - (x_b^j)^2 \right|}$$

where ζ_j is the initial phase of the j path parallel section; the initial phases of consequent sections are related as follows:

$$\cos \zeta_{j+1} = \cos \zeta_j + \frac{8}{w^2} \left[(x_t^j)^2 - (x_b^j)^2 \right]$$

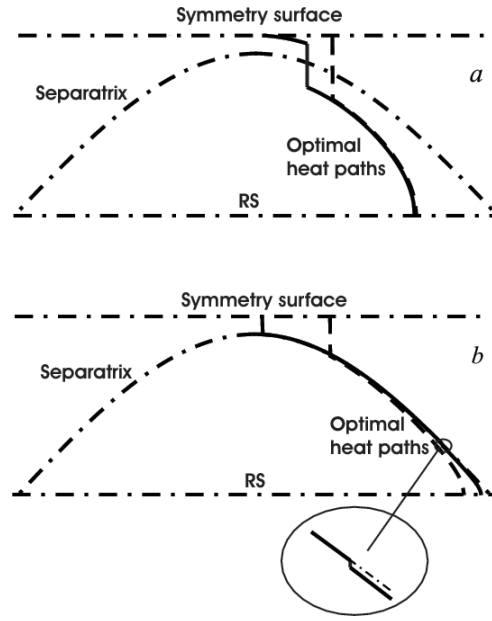


Figure 3.5: Optimal paths beginning at the symmetry surface with the initial phases 0.1 (solid curves) and 1 (dashed curves) found for $\varsigma = 10$ (a) and $\varsigma = 10^4$ (b) with $\sigma_{Ch} = 0.9$.

Optimal paths are selected by varying $x_{b,t}^{j=1,\dots,j_{max}}$ in the whole range $[0, x_0]$ and looking for the minimal total temperature change $\Delta T = \Delta_{\perp} T + \sum_{j=1}^{j_{max}} \Delta_{\parallel}^j T$. The effective radial heat conduction of the optimal path, κ_{eff} , is defined according to the relation:

$$q_r = \kappa_{eff} \frac{\Delta T}{x_0}$$

After averaging over the path initial phase at the symmetry surface we finally get:

$$\frac{\langle \kappa_{eff} \rangle}{\kappa_{\perp}} = \int_0^{\pi} \frac{d\zeta_1/\pi}{1 - \sum_{j=1}^{j_{max}} \left[\frac{2}{w} (x_b^j - x_t^j) - \eta_j/\varsigma \right] \sigma_{Ch}} \quad (3.33)$$

with the definition $x_0 = w/(2\sigma_{Ch})$ taken into account.

Thus $\varsigma = 4\kappa_{\parallel} b_r^2/\kappa_{\perp}$ and σ_{Ch} are the only parameters which characterise the enhancement of κ_{eff} and $\langle \kappa_{eff} \rangle$ over κ_{\perp} . Figure 3.4 shows the ς -dependence of the ratio $\langle \kappa_{eff} \rangle/\kappa_{\perp}$ for different magnitudes of σ_{Ch} computed for paths with up to 3 radial and 2 parallel sections. One can see that the parallel transport contributes to the perpendicular one, i.e., optimal paths include fractions along field lines, if $\varsigma \geq 4$. The enhancement level saturates when ς exceeds $10^3 - 10^4$, depending on σ_{Ch} . In this case the temperature change in the island

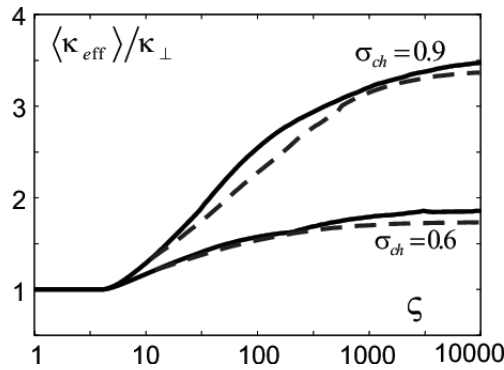


Figure 3.6: The ratio of the effective radial heat conduction to the perpendicular one as a function of the parameter ζ computed for different magnitudes of the Chirikov parameter by taking into account heat paths with up to two (solid curve) and one (dashed curves) parallel sections.

approaches to zero in correspondence to the "large" island approximation of Ref.[28].

The optimal paths, beginning with different phases at the symmetry plane, found for different strength of perturbations and $\sigma_{Ch} = 0.9$, are shown in Fig.3.5. One can see that such paths can be all possible combinations of radial and parallel sections. With increasing perturbation level and approaching to the "large" island limit the parallel sections approach closer and closer to the separatrix. However the final parallel section is always inside the island because (i) at the separatrix the parallel transport becomes less and less efficient by approaching to the X-point and (ii) beyond the island all parallel segments terminate at a finite distance from the RS, i.e., the heat path has to be finished with a radial section contributing strongly to ΔT for $\zeta \gg 1$

Finally, in fig. 3.6 we compare the transport enhancement obtained by considering paths with maximally one and two parallel sections. One can see that the difference between two approaches is not very significant. This is an indication that further increase of the number of parallel sections taken into account, which would lead to a significant rise of computational time, will not noticeably change the results.

In this chapter an analytical approach by R. Fitzpatrick [28], to investigate transport of heat originating from core plasma and passing through non-overlapped magnetic island chains is presented. Due to limited applicability of this approach to the cases of "small" and "large" islands, the 'Optimal path' approach, which is based on the principal of minimum entropy production has been applied for the same problem. This model shows that the effective heat conduction κ_{eff} through islands increases with κ_{\parallel} and with the perturbation level, characterised by σ_{ch} , and reaches a saturation level with κ_{\parallel} , which corresponds to the case where the temperature change in the island disappears. Also with increasing σ_{ch} and κ_{\parallel} , heat is carried predominantly close to the separatrix.

Chapter 4

Transport from internally heated magnetic islands

In a situation where magnetic field perturbations are so strong that the transport parallel to field lines contributes significantly to effective radial heat transport, the magnitude of parallel heat conduction is of principal importance.

In plasmas the dominant contribution to κ_{\parallel} is due to light electrons. If electrons collide with each other often enough, the Spitzer-Härm formula can be used [6]: $\kappa_{\parallel} \approx \kappa_{\parallel}^{SH} = 3.16nV_{th}\lambda$, with $n, V_{th} = \sqrt{T/m}$ and λ being the density, thermal velocity and collision mean free path length of electrons, T and m are their temperature and mass, respectively. With reducing collisionality this approximation becomes inadequate when λ exceeds some per mill of the characteristic dimension for the temperature change, $L_T = 1/|\nabla_{\parallel} \ln T|$, i.e., much earlier than the fluid approximation breaks down. The reason for this is that heat carrying electrons with velocities by a factor of 3 – 4 larger than V_{th} get collisionless [21]. The importance of these suprathermal particles for the heat conduction process manifests also in the fact that contradictory to naive expectations the free-streaming heat flux, $\xi nV_{th}T$ with $\xi \approx 1$, fails to explain the heat transfer in a collisionless case. This has been demonstrated by interpreting laser fusion experiments. These studies [10] have elucidated that a significant heat flux limitation has to be introduced by assuming $0.03 \leq \xi \leq 0.1$. Fokker-Planck simulations of laser produced plasmas [14] and tokamak scrape-off layer with strong recycling [21] have theoretically confirmed this limitation arising due to non-local effects. These effects reduce the perturbation in the distribution function caused by the temperature gradient and being responsible for the heat conduction process [22].

Since it is the uni-direction heat flux one is interested in, one considers a half-Maxwellian distribution function. The distribution function of particles and the parallel free stream heat flux density are given as:

$$q_{\parallel} = \int dv_{\parallel} \int_0^{\infty} v_{\parallel} f(v_{\parallel}, v_{\perp}) \frac{m(v_{\parallel}^2 + v_{\perp}^2)}{2} 2\pi v_{\perp} dv_{\perp} \quad (4.1)$$

$$f(v_{\parallel}, v_{\perp}) = n \left(\frac{m}{2\pi T} \right)^{3/2} \exp \left[-\frac{v_{\parallel}^2 + v_{\perp}^2}{v_{th}^2} \right]$$

With velocity components parallel v_{\parallel} and perpendicular v_{\perp} to the magnetic field, and $v_{th} = (2T/m)^{1/2}$. A half-Maxwellian distribution means $0 \leq v_{\parallel} < \infty$, and full-Maxwellian distribution $-\infty < v_{\parallel} < \infty$, using these in 4.1 as limits or the integral over the v_{\parallel} component of the velocity space gives us the free streaming heat flux q_{\parallel}^{FS} and $q_{\parallel} = 0$, respectively. Consider some plane at a position x in the plasma. Particles from both sides pass and generate net heat flux through this plane. If there is a temperature gradient two situations are possible: (i) particles collide very often and their energy is determined by the temperature at moment of last collision, resulting in normal heat conduction; (ii) particles do not collide often, but there is ambipolar electric field which equalises electron and ion flows, such a field brakes electrons coming to the plane from hotter side and accelerates those from the colder side. This reduces difference in energies of electrons crossing the plane in question and provides a distribution function of particles at the plane position close to a full two-side Maxwellian one with the local temperature. Such a distribution results in a much smaller heat flux in the direction of reducing temperature than a half-Maxwellian one leading to free stream heat flux. This is a qualitative picture of the heat flux limit. In the following sections we elucidate the heat flux limit for tokamak plasmas, by analysing transport of heat from heated magnetic islands.

4.1 Transport through heated magnetic islands

Up to now there is a lack of experimental evidences for the existence of the heat flux limit in tokamak plasmas. Here we analyse from this point of view recent experiments on the tokamak TEXTOR where a tearing mode with the poloidal and toroidal wave numbers m and n equal to 2 and 1, respectively, was triggered by the dynamic ergodic divertor (DED) [48]. The arising magnetic islands were heated by electron cyclotron resonance heating (ECRH) [49] and detailed measurements of the electron temperature profile in islands have been performed with the 2D electron cyclotron emission imaging (ECEI) diagnostic [65]. By interpreting these results the heat conduction components, both perpendicular and parallel to the magnetic field, κ_{\perp} and κ_{\parallel} , respectively, are determined. For this purpose an "optimal path" method is applied and it is demonstrated that the found κ_{\parallel} agrees with the heat flux limit concept. The elucidated limit factor ξ is at the lower edge of the range established earlier in laser plasma experiments [10].

Optimal path method.- In previous analytical theoretical studies of the heat transfer in magnetic islands, see, e.g., Ref. [17, 28] (see previous chapter), a

critical assumption on the temperature perturbation antisymmetry about the resonant surface has been made. This means, in particular, the temperature at the O-point remains the same as in the case without the island. In the experiments in question [65] this assumption is, however, violated since owing to heating of the island interior the temperature profile acquires a maximum in the O-point. In order to evaluate the transport characteristics we apply here the approximate "optimal path" method as proposed in the previous chapter. This method implies that the injected heat is transferred out of the island predominantly along paths providing the smallest temperature change.

There is a direct relation of this approach to the principle of minimum entropy production [4]. As previously, in a plasma region where heat sources are negligibly small the entropy production per unit volume, θ , is given by the relation $\theta = \mathbf{q} \cdot \nabla(\mathbf{1}/\mathbf{T})$, where \mathbf{q} is the heat flux density. By applying this relation to the magnetic island, fig. 4.1, we take into account that the total ECRH power has been launched into the layer being centred on the resonant surface (RS) and much thinner than the island width. Owing to the island rotation the power is distributed nearly homogeneously over the RS. Therefore we assume that the heat deposition layer is infinitesimally thin. The deposited heat flows out from the RS towards both branches of the separatrix with the initial heat flux density $q_s = P_{ECRH} / (8\pi^2 r_s R_s)$, where P_{ECRH} is the heating power, r_s and R_s are the minor and major radius of the RS. By integrating over the volume between the RS and one of the separatrix branches, we get:

$$\int \theta dV = \frac{P_{ECRH}}{2T_s \cdot T_{sep}} \Delta T \quad (4.2)$$

with T_s being the averaged temperature on the RS, T_{sep} the temperature on the separatrix being, according to Fig.2c of Ref.[65], nearly constant, and $\Delta T = T_s - T_{sep}$. Thus, the minimum temperature difference corresponds to the minimum of entropy production.

Consider the part of RS not very close to the X-points. It is logical to assume that optimal paths beginning here can be composed of two parts, see fig. 4.1. The first one is aligned along field lines, since at the RS the parallel transport contributes maximally to the radial heat loss. With the phase angle $\zeta \equiv m\vartheta - n\varphi$ approaching to zero this contribution decreases because the radial flux component is proportional to the radial magnetic field perturbation, $B^r = B_s^r \sin \zeta$. Therefore at some ζ_* the parallel heat transfer becomes inefficient and heat is transported further along the second radial part of the path, perpendicularly to the magnetic field. Near the X-point the chosen very primitive optimal paths can not correspond to reality. The parallel transport at the RS becomes less and less effective since $B^r \rightarrow 0$ when $\zeta \rightarrow \pi$ and an optimal path here should begin from a radial part. Moreover the transport of the main ohmic heat generated in the plasma core takes place also mainly through the X-points, see Fig.2a of Ref. [65]. This makes the composition of the optimal paths even more tricky and the whole concept loses attractiveness due to simplicity compared to a direct numerical treatment, see, e.g., Ref. [60].

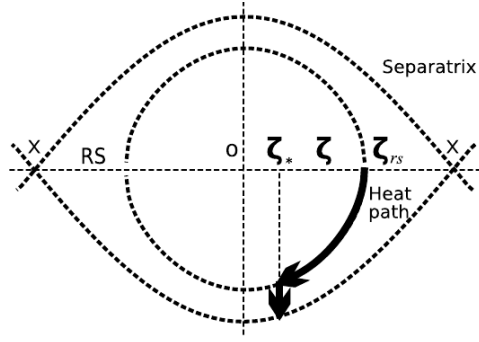


Figure 4.1: Schematic view of a magnetic island with a heat path originating at the resonant surface at the phase angle ζ_{rs} and ending at the separatrix at the phase angle ζ_*

In a quasi-stationary state the heat flux continuity along the parallel part of the path is governed by the equation:

$$q_s = -(\kappa_{\parallel} \nabla_{\parallel} T) \frac{B^r}{B} g = -\kappa_{\parallel} b_r^2 \sin^2 \zeta \frac{\partial T}{\partial x} g \quad (4.3)$$

where $b_r = B_s^r/B$ with B being the total magnetic field, i.e., nearly its toroidal component, g is the metric coefficient taking into account the variation of the cross section of the parallel path part with the phase ζ and distance to the RS [45],

$$x = \frac{w}{2} \sqrt{\frac{\cos \zeta - \cos \zeta_s}{2}}$$

with ζ_s being the initial phase angle of the path at the RS, $w = 4\sqrt{b_r \frac{r_s R}{s_s n}}$ the island width, s_s is the magnetic shear. By considering the intersections of the normal vector with the path borders beginning at ζ_s and $\zeta_s + d\zeta_s$, one gets (see Appendix B)

$$g = \frac{\sin \zeta_s}{\sqrt{\sin^2 \zeta + 32 \left(\frac{r_s}{wm}\right)^2 (\cos \zeta - \cos \zeta_s)}} \quad (4.4)$$

By integrating (4.3) one finds the temperature change along the parallel part of the path:

$$\Delta_{\parallel} T = \frac{q_s r_s}{\kappa_{\parallel} b_r^2 m \sin \zeta_s} \int_{\zeta_*}^{\zeta_s} \frac{\sqrt{1 + \frac{\left(\frac{wm}{r_s}\right)^2 \sin^2 \zeta}{32 \cos \zeta - \cos \zeta_s}}}{\sin \zeta} d\zeta \quad (4.5)$$

The second term under the square root is of importance only for a very small ζ -range, corresponding to $\zeta_r - \zeta \leq \frac{1}{32} \left(\frac{wm}{r_s}\right)^2$. For the typical parameters

in the experiments in question [65], $w = 6\text{cm}$, $m = 2$, $r_s = 30\text{cm}$, this results in $\zeta_r - \zeta \leq 5 \times 10^{-3}$. Thus one can neglect this term and we get:

$$\Delta_{\parallel} T \approx \frac{q_s r_s}{m \kappa_{\parallel} b_r^2} \frac{\ln \left| \frac{\tan \frac{\zeta_s}{2}}{\tan \frac{\zeta_*}{2}} \right|}{\sin \zeta_s} \quad (4.6)$$

At the perpendicular part of the path, $\zeta = \zeta_*$:

$$q_s = -\kappa_{\perp} \frac{\partial T}{\partial x} \quad (4.7)$$

This provides the temperature change:

$$\Delta_{\perp} T = \frac{q_s \Delta x_*}{\kappa_{\perp}} \quad (4.8)$$

with Δx_* being the length of this part, i.e., the distance between the end of the parallel path part and the island separatrix:

$$\Delta x_* = \frac{w}{2} \left(\sqrt{\frac{\cos \zeta_* + 1}{2}} - \sqrt{\frac{\cos \zeta_* - \cos \zeta_s}{2}} \right) \quad (4.9)$$

By introducing the variables $\Omega_* = -\cos \zeta_*$, $\Omega_s = -\cos \zeta_s$ and the parameter $\sigma = 2r_s \kappa_{\perp} / (w m \kappa_{\parallel} b_r^2)$, one obtains for the total temperature variation along the path:

$$\begin{aligned} \Delta T &= \Delta_{\parallel} T + \Delta_{\perp} T \\ &\approx \frac{w q_s}{2 \kappa_{\perp}} \left[\sqrt{\frac{1 - \Omega_*}{2}} - \sqrt{\frac{\Omega_s - \Omega_*}{2}} + \frac{\sigma}{2 \sqrt{1 - \Omega_s^2}} \ln \frac{(1 - \Omega_*)(1 + \Omega_s)}{(1 + \Omega_*)(1 - \Omega_s)} \right] \end{aligned} \quad (4.10)$$

For the optimal path the condition $\partial \Delta T / \partial \Omega_* = 0$ has to be satisfied. This can be reduced to the following equation for Ω_* :

$$\frac{1 - \Omega_*^2}{\sqrt{\Omega_s - \Omega_*}} - \frac{1 - \Omega_*^2}{\sqrt{1 - \Omega_*}} = \frac{\sqrt{8} \sigma}{\sqrt{1 - \Omega_s^2}} \quad (4.11)$$

One can easily see that this equation has always a real solution in the range of interest, $-1 \leq \Omega_* \leq \Omega_s$. Indeed, the left hand side approaches either to zero or to infinity when $\Omega_* \rightarrow -1$ or $\Omega_* \rightarrow \Omega_s$, respectively. Numerically this equation can be solved by iterations.

Figure 4.2 shows the Ω_s -dependence of the value

$$\Theta = \Delta T / \left(\frac{w q_s}{2 \kappa_{\perp}} \right) \quad (4.12)$$

computed for the optimal paths. Since the electron temperature at the external island separatrix is nearly constant, see Fig.2c in Ref. [65], $\Delta T(\Omega_s)$ can be identified with the difference between the experimentally measured temperatures on the resonant surface in the point Ω_s and in the X-point, $\Delta_{\text{exp}} T(\Omega_s) \equiv T_{\text{exp}}(\Omega_s) - T_{\text{exp}}(1)$. The latter one can be directly taken from Fig.4a of Ref.[65].

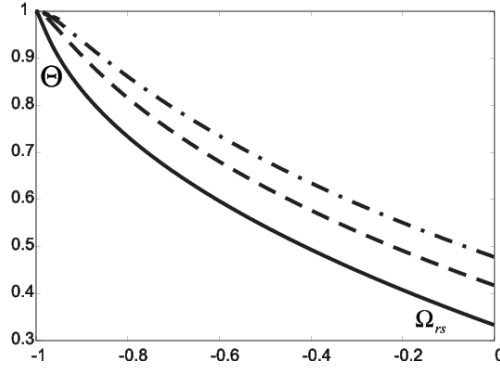


Figure 4.2: The dependence of the dimensionless temperature change along the optimal path, $\Theta = \Delta T / \left(\frac{wq_r}{2\kappa_\perp} \right)$ on the position of the path origin at the RS, $\Omega_{rs} = -\cos\psi_{rs}$, for different magnitudes of the parameter $\sigma = 2r_{rs}\kappa_\perp / (wm\kappa_\parallel b_r^2)$: $\sigma = 0.02$ - solid line, 0.1 - dashed line and 0.2 -dash-dotted line.

The optimal path starting in the O-point consists of a perpendicular part only and for this $\Theta(-1) = 1$. Thus, by identifying $\Delta_\perp T(-1) = \frac{wq_s}{2\kappa_\perp}$ with the experimental temperature difference between the O- and X-points, $\Delta_{\text{exp}} T(-1)$, one can determine the magnitude of κ_\perp :

$$\kappa_\perp \approx \frac{wq_s}{2\Delta_{\text{exp}} T(-1)} \quad (4.13)$$

For the cases displayed in Fig.4a of Ref.[65] this results in κ_\perp within the range $2.7-3 \times 10^{17} \text{ cm}^{-1} \text{ s}^{-1}$. This level is very close to the one determined from the heat transport analysis of TEXTOR ohmic plasmas by means of predictive modelling [25]. One can consider such a closeness as an indication that the presence of islands does not change the perpendicular transport noticeably.

Determination of parallel heat conduction and flux limit factor.- With κ_\perp known one can deduce the parallel heat conduction by comparing the Θ -magnitude for certain Ω_s with those found in the experiment. This possibility can be already seen from Fig.4.2 predicting a significant variation of $\Theta(\Omega_s)$ with the parameter $\sigma \sim \kappa_\perp / \kappa_\parallel$. Fig.4.3 displays the $\Theta(\sigma)$ found for $\zeta_s = \pi/3$. The horizontal lines correspond to the experimental values of $\Theta_{\text{exp}} \equiv \Delta_{\text{exp}} T(\Omega_s) / \Delta_{\text{exp}} T(-1)$ deduced from Fig.4a of Ref.[65] for the cases with the ECRH power of 300 and 400 kW. The vertical lines provide the corresponding values of the parameter σ . With the parameter σ known the parallel heat conduction can be estimated as follows:

$$\kappa_\parallel = \frac{2r_s \kappa_\perp}{\sigma w m b_r^2} \quad (4.14)$$

Here the relative amplitude of the radial magnetic field perturbation, b_r , is assessed from the measured island width w as $b_r = w^2 s_s n / (16r_s R)$ [45]; this

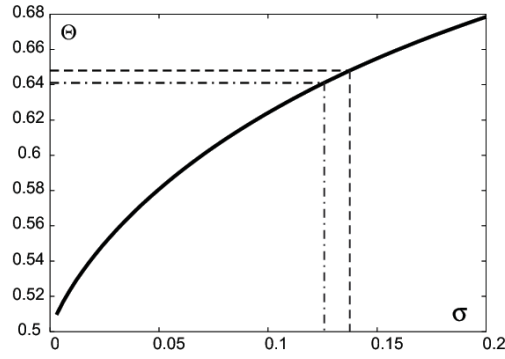


Figure 4.3: Calculated σ -dependence of the dimensionless temperature change Θ along the optimal paths beginning at $\psi_{rs} = \pi/3$, the horizontal lines shows the corresponding experimental values Θ_{exp} for the ECRH heating power of 300 kW (dashed line) and 400 kW (dash-dotted line). The vertical lines provide the corresponding experimental magnitudes of the parameter σ

provides values of 5.8×10^{-4} and 4.0×10^{-4} for $P_{ECRH} = 300$ and 400 kW, respectively. Finally,

$$\kappa_{\parallel} \approx 0.2\kappa_{\parallel}^{SH} \quad (4.15)$$

In order to estimate the flux limiting factor ξ , we use the formula introduced in Ref.[10] and interpolating the heat flux expressions in the collision dominated and collisionless limit cases. This results in the following expression for κ_{\parallel} :

$$\kappa_{\parallel} \approx \kappa_{\parallel}^{SH} / \left(1 + \frac{3.16}{\xi} \frac{\lambda}{L_T} \right) \quad (4.16)$$

The e -folding length for the temperature change along field lines, L_T , is determined as $L_{\parallel}T/\Delta_{\parallel}T$ with

$$L_{\parallel} = \int_{\zeta_*}^{\zeta_s} \frac{B}{B^r} dr = \frac{w}{4\sqrt{2}b_r} \int_{\zeta_*}^{\zeta_s} \frac{d\zeta}{\sqrt{\cos \zeta - \cos \zeta_s}} \quad (4.17)$$

being the length of the parallel path part and $\Delta_{\parallel}T$ is computed according to 4.6. Finally we asses the heat flux limit factor as

$$\xi \approx \frac{3.16}{\kappa_{\parallel}^{SH}/\kappa_{\parallel} - 1} \frac{\lambda}{T} \frac{\Delta_{\parallel}T}{L_{\parallel}} \quad (4.18)$$

For the cases considered above this results in $\xi \approx 0.03$, at the lower edge of the ξ -range, $0.03 \leq \xi \leq 0.1$, found by interpreting laser fusion experiments [10]. However in view of the approximateness of the applied 'optimal path' method this assessment can be considered as being in reasonable agreement

with previous considerations and can be considered as the first experimentally based evidence for the parallel heat flux limit in tokamak plasmas.

4.2 Extension of fitzpatrick's model for heated magnetic islands

Here the results in the previous section obtained by applying the 'Optimal path' method are validated by generalising of the more rigorous theory proposed in [28] (see previous chapter) on the case with plasma heating inside the island. As in the previous section it is assumed that the heat deposition layer is an infinitesimally thin toroidal shell centred on the RS. The deposited heat flows from the RS towards both the plasma core and edge with the heat flux density $q_s = P_{ECRH} / (8\pi^2 r_s R_s)$. Since the ohmic power deposited in the plasma core is transported to the plasma edge mainly through regions close to the X-point of islands [28] it does not change strongly the temperature perturbation produced by the island heating.

By applying the ECRH the temperature in the island O-point rises quickly in roughly 10 *ms* by a maximal 25% and remains nearly constant during the heating phase lasting up to 700 *ms* [65]. Thus the temperature profile in the island can be described by a stationary heat transport equation [28], equation 3.13 above. By including the heat source this equation can be conveniently written in the form:

$$\left(\sin \zeta \frac{\partial}{\partial y} + 4y \frac{\partial}{\partial \zeta} \right) g \left(\sin \zeta \frac{\partial \tilde{T}}{\partial y} + 4y \frac{\partial \tilde{T}}{\partial \zeta} \right) + \sigma \frac{\partial^2 \tilde{T}}{\partial y^2} = -\frac{w^2 Q}{4\kappa_{\parallel} b_r^2} \quad (4.19)$$

where \tilde{T} is the temperature perturbation due to the presence of the island and heating; as in Ref.[28] the island O-point is located at $\zeta = \pi$; $y = 2(r - r_s) / w$ is the distance from the RS measured in the island halfwidths; $\sigma = \kappa_{\perp} / (\kappa_{\parallel} b_r^2)$, Q is the heating power density. By taking into account the heating source localisation at the RS, the temperature perturbation out of the RS is described by 4.19 with zero right hand side. This is similar to 3.13 in Ref.[28] where the critical island width $w_c = w(\sigma/4)^{1/4}$ and radial coordinate $X = 2wy/w_c$ have been used. The heating at the RS defines the boundary condition for \tilde{T} at $y = 0$. This can be found by integrating 4.19 over the infinitesimally thin heating layer or, in a more transparent way, from the heat flux continuity at the border of this layer, $q_s = -\kappa_{\perp} \partial \tilde{T} / \partial r + q_{\parallel}^r$. The former contribution on the right hand side is due to perpendicular heat conduction and the latter one - the radial component of the heat flux along magnetic field lines:

$$q_{\parallel}^r = -\frac{B^r}{B} \kappa_{\parallel} \nabla_{\parallel} \tilde{T} = -\kappa_{\parallel} b_r^2 \sin^2 \zeta \frac{\partial \tilde{T}}{\partial r} \quad (4.20)$$

As a result one has:

$$\frac{\partial \tilde{T}}{\partial y}(0) = -\frac{wq_s}{2\kappa_{\parallel} b_r^2 (\sigma + \sin^2 \zeta)} \quad (4.21)$$

Small island limit.- In this approximation, corresponding to $w \ll w_c$ or $1 \ll \sigma$, the temperature perturbation is primarily just a function of y . This contradicts to the experimental observations [65] clearly exhibiting a significant ζ -dependence in T . Therefore one can reasonably expect that this limit is not realised. However, for the completeness of our analysis we consider it. As in Ref.[28] it is assumed $\tilde{T}(y, \zeta) = \tilde{T}_0(y) + \tilde{T}_1(y) \cos \zeta$ and the functions $\tilde{T}_0(y)$ and $\tilde{T}_1(y)$ are governed by Eqs. 3.14. However, their boundary conditions at the RS are modified. From 4.21 one gets $\frac{\partial \tilde{T}}{\partial y}(0) \approx -\frac{wq_s}{2\kappa_{\perp}} \left(1 - \frac{1}{2\sigma} + \frac{\cos 2\zeta}{2\sigma}\right)$ and:

$$\frac{d\tilde{T}_0}{dy}(0) \approx -\frac{wq_s}{2\kappa_{\perp}}, \quad \frac{d\tilde{T}_1}{dy}(0) \approx 0 \quad (4.22)$$

Thus, in the case in question the function f , controlling the $y(X)$ -dependence of \tilde{T}_1 , see Eq. 3.16, satisfies the boundary condition $df/dy(0) = 0$. Numerical solution of 3.16 from Ref.[28] with this boundary condition gives $f(0) = 2.5$ instead of $f(0) = 0$ adopted in Ref.[28].

ECEI diagnostics [65] allows apparent identification of the poloidal cross-sections of isothermal surfaces in islands. These surfaces are characterised by the radial and poloidal halfwidths x_* and ϑ_* , respectively, corresponding to the phase coordinates $y_* = 2x_*/w$ and $\zeta_* = \pi + m\vartheta_*$ (φ_* is constant for poloidal cross-sections of isotherms and is assumed equal to zero). The radial temperature difference $\delta_r \tilde{T} \approx \tilde{T}(0, \pi) - \tilde{T}(y_*, \pi) \approx -y_* \partial \tilde{T}_0 / \partial y(0) = q_s x_* / \kappa_{\perp}$. With $\delta_r \tilde{T}$, q_s and x_* known from the experiment one can compute the perpendicular heat conduction:

$$\kappa_{\perp} \approx q_s x_* / \delta \tilde{T}_r \quad (4.23)$$

Moreover, on isotherms $\delta_r \tilde{T}$ is equal to $\tilde{T}(0, \pi) - \tilde{T}(0, \zeta_*) \approx -\tilde{T}_1(0) (1 + \cos \zeta_*)$ and this results in:

$$\sigma = \left[\frac{f(0) (1 + \cos \zeta_*) w}{8\sqrt{2}x_*} \right]^4 \quad (4.24)$$

As an example we consider the case of $P_{ECRH} = 300kW$ in Ref.[65] and the isotherm with $\delta_r \tilde{T} \approx 35eV$. This is characterised by $x_* = 2.7cm$ and $\vartheta_* = 0.83$. For typical $q_s \approx 0.7W/cm^2$ and $w = 6cm$, one obtains $\kappa_{\perp} \approx 3.4 \cdot 10^{17} cm^{-1} s^{-1}$ and $\sigma \approx 0.08$. As it was expected, the latter is in contradiction to the small island approximation, $\sigma \gg 1$.

Large island limit. - This limit corresponds to $\sigma < 1$ and parallel heat conduction dominating over the perpendicular one and heating. In this case the temperature perturbation has to be, in the first approximation, constant on island magnetic surfaces corresponding to a constant $\Omega = 2y^2 + \cos \zeta$. Indeed, by assuming $\tilde{T} = T_0 y^2 + T_1 \cos \zeta$, where T_0 and T_1 are some constant

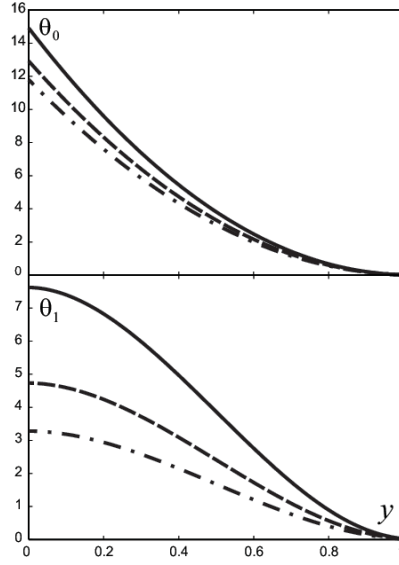


Figure 4.4: Functions $\theta_0(y)$ and $\theta_1(y)$ calculated for $\alpha = 24$, $\sigma = 0.5$ (solid curves), $\alpha = 20$, $\sigma = 0.2$ (dashed curves), and $\alpha = 17$, $\sigma = 0.05$ (dash-dotted curves), characteristic for the ECRH experiments in Ref. [65] with heating power of 400, 300 and 200 kW, respectively.

factors, and substituting this into 4.19 where $\kappa_{\parallel} \rightarrow \infty$ and, thus, $\sigma \rightarrow 0$, one obtains $T_1 = T_0/2$ and $\tilde{T} = \Omega T_0/2$. By considering the effect of perpendicular heat conduction and heating as small, we look for the solution of 4.19 in the form $\tilde{T} = \Omega T_0/2 + \tilde{T}_2$, where $\tilde{T}_2(y, \zeta) \approx \Theta(y) \Psi(\zeta)$. The requirement that \tilde{T} has to satisfy the boundary condition 4.21 at the RS results in

$$\tilde{T} = \frac{T_0}{2} \Omega + \frac{wq_s}{2\kappa_{\parallel} b_r^2} \frac{\Theta(y)}{\sigma + \sin^2 \zeta} \quad (4.25)$$

with the following boundary condition for $\Theta(y)$:

$$\frac{d\Theta}{dy}(0) = -1 \quad (4.26)$$

The equation, governing Θ , is obtained by substituting \tilde{T} from 4.25 into 4.19 and averaging over the phase angle ζ . This provides:

$$\frac{d}{dy} \left(\gamma \frac{d\Theta}{dy} \right) = -\frac{2\pi T_0 \kappa_{\perp}}{wq_s} \quad (4.27)$$

with:

$$\gamma(y) = \int_0^1 \frac{(1-s^2) ds}{\sqrt{\alpha^2 y^2 + 1 - s^2} (\sigma + 1 - s^2)} \quad (4.28)$$

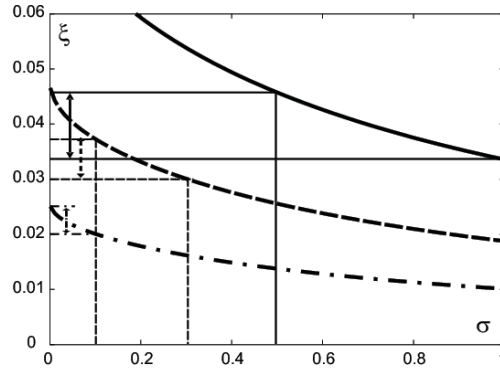


Figure 4.5: σ -dependence of the heat flux limit ξ calculated according to Eq. 4.37 for the condition of ECRH in TEXTOR with different power levels of 400 (solid curve), 300 (dashed curve) and 200 kW (dash-dotted curve). The vertical lines of the same pattern indicate the σ -ranges determined from the experimental data of Ref.[65] according to Eq. 4.32; the vertical arrows - the corresponding ξ -intervals.

where $\alpha = 8r/(mw)$. According to [28] all $\tilde{T}_{\nu \geq 2}$ subside fast with the distance from the island and we assume

$$\Theta(1) = 0 \quad (4.29)$$

as the second boundary condition for Θ . The integration provides:

$$\Theta = \theta_0(y) + \frac{2\pi T_0 \kappa_{\perp}}{wq_s} \theta_1(y) \quad (4.30)$$

with $\theta_0(y) = \int_y^1 \frac{\gamma(0)}{\gamma(y)} dy$ and $\theta_1(y) = \int_y^1 \frac{y dy}{\gamma(y)}$ shown in Fig. 4.4 for different combinations of the parameters α and σ characteristic for ECRH of different power levels in TEXTOR [65].

In order to determine the parameters T_0 , κ_{\perp} and σ we calculate according to 4.25 and 4.30 the differences in the temperature perturbation in four points on the RS, $y = 0$: $\Omega_{i=1-4} = -0.8, -0.4, 0$, and 0.4 . By equating these to the experimental values $\Delta_{\Omega_i, \Omega_j}$ taken from Fig.4 of Ref. [65], one gets:

$$T_0 = -2.5\Delta_{-0.4,0.4}, \quad (4.31)$$

$$\sigma = \frac{\Delta_{-0.8,0} - 9/8\Delta_{-0.8,0.4} + 11/16\Delta_{-0.4,0.4}}{4/3\Delta_{-0.8,0.4} - \Delta_{-0.4,0.4} - \Delta_{-0.8,0}} \quad (4.32)$$

and

$$\kappa_{\perp} \approx \frac{0.32\theta_0(0)wq_s}{\left[\frac{(\Delta_{-0.8,0} - \Delta_{-0.4,0.4})(\sigma + 1.36 + 0.36/\sigma) + 5\theta_0(1)\Delta_{-0.4,0.4}}{\sigma} \right]} \quad (4.33)$$

With the temperature profiles from Ref.[65] one obtains σ in the ranges $0 - 0.1$, $0.1 - 0.3$, and $0.5 - 1$, for the ECRH power of 200, 300 and 400 kW, respectively. Thus, the applicability condition for the large island approximation, $\sigma < 1$, is fulfilled. The perpendicular heat conduction κ_{\perp} is within the range $2.5 - 3.1 \times 10^{17} \text{cm}^{-1} \text{s}^{-1}$, i.e., close to the level found in the small island approximation. By the 'Optimal path method' one can see, in the case of the temperature perturbation being exactly constant on magnetic surfaces, $\tilde{T} \sim \Omega$, the σ and transport coefficients given by 4.32 and 4.33 are undefined. Thus, namely the deviation from such a constancy provides a possibility to determine κ_{\perp} and κ_{\parallel} .

Heat flux limit factor- As a example we consider the surface with $\Omega = 0$ and the field line part between the RS and $y = 0.5$. In such a case an assesment of $\Delta_{\parallel} T$ from 4.25, 4.30 and fig. 4.4 yields

$$\Delta_{\parallel} T \approx \frac{\theta_0(0) - \theta_0(0.5)}{\sigma + 1} \frac{wq_s}{2\kappa_{\parallel} b_r^2} \approx \frac{0.37\theta_0(0)}{\sigma + 1} \frac{wq_s}{\kappa_{\parallel} b_r^2} \quad (4.34)$$

and for L_{\parallel} one has from 4.17:

$$L_{\parallel} = \int_{r_s}^{r_s+0.25w} \frac{B}{B^r} dr = \frac{w}{2b_r} \int_0^{0.5} \frac{dy}{\sqrt{1-4y^2}} \approx 0.26w/b_r \quad (4.35)$$

For collisionless plasmas in question the second term in the brackets in Eq. 4.16 is much larger than 1. Therefore for the heat flux limit factor ξ we obtain:

$$\xi \approx \frac{3.16\kappa_{\parallel}}{\kappa_{\parallel}^{SH}} \frac{\lambda}{L_T} \approx \frac{1.42q_s\theta_0(0)}{(\sigma + 1)nV_{th}Tb_r} \quad (4.36)$$

The relative amplitude of the radial magnetic field perturbation, b_r , is estimated from the measured island width w according to the formula [28]: $b_r = (w/4)^2 \widehat{s}_s N / (r_s R_s)$. At the RS with $r_s \approx 30 \text{cm}$ the magnetic shear $\widehat{s}_s \approx 1$, and we obtain ξ with parameters in practical units, see the square brackets:

$$\xi \approx \frac{0.14\theta_0(0)}{\sigma + 1} \frac{P_{ECRH}^{[MW]}}{n_{[10^{13} \text{cm}^{-3}]} \cdot T_{[keV]}^{1.5} \cdot w_{[cm]}^2} \quad (4.37)$$

Figure 4.5 demonstrates the σ - dependences of ξ computed according to 4.37 for different levels of the ECRH power and the temperature profiles on the RS from Fig.4 of Ref. [65]. The corresponding σ -intervals and resulting ξ -ranges are shown by vertical lines and arrows, respectively. In spite of the broad range of the parameter σ , the found ξ -factor varies in a relatively narrow interval from 0.02 to 0.045. These values are close to those obtained above by the optimal path method and validate the results obtained in the previous section. Hence, the heat flux limit obtained by application of both approaches to experimental observations from TEXTOR, is in good agreement with that found in laser fusion experiments [10].

Chapter 5

ELMs

Here we investigate transport of heat and particles due to another important class of MHD instabilities called ELMs, which are localised in the edge region of tokamak plasmas.

5.1 Phenomenology and mechanisms

High confinement mode (H-mode) operation is still nominated as the reference inductive operational scenario for ITER [13, 24, 35, 36]. MHD instabilities called edge localised modes (ELMs) driven by the steep gradients of edge temperature and density are observed in such H-mode plasmas [15, 16]. They expel periodically energy and particles from the plasma edge. The important role of ELMs is to provide stationary H-mode discharges (ELM-y H-mode), and help to control the inventory of the plasma [30, 51].

Profiles of an edge transport barrier (ETB) in H-modes of the density and/or temperature, and hence the plasma pressure, indicate steep gradient in the plasma region at around normalised radius of $r/a \sim 0.9 - 1.0$ (so called pedestal), while no pedestal structure is seen at low confinement mode (L-mode). Various theory-based transport models, show an increase in Q_{DT} with T_{ped} . According to such estimates, ITER will need a very high pedestal temperature of $T_{ped} \sim 3 - 5\text{KeV}$ to obtain $Q_{DT} \geq 10$ at the plasma current $I_p = 15\text{MA}$ and the auxiliary heating power $P_{aux} = 40\text{MW}$ with electron density normalised by Greenwald density $n_e/n_{GW} = 0.85$.

Once the pedestal pressure or its gradient reaches its own limit by MHD instability, ELM crash occurs, ejecting plasma energy and particles towards the scrape-off layer (SOL) region, and recovers rapidly through a transport process. ELMs affect only the plasma peripheral region ($r/a \geq 0.7 - 0.8$, roughly), and the core confinement remains undamaged. Periodic ELM crash has a potential for controlling plasma density and impurity accumulation in the plasma core, allowing a quasi-stationary operation, though induced energy and particles could potentially limit the divertor and, possibly, first-wall lifetime. Temporal analysis from different locations in many tokamaks give insight into transport physics of ELMs [52]. ELMs form in the LFS (low field side) with

a typical ELM duration $\tau_{ELM} \sim 100 - 200 \mu s$, which has a finite poloidal and radial extent. Then the ELM plasma moves near the last closed flux surface (LCFS) as a perpendicular transport across the SOL, and it also propagates parallel to the magnetic field lines with the ion transport time from pedestal to divertor $\tau_{ELM} = L_c/c_s$, depending on the pedestal parameters. Finally, it spreads radially as it moves towards the divertor/first-wall.

From the variety of edge localised modes occurring in toroidal fusion plasma, three distinct types can be classified [30].

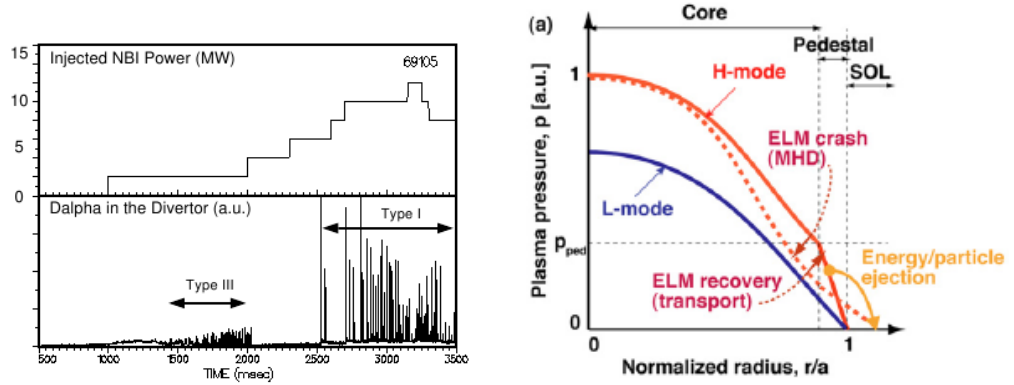


Figure 5.1: ELMs experimental observations (left) [30] - as the NBI power is increased the Dalphi emission in the divertor shows a transition from Type III ELMs, ELM free phase to Type I ELMs. ELMs pedestal (right) [67] schematic view of the events at the pedestal - with increasing input power a transition take place from L-mode to ELM-y H-mode, where relaxation of pedestal pressure gradient takes place through pulsed ejection of heat and particles

Dithering cycles- Due to bifurcated character of the H-mode, at $P_{sep} \approx P_{thr}^{LH}$, repetitive L-H-L transitions can occur. Dithering cycles show no magnetic precursor oscillation; the level of turbulence during the temporary L-phase does not significantly exceed that of the L-phase at $P_{sep} \leq P_{thr}^{LH}$.

Type III ELMs- The ELM repetition frequency decreases with the energy flux through the separatrix in excess of P_{thr} i.e. $d\nu_{ELM}/dP_{sep} < 0$. A coherent magnetic precursor oscillation with toroidal mode number $n \approx 5 - 10$ and poloidal mode number $m \approx 10 - 15$ is observed on magnetic probes located close to the plasma. During the ELM, there is a high level of magnetic fluctuations. Type III ELMs are stabilised at high edge temperatures, indicating that they are connected with resistive MHD instabilities. Candidates for the type III ELM mechanism include resistive ballooning modes, coupled to a global instability such as the free boundary mode (peeling mode).

Type I ELMs- The ELM repetition frequency ν_{ELM} increases with the energy flux through the separatrix, i.e. $d\nu_{ELM}/dP_{sep} > 0$. There are indications that type I precursor activity has even higher mode numbers than type III precursors. The power dependence and results from magnetic stability anal-

ysis indicate that type I ELMs are linked to ideal MHD instabilities. Type I ELMs may be stabilised by opening access of the plasma edge to the second stability ballooning region. However, the ideal ballooning criterion seems to be a necessary but not sufficient condition for a type I ELM. A plausible candidate for Type I ELMs is therefore a combination of ideal ballooning modes coupled to global ideal MHD instability such as an ideal kink (peeling).

The power release between ELMs comes dominantly from the low field side, and most of it is deposited on the outboard divertor. ELM energy is also released preferentially near the outer midplane consistent with the peeling-ballooning mode characteristics. The SOL transport during ELMs exhibits several interesting features as well. An asymmetry is observed in the energy deposition into the inner divertor compared with the outer divertor, with a higher fraction deposited on the inner target. The duration of the ELM power pulse seems to be independent of the ELM MHD duration, τ_{MHD}^{ELM} , and thus the transport of energy along the field plays an important role on the ELM energy losses, this forms another basis for extrapolation of the ELM energy loss to ITER. The characteristic timescale τ_{IR}^{ELM} , defined as the duration of power increase from 10% above the initial value to 100% of the maximum measured value, shows good correlation with τ_{\parallel}^{ELM} , suggesting a convective transport along open field lines towards the divertor target. Based on expected pedestal parameters for ITER, one could estimate for ITER $\tau_{IR}^{ELM} \sim 400 \pm 150 \mu s$. Only a fraction of the target load energy arrives during τ_{IR}^{ELM} , while the rest arrives in the tail after the maximum heat flux. Also, it is observed that about 50–80% of the ELM energy arrives at the divertor target, which means a part of the ELM energy reaches the main chamber wall, which may have strong implication for ITER such as the choice of the first-wall materials.

Observations on diverse tokamak devices demonstrate that the losses of plasma energy provoked by type I Edge Localised Modes $\Delta W_{elm}/W_{ped}$ shows good correlation with collisionality, increasing significantly with decreasing plasma collisionality ν^* [41]. The physics basis for this approach may come from the peeling-ballooning model for the ELM and the influence of collisionality on the edge bootstrap current and change in the associated MHD unstable mode structure. In ITER, $\nu^* \sim 0.06$, unacceptably large ELM energy loss of around 20% of pedestal stored energy is expected, which is significantly larger than ITER maximum tolerable ELM size of around $\Delta W_{elm}/W_{ped} \sim 5 - 10\%$. However, there is also a large variation in $\Delta W_{elm}/W_{ped}$ even at fixed collisionality, which may be due to the nonlinear nature of ELM instability and its evolution, and hence such an extrapolation remains uncertain. Experiments with fixed collisionality at JT-60U, show variations of $\Delta W_{elm}/W_{ped}$ with counter-NBI and plasma volume. Namely, $\Delta W_{elm}/W_{ped}$ decreases when scanning the direction of the momentum injection from co-, balanced to counter directions and when increasing the volume of the plasma.

At low collisionality the relative drop in the thermal energy clearly exceeds the corresponding level for particles and such ELMs are called "conductive". With increasing collisionality the energy drop decreases immensely and on approaching the H-mode density limit it becomes comparable or even lower

than the relative particle loss and such ELMs are referred to as "convective".

On the one hand, an understanding of mechanisms for ELMs and firm predictions for the absolute level of particle and energy losses, caused by them, are important for the future ITER, considering the large transient heat loads to material surfaces and constraints placed on the edge pedestal height due to ELMs. On the other hand, active ELM control techniques are also being developed, such as pellet triggered ELM pace making on ASDEX Upgrade [43], edge ergodization with external coils on DIII-D [55, 57] and JET, vertical motion on TCV [42] and dynamic ergodic divertor on TEXTOR [56, 48], whose feasibility for ITER ELM control are currently studied [74].

In this section we have seen various experimentally observed characteristics of ELMs, which give us some insight to the possible physics behind their trigger and transport mechanisms, dependence on various parameters, and their effect on the tokamak. We now proceed to give an overview of various models that have been proposed to explain the ELM phenomenology.

5.2 Theories

The pedestal region of H-mode tokamak plasmas is characterised by a sharp pressure gradient and consequent large bootstrap current. The peeling-ballooning model posits that the free energy in the large pressure gradient and current drives coupled peeling-ballooning modes that constrain the maximum pressure at the top of the pedestal region and trigger ELMs. Peeling-ballooning theory was first developed in the local high toroidal mode number (n) limit [32], and later extended to incorporate intermediate- n and nonlocality [39]. While the high- n ideal ballooning limit does correspond well to the observed type I ELM threshold in some regimes, experiments with high edge spatial resolution do show that the observed pressure gradients do not scale as expected from ideal ballooning theory [34].

The sharp pressure gradients in H-mode pedestal can drive strong bootstrap currents which play complex dual role in the stability picture. On the one hand, edge current provides a source of free energy which drives external kink or peeling modes in the edge. On the other hand, edge currents reduces the magnetic shear s in the pedestal, which stabilises high- n ballooning modes, and increases the MHD pressure gradient threshold.

The stability limits imposed by coupled peeling-ballooning modes can be envisioned schematically 5.2. At least three types of MHD driven ELM cycle can be imagined for this type of stability boundary. In each case, power flowing from the core causes the pedestal gradient to rise between ELMs on a transport time scale, with current (mostly bootstrap) generally rising more slowly towards its steady state value. In figure 5.2 The cycle (iii) will occur at low density and low input power, such that the current rises to exceed the peeling limit well before the pressure gradient reaches the ballooning limit. These ELMs are expected to be small, both because the peeling mode triggering them have narrow mode structures, and because they occur at low pedestal

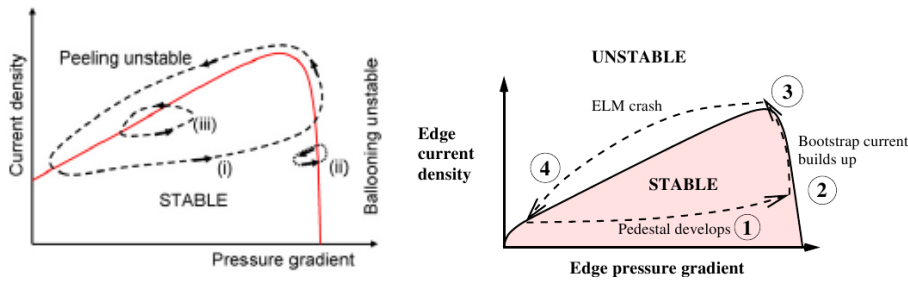


Figure 5.2: ELMs cycle (left) [59] - (i), (ii), (iii) represent coupled peeling-ballooning (Type I), ballooning (Type II) and peeling cycles (Type III), respectively. Type I ELM (right) [53]

height. The ELM frequency is expected to decrease with input power, because the pressure gradient will rise more quickly, stabilising the peeling mode. Hence this cycle provides a model for the low density variety of type III ELMs (high density type III ELMs are likely driven by resistive modes). At higher power and low density, cycle (i) will occur, generating large ELMs both because the relatively low- n peeling-ballooning modes have a broad radial structure, and because the initial pedestal pressure collapse will leave the pedestal in the unstable domain until the current relaxes to a much lower value. This cycle's frequency will increase with input power, and it provides a model for large type I ELMs. Finally, at larger power, where the total steady state current at the pressure limit does not exceed the peeling limit ($J_{tot} < J_{peel}$), cycle (ii) occurs. This can occur either at high density, where high collisionality leads to a low J_{bs} , or it can occur at somewhat lower density when the peeling limit is high due to strong shaping or large magnetic shear. This cycle is expected to yield relatively small ELMs because both the high- n ballooning modes which are most unstable at low current, and the intermediate- n modes most unstable for high- q high- δ type-II ELM cases, tend to have narrow mode structures, and because the pressure loss immediately following the ELM crash returns the pedestal to a stable region of parameter space. In the above stability studies the density and temperature profile shapes, and therefore the pedestal width, have been held fixed.

Several 2D MHD codes have been developed to study these nonlocal, finite- n peeling, ballooning and coupled peeling-ballooning modes [40]. A finite growth rate threshold is typically used to account for diamagnetic stabilisation. For typical H-mode edge parameters, the limiting instability is usually an intermediate n ($n \sim 3 - 30$) coupled peeling-ballooning mode, though pure ballooning modes can be limiting at high collisionality, and pure kink/peeling modes at low collisionality. Such linear models are useful for understanding ELM onset conditions and pedestal constraints. Nonlinear simulations have also been made to understand ELMs associated particle and heat losses. One such simulation shows [50] that the onset conditions for ELMs are found to be similar to those calculated with linear MHD codes. A two-

pronged model for energy and particle losses is proposed (1) Conduits: the filaments remain connected at the top and bottom to the hot core plasma, fast local diffusion and secondary instabilities along the outer portion of the filament allow fast parallel losses of heat and particles (2) Barrier collapse: the growth and propagation of the mode collapses the flow shear in the edge region and weakens or destroys the ETB, resulting in a temporary return of L-mode transport until the barrier recovers.

While a clearer picture of the physics behind ELMs is emerging, efforts are made to understand the physics of ELM-free regimes in the low-collisionality regime like QH-mode and ELMs suppression via RMP. A proposed model [70] posits that in the QH mode the EHO, a typically $n \sim 1 - 5$ mode observed in most QH plasmas, is a saturated kink/peeling mode, which is destabilised by edge current and rotation. As its eigenmode grows to large amplitude, it creates significant magnetic perturbations which allow particle and current transport across the field. In addition, the large amplitude mode applies drag on rotation, allowing the nonlinear mode to damp its drive and saturate at finite amplitude, thus not growing explosively like an ELM. This allows steady state in all important transport channels and leads to a steady quiescent edge. The RMP play a similar role to the EHO, driving substantial transport, keeping the edge parameters below the peeling-ballooning stability boundary, and allowing an approximately steady state edge.

The interest in modelling ELMs phenomenology is evident from the numerous efforts made in investigating aspects of MHD instability [40, 70], and integrated modelling combining transport [47, 54, 71, 72, 73, 76, 77]. A model introduced recently [63], providing predictions for these losses, has been modified as part of this thesis. It is based on a well established idea that type I ELMs are generated by ballooning-peeling ideal MHD modes, developing when the pressure gradient in the edge transport barrier (ETB) surmounts the critical level [31, 39]. These modes produce a radial component of the magnetic field and, therefore, perturbed field lines lean in the radial direction. The radial inhomogeneity of the plasma parameters in the ETB results in flows along such field lines increasing the particle and energy transport during type I ELMs. It has been put forward in Ref.[63] that the electron heat conduction along perturbed field lines can be of eminent importance for the energy loss by ELMs and explain the decrease of these losses with increasing collisionality, in qualitative agreement with observations. However, a relatively high, of 0.2, heat flux limit factor, giving the ratio of the parallel heat conduction flux in a collisionless plasma to that transferred by free streaming electrons, has been adopted in Ref.[63]. This exceeds noticeably a level of 0.03 elucidated very recently [68] from magnetic island heating experiments [65] (see previous chapter), which is in agreement with the results of previous investigations, Refs. [10, 14, 21]. Thus, the energy loss by ELMs with electron heat conduction was noticeably overestimated in Ref. [63] and is, actually, inadequate to explain the experimental data.

Recent observations on ELMs exhibit that ion convection physics is likely to play an important or even dominant role in ELM energy transport [67].

In the following section, the model for convective heat losses during the ELM associated with the escape from the plasma of ions of diverse velocities and energies, including suprathermal particles, developed during this thesis work is presented. These losses exceed significantly those due to electron heat conduction being assessed with more realistic heat flux limit factor. The collisionality dependence of the total energy loss per ELM and of the width of the edge region where these losses are localised is in qualitative and quantitative agreement with experimental findings [41]. Moreover, the maximum loss intensity is located at the barrier top and the averaged energy of escaping ions is close to the top temperature, as it is observed in experiments [41].

5.3 Model for ion convective heat loss during ELM crash

The contribution of thermal particles, those with the temperature at the separatrix, to the convective heat losses by ELMs was accounted for in the previous model [63]. However, observations show that the energy of particles expelled from the plasma during ELMs is probably significantly higher and is of the temperature at the ETB top [67]. Thus, the energy of suprathermal particles escaping along field lines perturbed by MHD modes from deeper plasma regions may also contribute substantially to the energy loss. Similar to the electron heat conduction this loss channel is expected to be decreasing with increasing plasma collisionality, in accord with experimental observations.

We consider ions, which start to move at time $t = 0$, when the magnetic field lines are inclined by MHD-perturbations, from different initial radial positions r inside the separatrix, $0 \leq r \leq a$, with diverse initial values ϵ and U of the perpendicular energy ϵ and parallel velocity V , respectively. The variation of the particle radial position x in time is governed by the kinematic equation:

$$\frac{dx}{dt} = \alpha V \quad (5.1)$$

Here α is the characteristic inclination angle of perturbed field lines in the radial direction. The typical level of α achieved on the stage of linear MHD instability has been roughly estimated in Ref. [63] and is of the order of $3 - 5 \times 10^{-4}$. In this section α is assumed to be constant in space and time, during the ELM duration time τ_{ELM} . In the next section, the computations will be generalised on the case of $\alpha(t)$, calculated by considering the time variation of magnetic field radial component and density at ETB top.

The variation of the parallel velocity V and perpendicular energy ϵ in time is governed by the momentum and energy balance equations where coulomb collisions with thermal background particles are taken into account [5]:

$$\frac{dV}{dt} = \frac{e}{m_i} E - \frac{2\mu}{\tau_1} V \quad (5.2)$$

and

$$\frac{d\varepsilon}{dt} = \frac{2}{\tau_1} \left[(\mu + \mu') \frac{m_i V^2}{2} - (\mu - \mu') \varepsilon \right] \quad (5.3)$$

where e is the electric charge of the plasma ions of a hydrogen isotope with the mass m_i , μ and τ_1 are the Maxwell integral and relaxation time (Appendix C), respectively, see Ref. [5], computed with the local plasma parameters. The parallel electric field E is estimated from the force balance for electrons along the field lines, between the electric field force and pressure gradient:

$$0 = -enE - \alpha \frac{d(nT)}{dx} \quad (5.4)$$

The profiles of the plasma density n and temperature T at the edge are assumed piecewise linear ones with sharp gradients in the ETB: core plasma, $x \leq a - \Delta_b$,

$$\begin{aligned} n &= n_b, \\ T &= T_c - (T_c - T_b) \frac{x}{a - \Delta_b}; \end{aligned}$$

edge transport barrier, $x \geq a - \Delta_b$,

$$\begin{aligned} n &= n_s + (n_b - n_s) \frac{a - x}{\Delta_b}, \\ T &= T_s + (T_b - T_s) \frac{a - x}{\Delta_b}, \end{aligned}$$

where the subscripts s, b and c indicate the parameter values at the separatrix, the barrier top and in the plasma core, and Δ_b is the barrier width. Equations 5.1, 5.2 and 5.3 are integrated numerically with the initial conditions $x(t=0) = r$, $V(t=0) = U$ and $\varepsilon(t=0) = \epsilon$ till either the travelling time t exceeds the ELM characteristic duration time τ_{ELM} or the particle escapes through the separatrix, i.e., $x = a$ for $t = t_a < \tau_{ELM}$. In the latter case the energy of the escaping particles is added to the total energy loss:

$$\begin{aligned} \Delta W_{ELM}^{conv} &= S_{sep} \int_0^a dr \int_{-U_{max}}^{U_{max}} dU \int_{-\epsilon_{max}}^{\epsilon_{max}} d\epsilon \frac{2\epsilon}{m_i} \frac{1}{\sqrt{\pi}} \frac{n(r)}{V_T^3(r)} \\ &\times \exp \left[-\frac{U^2}{V_T^2(r)} - \frac{\epsilon}{T(r)} \right] \left(\frac{m_i V_a^2}{2} + \varepsilon_a \right) \end{aligned} \quad (5.5)$$

where $S_{sep} = 4\pi^2 \kappa a R$ is the separatrix area with R and κ being the plasma major radius and the separatrix elongation, respectively, $V_T = \sqrt{2T/m_i}$ is ion thermal velocity, V_a and ε_a are the parallel velocity and perpendicular energy of the particle attained at the separatrix; a Maxwellian distribution over the initial parameters U and ϵ is assumed. Typically $U_{max} = 6V_T^b$ and $\epsilon_{max} = 11T_b$ are adopted, these values have been obtained as a result of several calculations

which indicate that the energy loss does not change on further increase in the considered range of these parameters.

It is worth indicating that the computational effort required for the calculation of ΔW_{conv} with a given accuracy was minimised eminently by use of some numerical techniques, which permitted to operate with larger steps of t, U, ϵ and r . In particular, the parametric dependence of the integrand in 5.5 has been interpolated by a cubic spline determined by its values for four consecutive parameter values.

Pedestal energy loss. - The relative loss per ELM of the pedestal energy, defined as the thermal energy in the whole plasma volume calculated at the pedestal density n_b and temperature T_b , $W_{ped} = S_{sep}a/2 \times 3n_bT_b$, was introduced in Ref.[41] as a figure of merit:

$$\frac{\Delta W_{ELM}}{W_{ped}} = \frac{\Delta W_{ELM}^{conv}}{W_{ped}} + \frac{\Delta W_{ELM}^{cond}}{W_{ped}} \quad (5.6)$$

According to Ref.[63] the latter contribution from the electron heat conduction can be asserted as

$$\frac{\Delta W_{ELM}^{cond}}{W_{ped}} \approx 0.23 \frac{1 + \kappa}{\kappa} \frac{\tau_{ELM} \sqrt{2T_b/m_e}}{a \left(\frac{\nu^*}{\nu_0} + \frac{1}{\xi_{FS}} \right)} \alpha \quad (5.7)$$

where $\nu^* \equiv qR(R/a)^{3/2}/\lambda_b$ is the collisionality parameter, wherein λ_b is the mean free path length determined for the plasma parameters at the barrier top, $\nu_0 = (1.9\alpha qR/\Delta_b)(R/a)^{3/2}$, q is the typical safety factor at the edge, and ξ_{FS} the heat flux limit factor.

One can see that in collisionless plasmas with $\nu^*/\nu_0 \ll 1/\xi_{FS}$ the conductive contribution to the energy loss scales proportionally to ξ_{FS} . With $\xi_{FS} \approx 0.2$ used in Ref. [63], this contribution alone has been enough to explain well the experimentally found magnitude and collisionality dependence of $\Delta W_{elm}/W_{ped}$. However recent studies [68] on interpretation of the magnetic island heating experiments [65] have provided a ξ_{FS} -value a factor of 5-10 lower (see previous chapter). This means that the maximum level of the conductive loss contribution has to be reduced by this factor and should be significantly lower than it was predicted in Ref. [63]. The quantitative assessment in the next section shows that the convective contribution considered here is normally much larger and most probably is responsible for the experimentally measured level of losses.

Results. - Parameters characteristic for the ELMy H-mode discharges in JET have been assumed in calculations [41, 69]: $R = 3m$, $a = 0.9m$, $\kappa = 1.6$, $q = 4$, $\Delta_b = 0.05m$, $n_b/n_s = 2$, and $Z_{eff} = 2$. By taking into account that the time averaged plasma parameters at the barrier top have to satisfy the threshold condition for ballooning-peeling MHD modes [31, 39]

$$\frac{n_b T_b}{\Delta_b} \approx \frac{B^2 \alpha_{cr}}{16\pi R q^2}$$

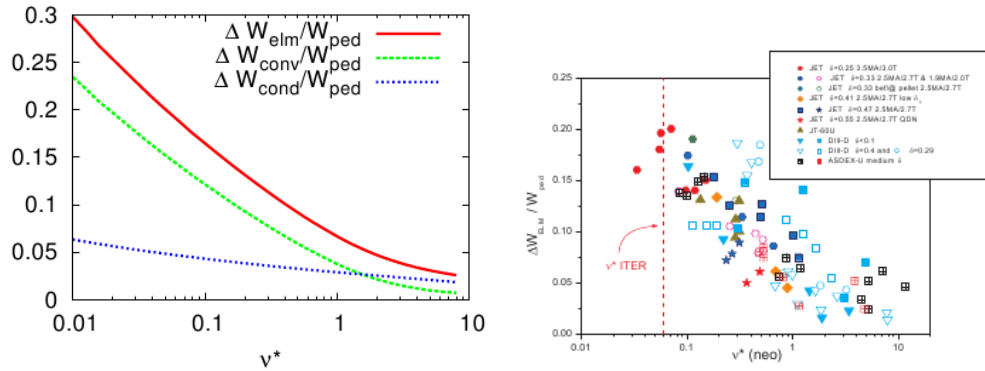


Figure 5.3: Collisionality dependence of energy loss during ELMs - as seen from the model (left) and in good agreement with experiments (right) [41]. $\Delta W_{ELM}/W_{ped}$ decreases with ν^* , and the major contribution comes from $\Delta W_{conv}/W_{ped}$, while the $\Delta W_{cond}/W_{ped}$ contribution remains small

where $\alpha_{cr} \approx 4 - 5$, it can be shown, see, e.g., Ref.[63], that they scale with the collisionality parameter ν^* at the ETB top as follows:

$$n_b = n_{b0}(\nu^*/\nu_0^*)^{1/3}, T_b = T_{b0}(\nu_0^*/\nu^*)^{1/3} \quad (5.8)$$

where n_{b0}, T_{b0} and ν_0^* are the reference parameters taken henceforth equal to $3 \times 10^{19} m^{-3}$, $2 keV$ and 0.06 , respectively[69]. According to experimental observations [41] the characteristic ELM duration time $\tau_{ELM} \approx 200 \mu s$ and is nearly independent of ν^* .

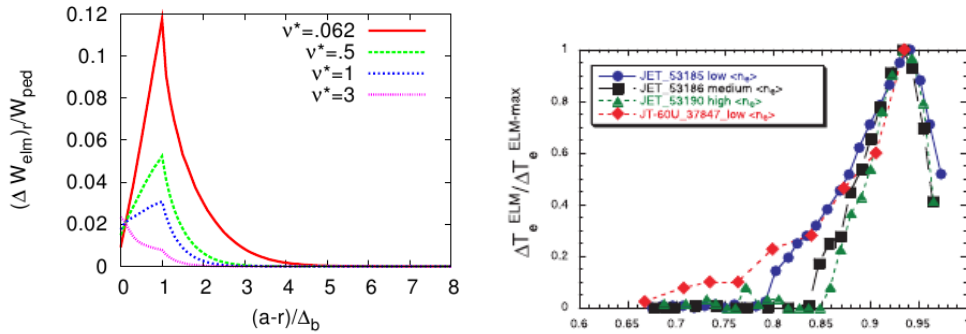


Figure 5.4: Energy loss contribution from different radial locations $w_{ELM}^{conv} = |dW_{ELM}^{conv}/dr|$ (left) as obtained from the model - w_{ELM}^{conv} peaks at the ETB top and is clustered around the barrier region, the size of the loss region decreases with ν^* . Temperature drop in the ETB as observed in experiments [41].

Figure 5.3 shows the calculated collisionality dependences of the net energy loss per ELM, ΔW_{ELM} , the convective and conductive contributions to it,

ΔW_{ELM}^{conv} and ΔW_{ELM}^{cond} , respectively, normalised to the pedestal energy content W_{ped} , computed with $\alpha = 5 \times 10^{-4}$. It illustrates the decline of ΔW_{ELM} with increasing ν^* as observed in experiments [41]. Also in agreement with recent experimental observations [67] the share to the energy loss is dominated by ion convection ΔW_{ELM}^{conv} rather than by conductive heat loss ΔW_{ELM}^{cond} in a broad range of ν^* (an effect reversing only minutely for $\nu^* > 1$). The conductive heat loss is significantly curtailed compared to that found in Ref.[63] because the heat flux limit was reduced from 0.2 to 0.03 according to recent findings [68] (previous chapter). The decline of $\Delta W_{ELM}/W_{ped}$ with increasing ν^* is due to collisions of hot ions with thermal ones: (i) the friction force reduces V and less ions have enough time to escape the plasma during the ELM burst and (ii) ion kinetic energy is dissipated more strongly in the background plasma.

Figure 5.4 illustrates the radial profile of the density of kinetic energy loss, $w_{ELM}^{conv} = |dW_{ELM}^{conv}/dr|$, normalised to the pedestal energy content. This value has its maximum at the ETB top in agreement with observations on the post ELM temperature drop [41]. The region where the losses are localised becomes narrower with increasing collisionality as it is also observed experimentally [41]. On the one hand, steep gradients of density and temperature imply a powerful electric force in the ETB driving ions out of the plasma compared with such a force deeper inside the plasma where the parameter profiles are relatively flat. Therefore, particles from deeper plasma region need much more time to reach the separatrix and the convective loss contribution declines fast for $r < a - \Delta_b$. On the other hand, near the separatrix in the ETB the initial energy and number of ejected particles decrease since T and n drop, and the same happens with the loss contribution.

The MHD perturbation level characterised by the inclination angle α can be only roughly estimated from the model of Ref.[63]. Therefore α has been varied in order to examine the sensitivity of the results to it. Figure 5.5 shows the variation with α in the collisionality dependence of the relative ELM energy loss $\Delta W_{ELM}/W_{ped}$. It grows slightly stronger than linearly with increasing α , however exhibiting a similar decline with increasing ν^* . Increasing α means a stronger bend of the field lines in the radial direction, and implies a two fold cause for the increase in the radial transport of ions. First, a higher fraction of the radial pressure gradient in the parallel direction provides a higher parallel electric field driving ions along field lines and increasing their energy. Second, the transport along field line determines the radial motion and time needed for a particle to escape the plasma. As a consequence, the ion convection loss from both ETB region and deeper plasma regions, is enhanced with increasing α . Figure 5.5 shows the collisionality dependence of the average energy per escaping ion measured in the ion thermal energy at the barrier top, $E_{av}/(1.5T_b)$, for different values of the field line inclination angle α . For all conditions this characteristic appears to lie within a relatively narrow range $0.8 < E_{av}/(1.5T_b) < 1.6$. For the chosen parameters, this ratio surging and sinking with increase in α and ν^* respectively, implying a greater fraction of suprathermal particles escaping for higher α and lower ν^* . As explained before with increasing ν^* , ions deeper inside the plasma have lower escape

probability, and apparently these ions have higher average energy in contrast to those present in the proximity of the separatrix, owing to the radial temperature profile. Also, an increase in α suggests, as mentioned above, substantial ion convection from deeper plasma regions, where ions are of higher average energy.

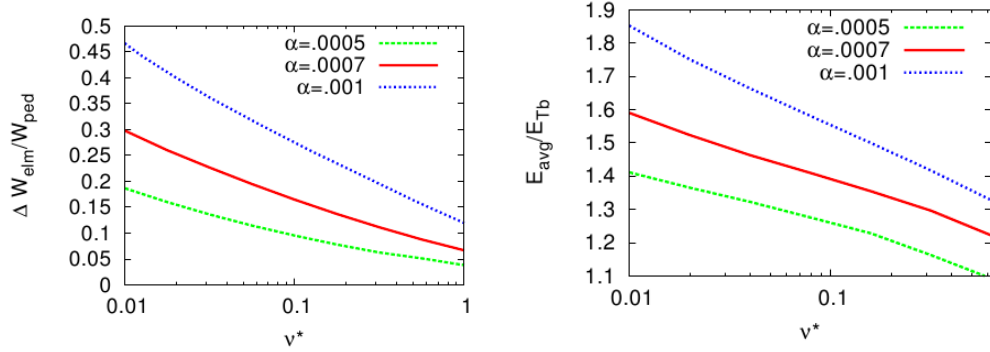


Figure 5.5: (Left) Energy loss $\Delta W_{ELM}/W_{ped}$ for different levels of perturbation α - $\Delta W_{ELM}/W_{ped}$ increases with α . (Right) Average energy $E_{av}/(1.5T_b)$ of ions released during ELMs also increases with α and decreases with ν^*

Conclusion - Important experimental findings on energy loss during type I ELM bursts have been reproduced in present calculations: (i) the ELM energy loss decreases with increasing collisionality ν^* ; (ii) ion convection appears as dominant mechanism for energy loss, (iii) the maximum in contribution to the loss from different radial positions is localised at the ETB top as it is observed for the temperature change after an ELM, (iv) the width of the edge plasma region involved in the ELM energy loss exceeds the ETB barrier by a factor of 2-4 and decreases with increasing ν^* . The results are sensitive enough to the level of the magnetic field perturbation caused by the ballooning-peeling MHD instability and characterised by the inclination angle α . Therefore precise determination of α is very essential for firm ELM loss predictions.

5.4 Model of the time variation of the field line inclination

In the above investigation the field line perturbation α_{elm} has been taken constant in space and time, and the n, T profiles are assumed constant during the ELM duration τ_{ELM} . In this section we go a step further considering time evolution of α_{elm} and n profile. A simple way to write the time evolution of α_{elm} , is to consider growth due to the concerned instabilities, the decay due to various dissipation mechanisms as approximated to be linear in time, activating when there is net outward particle flux in the ETB:

$$\frac{d\alpha}{dt} = \alpha \left[\gamma - \frac{\Theta(-\eta)}{t_{ELM}} \right] \quad (5.9)$$

where $\eta = \frac{\delta n_b}{n_b}$ and δn_b is the excess of n_b over this value at instability threshold, n_b is a function of collisionality. In this model instability growth rate for ballooning modes is considered responsible for the growth in time of the field line inclination angle:

$$\gamma \approx \frac{1}{Rq} \sqrt{\frac{B^2 \alpha_{cr}}{4\pi m_i n_b} \frac{\delta n_b}{n_b}} \quad (5.10)$$

The change in pedestal density characterises the variation of the pedestal pressure gradient, the driving force for ballooning modes. The growth rate can be written in a different form with new variables:

$$\gamma \approx \frac{V_A}{Rq} \sqrt{\eta \Theta(\eta)} \quad V_A = \sqrt{\frac{B^2 \alpha_{cr}}{4\pi m_i n_b}}, \tau = \frac{V_A}{Rq} t \quad (5.11)$$

with Heaviside function $\Theta(\eta < 0) = 0, \Theta(\eta \geq 0) = 1$. A model for assessment of γ is given in Appendix C.

Since γ depends on the density at the barrier top it is necessary to estimate its evolution in time. Particle balance in the barrier can be written as:

$$\frac{\Delta_b}{2} \frac{d\delta n_b}{dt} = \Gamma_i - \frac{(c_s \alpha)^2 n_b}{c_s \alpha \sqrt{\frac{n_b}{n_s}} + \frac{\gamma \Delta_b}{2}} \quad (5.12)$$

where the term on the left hand side represents the time evolution of the density at the barrier top. On the right hand side Γ_i is the fraction of the neutral influx ionised in the barrier and represents the source of particles. The second term has been taken from [63], where the expression has been derived from consideration of momentum balance along field lines, and represents the outward flux of particles during the ELM event. A more refined expression for this particle loss, including also perpendicular drift, is given in Appendix C. In dimensionless variables

$$\frac{d\eta}{d\tau} = \frac{2qRc_s}{\Delta_b V_A} \frac{\Gamma_i}{n_b c_s} - \left(\frac{2qRc_s}{\Delta_b V_A} \right)^2 \frac{\alpha^2}{\sqrt{\frac{n_b}{n_s} \frac{2Rq c_s}{\Delta_b V_A} \alpha} + \sqrt{\eta \Theta(\eta)}} \quad (5.13)$$

$$\frac{d\eta}{d\tau} = \xi \left[\sigma - \frac{\xi \alpha^2}{\delta \xi \alpha + \sqrt{\eta \Theta(\eta)}} \right] \quad (5.14)$$

with

$$\begin{aligned} \xi &= \frac{2qRc_s}{\Delta_b V_A} = \frac{2qR}{\Delta_b} \sqrt{\frac{8\pi n_b T_b}{B^2 \alpha_{cr}}} = \frac{2qR}{\Delta_b} \sqrt{\frac{\beta_b}{\alpha_{cr}}}, \beta_b = \frac{2n_b T_b}{B^2 / 4\pi} \\ \sigma &= \frac{\Gamma_i}{n_b c_s}, \delta = \sqrt{\frac{n_b}{n_s}}, c_s = \sqrt{\frac{2T_b}{m_i}} \end{aligned}$$

Density exceeds the ballooning threshold and MHD mode develops if

$$0 < \frac{d\eta}{d\tau}(0) \implies \alpha(0) < \sigma\delta$$

Time variation of the inclination angle with $\tau_{ELM} = V_A t_{ELM}/Rq$ can be written as:

$$\frac{d\alpha}{d\tau} = \alpha \left[\sqrt{\eta\Theta(\eta)} - \frac{\Theta(-\eta)}{\tau_{ELM}} \right] \quad (5.15)$$

but

$$\frac{d\alpha}{d\tau} = 0$$

if α drops down to $\alpha(0)$

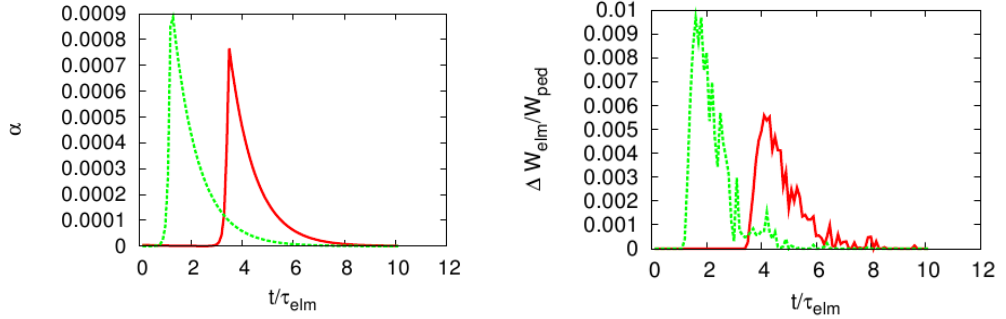


Figure 5.6: Time variation of α (left) and $\Delta W_{ELM}/W_{ped}$ (right) for $\alpha_0 = 5 \times 10^{-8}$ (dashed lines) and $\alpha_0 = 5 \times 10^{-6}$ (solid lines). α grows faster for smaller α_0 and appears to have a higher magnitude during the ELM. The energy loss $\Delta W_{ELM}/W_{ped}$, follows similar time evolution as α , energy loss is higher for smaller α_0

Equations 5.15 and 5.14 are integrated numerically for a characteristic time $10 \times \tau_{elm}$. Such a characteristic time greater than the ELM time is chosen so as to get insight in a ELM cycle with its growing, decaying and quiescent phase and to estimate the resulting transport.

In contrast to the previous section where α was considered constant in time, we see that some new physics can be distinguished with this model. Figure 5.6 shows the time evolution of α vs t/τ_{elm} . We see that for smaller value of α_0 , that is its value before the onset of an ELM, the perturbation grows quicker and has higher peak than in the case for higher α_0 . This can be explained looking at the coupling between equations 5.15 and 5.14. In the case where α_0 has lower value, the particle influx greatly exceeds the particle outflux which is proportional to α , and thus the density at the edge increases very rapidly. The rate of change of α in time is proportional to density and as a result also grows quickly. Although in this case α does reach a level whereon it increases the particle outflux and hence relaxes the density, it already achieves

a much higher peak than the case beginning with higher α_0 . Its average over time is also greater as can be seen more explicitly from fig. 5.7, which shows the variation of α_{avg} for cases beginning with different α_0 . Fig. 5.7 shows the collisionality dependence of energy loss during ELMs for cases beginning with different α_0 . As expected from the behaviour of α_{avg} with ν^* , the energy loss is also higher for lower α_0 .

The interesting result obtained above can actually explain certain important physics of the ELM phenomenology. First of all, the effective time during which most of the losses during ELMs takes place, would correspond to the time where α lies above a certain threshold level and as seen from figure 5.6 this corresponds roughly to τ_{elm} . Secondly, α_0 at the onset of ELM, determines to a great extent the α_{avg} and $\Delta W_{elm}/W_{ped}$, which appear to be higher for lower α_0 . This can explain the mitigation of ELMs by resonant magnetic field perturbations where the magnetic field lines are perturbed by means of an external source to a level above their normal values. The increased intermittent transport due to higher α_0 hinders the growth of α and consequently α_{avg} and $\Delta W_{elm}/W_{ped}$ are reduced.

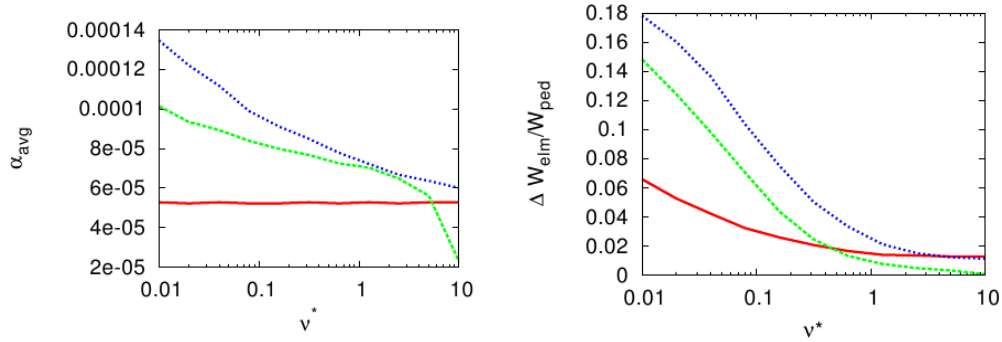


Figure 5.7: Variation of α_{avg} (left) and $\Delta W_{ELM}/W_{ped}$ (right) with ν^* , for different values of α_0 , $\alpha_0 = 5 \times 10^{-8}$ (dotted lines), $\alpha_0 = 5 \times 10^{-6}$ (dashed lines) and $\alpha_0 = 5 \times 10^{-4}$ (solid lines). Both α_{avg} and $\Delta W_{ELM}/W_{ped}$ decrease with ν^* , and with increasing α_0

5.5 0-D model for time evolution of all ETB parameters during elms

In this section we propose a model for time evolution of both n and T profiles during an ELM. This model is yet to be tested and provides scope for continuation of this work.

Particle balance equation, which can give us the time evolution of density at the barrier top, can be written as:

$$\frac{\partial n}{\partial t} + \nabla_{\perp} \Gamma_{\perp} + \nabla_{\parallel} \Gamma_{\parallel} = k_i n n_0 \quad (5.16)$$

where moving left to right the various terms represent the time evolution of density at a given point in space, the gradient of the particle flux perpendicular to field lines, gradient of particle flux along field lines and particle source due to ionisation of neutral influx, n_0 is neutral density and k_i is the ionisation rate. Particles are lost due to both perpendicular and parallel transport mechanisms.

Parallel momentum equation, can give us the time evolution of parallel particle flux at the separatrix, and can be written as:

$$\frac{\partial \Gamma_{\parallel}}{\partial t} + \nabla_{\parallel} \left(\frac{\Gamma_{\parallel}^2}{n} + \frac{2T}{m_i} n \right) = 0 \quad (5.17)$$

where the first two terms represent the convective derivative of the parallel momentum and the last term is the pressure gradient along field lines. The pressure gradient drives particle along field lines and the inclination of the field lines in the radial direction results in the parallel particle flux.

Heat balance equation, can give us the time evolution of temperature at the barrier top, and can be written as:

$$\frac{\partial}{\partial t} (3nT) + \nabla_{\perp} q_{\perp} + \nabla_{\parallel} q_{\parallel} = -k_i n n_0 E_i \quad (5.18)$$

where moving left to right the various terms represent time evolution of the energy density, perpendicular gradient of the heat flux, the parallel gradient of the heat flux and energy spent in the ionisation of neutrals. E_i is energy lost by ionisation of a neutral. The perpendicular particle flux and the perpendicular heat flux can be written as

$$\Gamma_{\perp} = -D_{\perp} \nabla_{\perp} n \quad q_{\perp} = 3\Gamma_{\perp} T - \kappa_{\perp} \nabla_{\perp} T$$

$D_{\perp}, \kappa_{\perp}$ are transport coefficients between ELMs, presumably neoclassical ones. The perpendicular particle flux has been considered to be mainly a consequence of diffusion, and the perpendicular heat flux has both a conductive component and convection of thermal particles. The parallel heat flux q_{\parallel} has been estimated in the previous sections, and has contributions from conduction due to electrons and convection of ions.

Presuming that the plasma parameters are uniform over unperturbed magnetic surfaces, which should be valid close to equilibrium condition, and averaging equation 5.16, 5.17 and 5.18 over unperturbed magnetic surfaces, that is in the ϑ, φ plane, one obtains 1-D transport equations:

$$\begin{aligned} \frac{\partial n}{\partial t} + \frac{\partial}{\partial r} \left(-D_{\perp} \frac{\partial n}{\partial r} \right) + \frac{\partial \alpha \Gamma_{\parallel}}{\partial r} &= k_i n n_0 \\ \frac{\partial}{\partial t} \Gamma_{\parallel} + \alpha \frac{\partial}{\partial r} \left(\frac{\Gamma_{\parallel}^2}{n} + \frac{2T}{m_i} n \right) &= 0 \\ \frac{\partial}{\partial t} (3nT) + \frac{\partial}{\partial r} \left[-3D_{\perp} \frac{\partial n}{\partial r} T - \kappa_{\perp} \frac{\partial T}{\partial r} + q_{\parallel} \right] &= -k_i n n_0 E_i \end{aligned} \quad (5.19)$$

These equations are integrated over the width of the edge region, barrier ($a - \Delta_b \leq r \leq a$) and deeper region involved in the ELM ($a - \Delta_b - \Delta_e \leq r \leq a - \Delta_b$) with the assumed piecewise shape of radial profiles.

$$\begin{aligned}\eta(\varsigma) &= \eta_s + (1 - \eta_s) \min(1, \varsigma) + (\eta_e - 1) \max(0, \varsigma - 1) \frac{\Delta_b}{\Delta_e}; \eta_{s,e} = \frac{n_{s,e}}{n_b} \\ \theta(\varsigma) &= \theta_s + (1 - \theta_s) \min(1, \varsigma) + (\theta_e - 1) \max(0, \varsigma - 1) \frac{\Delta_b}{\Delta_e}; \theta_{s,e} = \frac{T_{s,e}}{T_b} \\ x &= a - r; \varsigma = x/\Delta_b; S_{sep} = 4\pi^2 \kappa a R\end{aligned}$$

In these profiles the subscripts s, b, e indicate respectively the separatrix, barrier top and the inner boundary of the plasma region contributing to the particle and energy loss. The values at separatrix are assumed to be constant and the value at the barrier is allowed to vary in time. Hence integrating the equations 5.19 over the edge transport barrier with the boundary conditions at $r = a - \Delta_b - \Delta_e$:

$$\begin{aligned}\frac{\partial n}{\partial r} &= 0 \\ -3D_{\perp} \frac{\partial n}{\partial r} T - \kappa_{\perp} \frac{\partial T}{\partial r} &= q_{core}\end{aligned}$$

one gets 0-D equations for the density and temperature at the barrier top ($r = a - \Delta_b$), $n_b(t)$ and $T_b(t)$, and the parallel particle flux at the separatrix ($r = a$), $\Gamma_{\parallel}^s(t)$;

$$\begin{aligned}\frac{\Delta_b + \Delta_e}{2} \frac{dn_b}{dt} &= j_0 - D_{\perp} \frac{n_b - n_s}{\Delta_b} - \alpha \Gamma_{\parallel}^s \\ \frac{\Delta_b}{2} \frac{d}{dt} \Gamma_{\parallel}^s &= \alpha \left[2 \frac{T_e n_e - T_s n_s}{m_i} - \frac{(\Gamma_{\parallel}^s)^2}{n_s} \right] \\ &= \left[\frac{\Delta_b n_s + \Delta_e n_e}{2} + (\Delta_b + \Delta_e) n_b \right] \frac{dT_b}{dt} + \\ &+ \left[\frac{\Delta_b T_s + \Delta_e T_e}{2} + (\Delta_b + \Delta_e) T_b \right] \frac{dn_b}{dt} \\ &= q_{core} - j_0 E_i - 3D_{\perp} \frac{n_b - n_s}{\Delta_b} T_s - \kappa_{\perp} \frac{T_b - T_s}{\Delta_b} - q_r^s\end{aligned} \tag{5.20}$$

where j_0 is the influx of neutrals through separatrix, q_r^s the energy out-flow due to magnetic field perturbations has been found out in the previous sections. The plasma parameters at the separatrix, T_s and n_s , are assumed given but later should be defined from a model for SOL. The discretized form of the equations 5.20, are given in the Appendix C, they have to be solved numerically.

In this chapter models to study transport of heat and particles due to ELMs have been developed. At first energy losses during ELMs have been estimated considering contribution from parallel conductive loss due to electrons and parallel convection of ions, with constant level of the magnetic field perturbation and steady profiles for density n and temperature T , and accounting for the heat flux limit. The estimate shows agreement with experimental observations. As a next step the model is developed further by accounting for the time evolution of α_{elm} due to ballooning mode and linear dissipation, and a simple consideration of particle balance in the ETB with a constant particle source due to ionisation of neutrals and loss of particles due to the perturbation.

Furthermore, modification of the model for heat and particle loss during ELMs is proposed. Namely a model for time evolution of n and T in addition to α_{elm} has been developed. The particle balance, parallel momentum and energy equation have been integrated in the region contributing to the heat and particle loss during ELMs (as estimated from the model for ion convection heat loss); and equations for time evolution of n_b and T_b are obtained. The time evolving profiles when coupled with the above discussed model for heat and particle loss, yield a 0-D model for ELMs. In addition a more sophisticated model for particle loss due to ballooning modes is proposed and presented in the Appendix C. In this model the ballooning growth rate has been determined with a eigen value consideration. The particle fluxes due to perpendicular drift motion and radial contribution of parallel particle flux have been estimated. These models still need to be tested and provide scope for future work.

Chapter 6

Summary

With the growing demand for energy, thermonuclear fusion has potential to offer an economically, environmentally and socially acceptable supply of energy. A feasible method to execute thermonuclear fusion is to make a magnetically confined Maxwellian-plasma, where the high energy particles at the tail of the distribution undergo fusion. A lot of experience has been gained in toroidal magnetic confinement devices tokamaks, and it appears to be a promising design for the future efforts in fusion reactor development (ITER, DEMO). The tokamak still faces challenges in the major areas which can be categorised into confinement, heating and fusion technology. Confinement has to do with satisfying the Lawson criteria, and amongst various transport mechanisms that degrade confinement is transport along magnetic field lines perturbed by diverse MHD instabilities.

Unstable modes such as ideal ballooning-peeling, tearing etc., break closed magnetic surfaces and destroy the axisymmetry of the magnetic configuration in a tokamak, and provide deviation of magnetic field lines from unperturbed magnetic surfaces. Radial gradients of plasma parameters have nonzero projections along such lines and drive parallel particle and heat flows which contribute to the radial transport. Such transport can significantly affect confinement as this takes place by the development of neoclassical tearing modes (NTMs) in the core and edge localised modes (ELMs) at the plasma periphery. Therefore the transport characteristics parallel to the magnetic field are very important for understanding and quantitative description of such phenomena. Parallel transport is also relevant for mechanisms of ELM mitigation with external magnetic field perturbations.

In chapter 2 a theoretical basis for the description of plasma, instabilities and transport is given which assists in understanding the following chapters.

Magnetic islands are well known phenomena in hot fusion plasmas generated by resonant perturbations of the magnetic field. The latter arise from different sources such as spontaneously developing MHD instabilities, or special coils introduced in order to control the plasma behaviour. In chapter 3 transport of heat originating from core plasma and passing through non-overlapped magnetic island chains is investigated using the 'Optimal path' approach, which is based on the principle of minimum entropy production.

A more detailed analytical approach by R. Fitzpatrick [28] is also presented, where the limit cases of "small", $w \ll w_c$ ($\zeta = 4\kappa_{\parallel} b_r^2 / \kappa_{\perp} \ll 1$), and "large", $w \gg w_c$ ($\zeta \gg 1$), islands have been considered analytically. On the one hand, compared to previous analytical studies [17, 28] the present approach treats on the same foot cases with arbitrary parameter. On the other hand, it illustrates in a more transparent way than a pure numerical approach [60, 62] what parameters are of concern for the effective transport characteristics, and provides a computationally economical method to find the dependencies on these parameters. This model shows that the effective heat conduction κ_{eff} through islands increases with κ_{\parallel} and with the perturbation level, characterised by σ_{ch} , and reaches a saturation level with κ_{\parallel} , which corresponds to the case where the temperature change in the island disappears. Also with increasing σ_{ch} and κ_{\parallel} , heat is carried predominantly close to the separatrix.

In chapter 4 transport of heat through internally heated magnetic islands is investigated by further development of the 'Optimal path' method. In addition the approach by R. Fitzpatrick, has been extended by including in the heat transport equation an additional boundary condition for heating in a thin layer at the resonant magnetic surface. Heat flux limit, limiting parallel heat conduction in low collisional plasmas is elucidated with the 'Optimal path' method, and validated by the extension of the R. Fitzpatrick's model, by application of these approaches to experimental observations made at TEXTOR tokamak [65], where islands were heated at the resonant surface with ECRH, and detailed temperature profiles were measured with ECEI diagnostic. The elucidated value of the heat flux limit lies in the range $\xi = 0.02 - 0.045$, and is in good agreement with that found in laser fusion experiments [10].

In chapter 5 models to study transport of heat and particles due to ELMs have been developed. At first energy losses during ELMs have been estimated considering contribution from parallel conductive loss due to electrons and parallel convection of ions, with constant level of the magnetic field perturbation and steady profiles for density n and temperature T , and accounting for the heat flux limit. The estimate shows decrease of energy loss during ELMs with increasing collisionality ν^* and major contribution to energy loss from ion convection, as has been observed in experiments. The energy loss increases with the level of the inclination angle α_{elm} of perturbed field lines. As a next step the model is developed further by accounting for the time evolution of α_{elm} due to ballooning mode and linear dissipation, and a simple consideration of particle balance in the ETB with a constant particle source due to ionisation of neutrals and loss of particles due to the perturbation. α_{elm} depends on its value at the onset of ELM α_0 , and peaks to higher values for lower α_0 . The energy loss during the ELM shows similar dependence on α_0 , and this has been interpreted as follows: higher perturbations and transport in the inter-ELM period slow down the build of pressure gradient at the ETB, and hence also the growth of the perturbation.

Furthermore, modification of the model for heat and particle loss during ELMs is proposed. Namely a model for time evolution of n and T in addition to α_{elm} has been developed. The particle balance, parallel momentum and

energy equation have been integrated in the region contributing to the heat and particle loss during ELMs (as estimated from the model for ion convection heat loss); for this piecewise linear profiles for n and T varying in time with their value at the barrier top are assumed, and equations for time evolution of n_b and T_b are obtained. The time evolving profiles when coupled with the above discussed model for heat and particle loss, yield a 0-D model for ELMs. In addition a more sophisticated model for particle loss due to ballooning modes is proposed and presented in the Appendix C. In this model the ballooning growth rate has been determined with a eigen value consideration. The particle fluxes due to perpendicular drift motion and radial contribution of parallel particle flux have been estimated. These models still need to be tested and provide scope for future work.

Heat and particle losses, are of primary importance by strong magnetic field perturbations, due to radial contribution of the parallel heat and particle fluxes. Both NTMs and ELMs are omnipresent phenomenon in the operation regimes proposed for future fusion experiments and reactor prototypes, and such transport is bound to affect the confinement and other operation parameters in these devices. The impact of such transport on the operation parameters needs careful consideration, and understanding the physics behind can help to control these phenomena.

Bibliography

- [1] Bernstein I B *et al.*, 1958 Proc. Roy. Soc. (London), **A 244**, 17
- [2] Klimontovich Y L, *The kinetic theory of electromagnetic processes*, 1958 Sov. Phys. JETP, **6** 753
- [3] Shafranov V D, 1960 Sov. Phys. JETP, **26** 682
- [4] I. Prigogine, *Introduction to Thermodynamics of Irreversible Processes*, 2nd Edition (Interscience Publishers Inc., New York, 1961) p.53.
- [5] Trubnikov B A 1965 in *Reviews of Plasma Physics*, New York, Consultants Bureau Vol.1 105
- [6] Braginskii S. I. in *Reviews of Plasma Physics*, New York, Consultants Bureau Vol.1, 205 (1965).
- [7] Greene J M *et al.*, 1968 Plasma Physics, **10** 729
- [8] Furth H P *et al.*, 1973 Phys. of Fluids **16**, 1054
- [9] Rutherford P H *et al.*, 1973 Phys. of Fluids **16**, 1903
- [10] R C Malone *et al.*, 1975 Phys. Rev. Lett. **34**, 721
- [11] Lortz D 1975 Nuclear Fusion, **15** 49
- [12] Connor J W *et al.*, 1978 Physics Review Letters **40** 753
- [13] Wagner F *et al.*, 1982 Phys. Rev. Lett **49**, 1408
- [14] Luciani J F *et al.*, 1983 Phys. Rev. Lett. **51**, 1664
- [15] Kaye S M *et al.*, 1984 Journal of Nuclear Materials **121**, 115
- [16] Keilhacker M *et al.*, 1984 Plasma Phys. Control. Fusion **26**, 49
- [17] Tokar M Z, Proceedings of 14th European Conference on Controlled Fusion and Plasma Physics, Madrid, 1987 (European Physical Society, Geneva, 1987) **13F/2**, 687
- [18] Freidberg J P, *Ideal Magnetohydrodynamics*, Plenum Press, New York, 1987

-
- [19] Hahm T S, 1988 Phys. Fluids **31**, 3709
- [20] McCool S C *et al.*, 1990 Nucl. Fusion **30**, 167
- [21] Chodura R, 1992 Contrib. Plasma Phys. **32**, 219
- [22] Epperlein E M *et al.*, 1992 Phys. Fluids B **4**, 2211
- [23] Smolyakov A I *et al.*, 1993 Plasma Phys. Control. Fusion **35**, 657
- [24] Groebner R J, 1993 Phys. Fluids B **5**, 2343
- [25] Tokar M Z, 1994 Plasma Phys. Control. Fusion **36**, 1819
- [26] Chang Z *et al.*, 1995 Phys. Rev. Lett **74**, 4663
- [27] Tamai H *et al.*, 1995 J. Nucl. Mater. **220–222**, 365
- [28] Fitzpatrick R, 1995 Phys. Plasmas **2**, 825
- [29] Ghendrih Ph *et al.*, 1996 Plasma Phys. Control. Fusion **38**, 1653
- [30] Zohm H, 1996 Plasma Phys. Control. Fusion **38**, 105
- [31] Connor J W, 1998 Plasma Phys. Control Fusion **40** 191
- [32] Connor J W *et al* 1998 Phys. Plasmas **5** 2687
- [33] Tokar M Z, 1999 Phys. Plasmas **6**, 2808
- [34] Osborne T H *et al.*, 2000 *Plasma Phys. Contr. Fusion* **42** A175
- [35] Hugill J, 2000 *Plasma Phys. Contr. Fusion* **42** R75
- [36] Connor J W, 2000 *Plasma Phys. Contr. Fusion* **42** R1
- [37] Nishikawa K, Wakatani M, *Plasma Physics, third Edition* (Springer, 2000)
- [38] Meskat J P, PhD thesis *Institute for Plasma Research, Stuttgart University* (2001)
- [39] Snyder P B *et al.*, 2002 *Phys. Plasmas* **9** 2037
- [40] Wilson H R *et al.*, 2002 Phys. of Plasmas **9** 1277
- [41] Loarte A *et al.*, 2003 Plasma Phys. Control. Fusion **45** 1549
- [42] Degelink A W *et al.*, 2003 Plasma Phys. Control. Fusion **45** 1637
- [43] Urano H *et al.*, 2003 Plasma Phys. Control. Fusion **45** 1571
- [44] Evans T E *et al.*, 2004 Phys. Rev. Lett. **92** 235003
- [45] Wesson J, *Tokamaks, third Edition* (Clarendon Press, Oxford, 2004)
- [46] Yu Q *et al.*, 2004 Phys. of Plasmas **11** 140

-
- [47] Lönnroth J S *et al.*, 2004 Plasma Phys. Control. Fusion **46** 1197
- [48] Wolf R C *et al.*, 2005 Nucl. Fusion **45**, 1700
- [49] Westerhof E *et al.*, 2005 Fusion Science Tech. **47**, 108
- [50] Snyder P B *et al.*, 2005 *Phys. Plasmas* **12** 056115
- [51] Wade M R *et al.*, 2005 Phys. Rev. Lett **94**, 225001
- [52] Boedo J A *et al.*, 2005 *Phys. Plasmas* **12** 072516
- [53] Saarlema S, PhD Thesis *Labortory of Advanced Energy Systems, Helsinki University of Technology, Finland* (2005)
- [54] Onjun T *et al.*, 2005 Phys. Plasmas **12** 012506
- [55] Moyer R *et al.*, 2005 Phys. Plasmas **12** 056119
- [56] Finken K *et al.*, 2005 Phys. Rev. Lett **94**, 015003
- [57] Evans T E *et al.*, 2006 *Nature Physics* **2** 419
- [58] Loozen X, PhD thesis *Institute for Plasma Physics, FZ Jülich Germany* (2006)
- [59] Wilson H R *et al.*, 2006 Plasma Phys. Control. Fusion **48**, A71
- [60] Yu Q, 2006 Phys. of Plasmas **13**, 062310
- [61] Liang Y *et al.*, 2007 Phys. Rev. Lett **98**, 265004
- [62] Hölzl M *et al.*, 2007 Phys. Plasmas **14**, 052501
- [63] Tokar M Z *et al.*, 2007 Plasma Phys. Control. Fusion **49**, 395
- [64] Tokar M Z *et al.*, 2007 Phys. Rev. Lett **98**, 095001
- [65] Classen I G J *et al.*, 2007 Phys. Rev. Lett **98**, 035001
- [66] Doyle E J *et al* 2007 Nuclear Fusion **47** S18
- [67] Kamiya K *et al* 2007 Plasma Phys. Control. Fusion **49** S43
- [68] Tokar M Z and Gupta A, 2007 *Phys. Rev. Lett.* **99** 225001
- [69] Saibene G *et al* 2007 Nuclear Fusion **47** 969
- [70] Snyder P B *et al.*, 2007 Nucl. Fusion **47** 961
- [71] Pankin A Y *et al.*, 2007 Plasma Phys. Control. Fusion **49** S63
- [72] Park G *et al.*, 2007 Journal of Physics **78**, 012087
- [73] Hayashi N *et al.*, 2007 Nucl. Fusion **47** 682

- [74] Nardon E *et al.*, 2007 Phys. Plasmas **14**, 092501
- [75] Hölzl M *et al.*, 2008 Phys. of Plasmas **15**, 072514
- [76] Chang C S *et al.*, 2008 Journal of Physics **125**, 012042
- [77] Wiesen S *et al.*, 2008 Contrib. Plasma Phys. **48**, 201

Acknowledgements

I would like to thank my supervisor at FZ Jülich Prof. Mikhail Tokar for providing valuable assistance at various stages of this work. I am grateful to several friendly colleagues who gave me support in various aspects of my research as well as my personal life, especially Dominik Schega, Dr. Xavier Loozen, Dr. Vladislav Kotov, Dr. Jöel Rosato, Albert Greiche, Christopher Wiegmann, Dr. Oleksander Marchuk, Dr. Denis Kalupin and Rui Ding.

I would like to express my gratitude towards Prof. Detlev Reiter for his support, and also Mrs Hoffmann and Mrs Schumacher, to make my stay at FZ Jülich comfortable. I would like to thank Dr. Dirk Reiser for his availability, and Dipl.Ing. Petra Börner and Oliver Schmidt for the numerous occasions they provided me with technical support. I would also like to thank Prof. Carati, Ms De Neyn and Ms Deprins for helping me with the administrative issues at ULB.

I appreciate Prof. Maurizio Lontano for inviting me to IFP, Milano, and also Dr Sven Wiesen who helped me learn various useful analysing tools available at JET. I am thankful to Prof. Raghvendra Singh who provided useful ideas for my thesis project, and also hosted my visit at IPR, Gandhinagar. I am very grateful to Prof. Jan Weiland with whom I did my Msc thesis, and who gave me the opportunity to step into the world of Plasma Physics.

Most of all I am grateful to my family who allowed me to stay far from them for all these years and gave me lot of support. Finally I would like to thank all the people who helped with so many different things and whose list is too long to mention here.

This study has been partly performed within GRK1203 of German Research Society.

Appendix A

Magnetic islands

A.1 Transport across non overlapped magnetic islands

The entropy production rate in a toroidal shell of thickness $r_2 - r_1 \ll r_s$, with a surface area S , and heat flux q_r through it is given by:

$$\int \theta dV = \int \mathbf{q} \cdot \nabla(1/T) dV = \int_{r_1}^{r_2} q_r \frac{\partial}{\partial r} (1/T) S dr = q_r S \left[\frac{1}{T} \right]_{r_1}^{r_2} = \frac{P \Delta T}{T_1 T_2}$$

Hence we see that the ΔT should be minimised in order to have minimum entropy production. The temperature gradient along a field line i.e. in direction of l , with a radial perturbation of the form $b_r \sin \zeta$, can be expressed as:

$$\frac{dT}{dl} = \frac{dT}{dr} \frac{dr}{dl} \approx \frac{\partial T}{\partial r} b_r \sin \zeta$$

Thus the radial heat flux q_r , due to transport along field lines, is the product of this temperature gradient to parallel heat conductivity and the component of the field line along r -direction:

$$q_r \approx -(\kappa_{\parallel} \nabla_{\parallel} T) B_r / B = -\kappa_{\parallel} b_r^2 \sin^2 \zeta \partial T / \partial r$$

Putting $y = 2x/w$, and using $\xi = \delta/w$, $\cos \zeta = 2y^2 + \Omega$, we get $\sin^2 \zeta = 1 - (2y^2 - 2\xi^2 + 1)^2$. The parallel temperature gradient from the above equation can thus be written as:

$$\Delta_{\parallel} T = -\frac{q_r}{\kappa_{\parallel} b_r^2} \int_{r_b}^{r_t} \frac{dr}{\sin^2 \zeta} = -\frac{w q_r}{2 \kappa_{\parallel} b_r^2} \int_{y_b}^{y_t} \frac{dy}{1 - (1 + 2y^2 - 2\xi^2)^2}$$

$$\Delta_{\parallel} T = -\frac{w q_r}{8 \kappa_{\parallel} b_r^2} \int_{y_b}^{y_t} \left(\frac{1}{a_n^2 - y^2} + \frac{1}{a_p^2 + y^2} \right) dy$$

where $a_n = \xi$ and $a_p = (1 - \xi^2)^{1/2}$.

$$\Delta_{\parallel}T = -\frac{wq_r}{8\kappa_{\parallel}b_r^2} \int_{y_b}^{y_t} \left(\frac{1}{2a_n} \left[\frac{1}{a_n + y} + \frac{1}{a_n - y} \right] + \frac{1}{a_p^2 + y^2} \right) dy$$

Inside the island $\xi < 1 \Rightarrow a_n^2 > 0$ and $a_p^2 > 0$, and on integration the required expression is obtained:

$$\Delta_{\parallel}T = \frac{wq_r}{8\kappa_{\parallel}b_r^2} \left[\frac{1}{2a_n} \ln\left(\frac{1 + y/a_n}{1 - y/a_n}\right) + \frac{1}{a_p} \arctan(y/a_p) \right]_{y_t}^{y_b}$$

On the separatrix $\xi = 1 \Rightarrow a_p^2 = 0$. On integration one obtains:

$$\Delta_{\parallel}T = \frac{wq_r}{8\kappa_{\parallel}b_r^2} \left[\frac{1}{2a_n} \ln\left(\frac{1 + y/a_n}{1 - y/a_n}\right) - \frac{1}{u} \right]_{y_t}^{y_b}$$

Outside the island $\xi > 1 \Rightarrow a_p^2 < 0$. Here the integral cannot be performed as earlier since a_p assumes complex values. Let $a_{pn}^2 = -a_p^2$, then:

$$\Delta_{\parallel}T = -\frac{wq_r}{8\kappa_{\parallel}b_r^2} \int_{y_b}^{y_t} \left(\frac{1}{a_n^2 - y^2} - \frac{1}{a_{pn}^2 - y^2} \right) dy$$

$$\Delta_{\parallel}T = \frac{wq_r}{8\kappa_{\parallel}b_r^2} \left[\frac{1}{2a_n} \ln\left(\frac{1 + y/a_n}{1 - y/a_n}\right) - \frac{1}{2a_{pn}} \ln\left(\frac{1 + y/a_{pn}}{1 - y/a_{pn}}\right) \right]_{y_t}^{y_b}$$

In the above equations we let $a = a_n$ and $c = |a_p|, |a_{pn}|$, transform back to $x = wy/2$ to get the equations in the form used in our analysis. Since the same quantity of heat flows across the perpendicular, parallel and thus the combined path, we have the following relations:

$$q_r = -\kappa_{\perp} \frac{\Delta_{\perp}T}{\Delta_{\perp}r} = -\kappa_{\parallel eff} \frac{\Delta_{\parallel}T}{\Delta_{\parallel}r} = -\kappa_{eff} \frac{\Delta_{net}T}{\Delta_{net}r}$$

Solving for κ_{eff} one obtains,

$$\Rightarrow \kappa_{eff} = \frac{\Delta_{\perp}r + \Delta_{\parallel}r}{\frac{\Delta_{\perp}r}{\kappa_{\perp}} + \frac{\Delta_{\parallel}r}{\kappa_{\parallel eff}}}$$

Appendix B

Heat flux limit

B.1 Transport through heated magnetic islands

Close to the resonant surface ($q \simeq m/n$), the length along the phase coordinate is given by $z = r(\vartheta - \varphi/q) \simeq r_s \zeta/m$ and the distance from the resonant surface is $x = r - r_s$

The deviation of a field line from the resonant surface due to formation of islands is:

$$x = \frac{w}{2} \sqrt{\frac{\cos \zeta - \cos \zeta_s}{2}} \quad x_w = \frac{x}{w/2}$$

$$x_z \equiv \frac{dx}{dz} = -\frac{wm \sin \zeta}{8x_w r_s}$$

For a parallel path part $z_* \leq z \leq z_s$, the heat flux continuity equation is given as:

$$q_s dz_s = -\kappa_{||} b_r^2 \sin^2 \zeta \frac{\partial T}{\partial r} dt$$

where dz_s is the path width at the resonant surface $x = 0$, and dt is the path width at a given z . The unit vector along the normal to a point x, z on the path:

$$\vec{n} = \frac{-x_z \vec{e}_z + \vec{e}_x}{\sqrt{1 + x_z^2}}$$

Coordinates of a point at a distance dt from x, z on this normal is:

$$\tilde{z} = z - \frac{x_z dt}{\sqrt{1 + x_z^2}}, \tilde{x} = x + \frac{dt}{\sqrt{1 + x_z^2}}$$

The intersection of the normal with the second path border beginning at $z_s + dz_s$:

$$\begin{aligned}
\tilde{x} &= \frac{w}{2} \sqrt{\frac{\cos \tilde{\zeta} - \cos(\zeta_s + d\zeta_s)}{2}} \\
x + \frac{dt}{\sqrt{1+x_z^2}} &= \frac{w}{2\sqrt{2}} \sqrt{\cos \left[\frac{m}{r_s} \left(z - \frac{x_z dt}{\sqrt{1+x_z^2}} \right) \right] - \cos \left[\frac{m}{r_s} (z_s + dz_s) \right]} \\
x + \frac{dt}{\sqrt{1+x_z^2}} &\approx \frac{w}{2\sqrt{2}} \sqrt{\cos \zeta - \cos \zeta_s + \frac{m}{r_s} \frac{x_z dt}{\sqrt{1+x_z^2}} \sin \zeta + \frac{m}{r_s} \sin \zeta_s dz_s} \\
x^2 + \frac{2xdt}{\sqrt{1+x_z^2}} &\approx \frac{w^2}{8} \left[\cos \zeta - \cos \zeta_s + \frac{m}{r_s} \frac{x_z dt}{\sqrt{1+x_z^2}} \sin \zeta + \frac{m}{r_s} \sin \zeta_s dz_s \right] \\
dt &\approx \frac{\sin \zeta_s \sqrt{1+x_z^2}}{\frac{16r_s}{w^2 m} x - x_z \sin \zeta} dz_s \\
g = \frac{dt}{dz_r} &\approx \frac{\sin \zeta_s}{\sqrt{\sin^2 \zeta + (\sin \zeta / x_z)^2}}
\end{aligned}$$

Hence the heat flux can be written with the metric coefficient g as:

$$q_s = -\kappa_{||} b_r^2 \sin^2 \zeta \frac{\partial T}{\partial r} g$$

The temperature change along the parallel path part which corresponds to phase change $\zeta_s \rightarrow \zeta_*$, is given from the above equation for parallel heat flux as:

$$\begin{aligned}
\Delta_{||} T &= -\frac{q_s}{\kappa_{||} b_r^2} \int_{r_s}^{r_*} \frac{1}{g \sin^2 \zeta} dr = \int_{z_*}^{z_s} \frac{x_z}{g \sin^2 \zeta} dz \\
&= \frac{q_s r_s}{\kappa_{||} b_r^2 m} \int_{\zeta_*}^{\zeta_s} \frac{\sqrt{\sin^2 \zeta + (\sin \zeta / x_z)^2}}{\sin^2 \zeta \sin \zeta_s} x_z d\zeta \\
&= -\frac{q_s r_s}{\kappa_{||} b_r^2 m \sin \zeta_s} \int_{\zeta_*}^{\zeta_s} \frac{\sqrt{1+x_z^2}}{\sin \zeta} d\zeta \\
&= -\frac{q_s r_s}{\kappa_{||} b_r^2 m \sin \zeta_s} \int_{\zeta_*}^{\zeta_s} \frac{\sqrt{1 + \frac{(wm)^2}{r_s^2} \frac{\sin^2 \zeta}{\cos \zeta - \cos \zeta_s}}}{\sin \zeta} d\zeta
\end{aligned}$$

Region where $\frac{(wm)^2}{r_s^2} \frac{\sin^2 \zeta}{\cos \zeta - \cos \zeta_s}$ is of importance in $\sqrt{1 + \frac{(wm)^2}{r_s^2} \frac{\sin^2 \zeta}{\cos \zeta - \cos \zeta_s}}$:

$$\begin{aligned}
32 \left(\frac{r_s}{wm} \right)^2 &\leq \frac{\sin^2 \zeta}{\cos \zeta - \cos \zeta_s} \\
&\approx \frac{\sin^2 \zeta_s}{\cos \zeta_s + \sin \zeta_s \times (\zeta_s - \zeta) - \cos \zeta_s} \approx \frac{\sin \zeta_s}{\zeta_s - \zeta} \Rightarrow \\
\zeta_s - \zeta &\leq \frac{1}{32} \left(\frac{wm}{r_s} \right)^2 \approx 5 \times 10^{-3}
\end{aligned}$$

The contribution of this interval to the integral is roughly equal:

$$\begin{aligned}
\int_{\zeta_*}^{\zeta_s} \frac{\sqrt{\frac{\left(\frac{wm}{r_s}\right)^2 \sin^2 \zeta}{32 \cos \zeta - \cos \zeta_s}}}{\sin \zeta} d\zeta &\approx \frac{\frac{wm}{r_s}}{\sqrt{32 \sin \zeta_s}} \int_{\max\left[\zeta_s - \frac{1}{32} \left(\frac{wm}{r_s}\right)^2, \zeta_*\right]}^{\zeta_s} \frac{d\zeta}{\sqrt{\zeta_s - \zeta}} \\
&\approx \frac{2 \frac{wm}{r_s}}{\sqrt{32 \sin \zeta_s}} \min \sqrt{\zeta_s - \zeta_*, \frac{1}{32} \left(\frac{wm}{r_s}\right)^2} \\
&\approx \left(\frac{mw}{4r_s} \right)^2 \sqrt{\frac{\min \left[2 \left(\frac{4r_s}{mw}\right)^2 (\zeta_s - \zeta_*), 1 \right]}{\sin \zeta_s}}
\end{aligned}$$

and hence the parallel temperature change along the parallel path is given by:

$$\begin{aligned}
\Delta_{\parallel} T &\approx -\frac{q_s r_s}{\kappa_{\parallel} b_r^2 m \sin \zeta_s} \left(\int_{\zeta_*}^{\zeta_s} \frac{d\zeta}{\sin \zeta} + \left(\frac{mw}{4r_s} \right)^2 \sqrt{\frac{\min \left[2 \left(\frac{4r_s}{mw}\right)^2 (\zeta_s - \zeta_*), 1 \right]}{\sin \zeta_s}} \right) \\
&= -\frac{r_s q_s}{m \kappa_{\parallel} b_r^2} \frac{\ln \frac{\tan \frac{\zeta_s}{2}}{\tan \frac{\zeta_*}{2}} + \left(\frac{mw}{4r_s} \right)^2 \sqrt{\frac{\min \left[2 \left(\frac{4r_s}{mw}\right)^2 (\zeta_s - \zeta_*), 1 \right]}{\sin \zeta_s}}}{\sin \zeta_s}
\end{aligned}$$

For the reference cases below $\zeta_s = \frac{\pi}{2}$, $\zeta_* \approx 0.44$ (0.31) :

$$\ln \frac{\tan \frac{\zeta_s}{2}}{\tan \frac{\zeta_*}{2}} \approx 1.57 (1.85) \gg \left(\frac{mw}{4r_s} \right)^2 \sqrt{\frac{\min \left[2 \left(\frac{4r_s}{mw}\right)^2 (\zeta_s - \zeta_*), 1 \right]}{\sin \zeta_s}} \approx 0.01$$

i.e. the contribution from the second term in the expression for $\Delta_{\parallel} T$ can be normally neglected. The heat flux equation for the perpendicular path part beginning where the parallel path part ends, i.e. $z = z_*$ is given as:

$$q_s dz_s = -\kappa_{\perp} \frac{\partial T}{\partial r} dz_*$$

where dz_* is the distance between ends of the path borders starting at z_s and $z_s + dz_s$ and terminating at the same $x_* = x(z_s, z_*)$:

$$x_* = \frac{w}{2} \sqrt{\frac{\cos \zeta_* - \cos \zeta_s}{2}}$$

Since the path borders have the same x they satisfy the condition:

$$\begin{aligned} dx &= \frac{\partial x}{\partial z_*} dz_* + \frac{\partial x}{\partial z_s} dz_s = 0 \Rightarrow \\ dz_* &= \frac{\sin \zeta_s}{\sin \zeta_*} dz_s \end{aligned}$$

Thus the temperature change along the perpendicular path is obtained from the perpendicular heat flux equation as:

$$\begin{aligned} \Delta_{\perp} T &= -\frac{q_s \sin \zeta_*}{\kappa_{\perp} \sin \zeta_s} \left(\frac{w_*}{2} - x_* \right) \\ &= -\frac{wq_s \sin \zeta_*}{2\kappa_{\perp} \sin \zeta_s} \left(\frac{\cos \zeta_*}{2} - \sqrt{\frac{\cos \zeta_* - \cos \zeta_s}{2}} \right) \end{aligned}$$

Combining $\Delta_{\parallel} T$ and $\Delta_{\perp} T$, the total temperature change is obtained:

$$\begin{aligned} \Delta T &= \Delta_{\parallel} T + \Delta_{\perp} T \\ &= -\frac{r_s q_s}{m\kappa_{\parallel} b_r^2} \frac{\ln \left| \frac{\tan \frac{\zeta_s}{2}}{\tan \frac{\zeta_*}{2}} \right|}{\sin \zeta_s} - \frac{wq_s \sin \zeta_*}{2\kappa_{\perp} \sin \zeta_s} \left[\sqrt{\frac{1 + \cos \zeta_*}{2}} - \sqrt{\frac{\cos \zeta_* - \cos \zeta_s}{2}} \right] \\ &= -\frac{wq_s}{2\kappa_{\perp} \sin \zeta_s} \left\{ \sin \zeta_* \left[\sqrt{\frac{1 + \cos \zeta_*}{2}} - \sqrt{\frac{\cos \zeta_* - \cos \zeta_s}{2}} \right] + \sigma \ln \frac{\tan \frac{\zeta_s}{2}}{\tan \frac{\zeta_*}{2}} \right\} \end{aligned}$$

where $\sigma = 2r_s \kappa_{\perp} / (wm\kappa_{\parallel} b_r^2)$. At the O-point, the magnetic field lines have no radial inclination thus the transport is dominated by perpendicular heat conduction, which leads us to determine κ_{\perp} from the temperature change for a path beginning at the O-point:

$$0 < \zeta_* < \zeta_s \longrightarrow 0 : \Delta_0 T \approx -\frac{wq_s}{2\kappa_{\perp}} \implies \kappa_{\perp} \approx \frac{wq_s}{2|\Delta_0 T|_{\text{exp}}}$$

Considering a reference point $\zeta_s = \frac{\pi}{2}$, the total temperature change between this point and the terminal point of the associated heat flux on the separatrix is given as:

$$\frac{\Delta T}{\Delta_0 T} \approx \sin \zeta_* \left(\sqrt{\frac{1 + \cos \zeta_*}{2}} - \sqrt{\frac{\cos \zeta_*}{2}} \right) - \sigma \ln \tan \frac{\zeta_*}{2}$$

$\Delta T/\Delta_0 T$ obtained from experimentally observed temperature profiles, gives us σ_{exp} , from which the parallel heat conductivity can be obtained $\kappa_{\parallel} \approx (2r_s \kappa_{\perp}/w m b_r^2 \sigma_{exp})$. The field line length for the corresponding optimal path is given as:

$$L = \int_{\zeta_*}^{\zeta_s} \frac{B}{B_r} \frac{dr}{d\zeta} d\zeta = \frac{w}{4\sqrt{2}b_r} \int_{\zeta_*}^{\zeta_s} \frac{d\zeta}{(\cos \zeta - \cos \zeta_s)^{1/2}} \approx 0.38(0.4) \frac{w}{b_r}$$

Thus the heat flux limit ξ_{FS} , can be obtained from:

$$\begin{aligned} \xi_{FS} &\approx \frac{3.16}{\kappa_{\parallel}^{SH}/\kappa_{\parallel} - 1} \frac{\lambda}{T} \frac{\Delta_{\parallel} T}{L} \\ &\approx \frac{\kappa_{\parallel}}{nV_e T} \frac{\Delta_{\parallel} T}{L} \approx \frac{\frac{2r_s \kappa_{\perp}}{w m b_r^2 \sigma_{exp}}}{nV_e T} \frac{0.23 \Delta_s T}{0.38 \frac{w}{b_r}} \end{aligned}$$

B.2 Extension of fitzpatrick's model

Heat conduction equation in the presence of an island of width w , critical width w_c , in the X, ζ space can be written as:

$$\frac{1}{4} \left\{ \left[\left(\frac{w}{w_c} \right)^2 \sin \varsigma \frac{\partial}{\partial X} + X \frac{\partial}{\partial \zeta} \right] \times \left[g_{\parallel} \left[\left(\frac{w}{w_c} \right)^2 \sin \varsigma \frac{\partial \tilde{T}}{\partial X} + X \frac{\partial \tilde{T}}{\partial \zeta} \right] \right] \right\} + \frac{\partial^2 \tilde{T}}{\partial X^2} = -\frac{Q w_c^2}{16 \kappa_{\perp}}$$

With the introduction of $y = \frac{2x}{w} = \frac{w_c}{2w} X$, this equation becomes:

$$\kappa_{\parallel} b_r^2 \left[\left(\sin \varsigma \frac{\partial}{\partial y} + 4y \frac{\partial}{\partial \zeta} \right) \times \left[g_{\parallel} \left(\sin \varsigma \frac{\partial \tilde{T}}{\partial y} + 4y \frac{\partial \tilde{T}}{\partial \zeta} \right) \right] \right] + \kappa_{\perp} \frac{\partial^2 \tilde{T}}{\partial y^2} = -\frac{w^2 Q_0}{4} \delta(y)$$

In the limit of large island, i.e. $\kappa_{\parallel} \rightarrow \infty$, this equation can be written as:

$$\left(\sin \varsigma \frac{\partial}{\partial y} + 4y \frac{\partial}{\partial \zeta} \right) g_{\parallel} \left(\sin \varsigma \frac{\partial \tilde{T}}{\partial y} + 4y \frac{\partial \tilde{T}}{\partial \zeta} \right) = 0$$

Since the temperature in the large island limit should be function of the flux surface Ω , the solution of the above equation in this limit can be written in the form:

$$\tilde{T} = T_0 y^2 + T_1 \cos \varsigma$$

Substituting this solution into the heat conduction equation gives:

$$\sin \varsigma \frac{\partial \tilde{T}}{\partial y} + 4y \frac{\partial \tilde{T}}{\partial \zeta} = 2T_0 y \sin \varsigma - 4T_1 y \sin \varsigma = 0 \Rightarrow T_1 = \frac{T_0}{2}$$

$$\tilde{T} = T_0 y^2 + \frac{T_0}{2} \cos \varsigma = T_0 \left(y^2 + \frac{\cos \varsigma}{2} \right) = \frac{T_0}{2} \Omega$$

The presence of heating and finite κ_{\perp} is taken into account by introducing an additional term, dependent on y, ζ as follows:

$$\tilde{T} = T_0 \left(y^2 + \frac{\cos \varsigma}{2} \right) + \Theta(y) \Psi(\varsigma)$$

The function $\Psi(\zeta)$ and boundary condition for $\Theta(y)$ at the RS $y = 0$ follow from integration of the heat conduction equation over a radially thin layer around the resonant surface, or from 4.21:

$$\begin{aligned} (\kappa_{\perp} + \kappa_{\parallel} b_r^2 \sin^2 \varsigma) \frac{\partial \tilde{T}}{\partial y} (0) &= -\frac{w q_{rs}}{2} \\ (\kappa_{\perp} + \kappa_{\parallel} b_r^2 \sin^2 \varsigma) \Psi(\varsigma) \frac{d\Theta}{dy} (0) &= -\frac{w q_{rs}}{2} \Rightarrow \\ \Psi(\varsigma) &= \frac{w q_{rs}}{2 (\kappa_{\perp} + \kappa_{\parallel} b_r^2 \sin^2 \varsigma)}, \frac{d\Theta}{dy} (0) = -1 \end{aligned}$$

Beyond the heating layer, there is no considerable source of heat and the heat conduction equation can be written as follows:

$$\left(\sin \varsigma \frac{\partial}{\partial y} + 4y \frac{\partial}{\partial \varsigma} \right) g_{\parallel} \left(\sin \varsigma \frac{\partial \tilde{T}}{\partial y} + 4y \frac{\partial \tilde{T}}{\partial \varsigma} \right) + \frac{\kappa_{\perp}}{\kappa_{\parallel} b_r^2} \frac{\partial^2 \tilde{T}}{\partial y^2} = 0$$

where we introduce $\sigma = \frac{\kappa_{\perp}}{\kappa_{\parallel} b_r^2}$, and thus obtain the form:

$$\left(\sin \varsigma \frac{\partial}{\partial y} + 4y \frac{\partial}{\partial \varsigma} \right) g_{\parallel} \left(\sin \varsigma \frac{\partial}{\partial y} + 4y \frac{\partial}{\partial \varsigma} \right) \frac{\Theta}{\sigma + \sin^2 \varsigma} + \frac{4T_0 \kappa_{\perp}}{w q_{rs}} = 0$$

$$\left(\sin \varsigma \frac{\partial}{\partial y} + 4y \frac{\partial}{\partial \varsigma} \right) \frac{g_{\parallel} \sin \varsigma}{\sigma + \sin^2 \varsigma} \left(\frac{d\Theta}{dy} - \frac{8 \cos \varsigma}{\sigma + \sin^2 \varsigma} y \Theta \right) + \frac{4T_0 \kappa_{\perp}}{w q_{rs}} = 0$$

Integrating in ζ -direction over one complete phase \Rightarrow terms after $\frac{\partial}{\partial \zeta}$ lead to zero contribution \Rightarrow :

$$\frac{\partial}{\partial y} \left(\frac{d\Theta}{dy} \int_{\pi}^{2\pi} \frac{g_{\parallel} \sin^2 \varsigma}{\sigma + \sin^2 \varsigma} d\varsigma - 8y\Theta \int_{\pi}^{2\pi} \frac{g_{\parallel} \sin^2 \varsigma \cos \varsigma}{(\sigma + \sin^2 \varsigma)^2} d\varsigma \right) + \frac{4\pi T_0 \kappa_{\perp}}{w q_{rs}} = 0$$

The metric coefficient g_{\parallel} , the distance between path border of a heat transport path is given by the following consideration:

$$\Omega = y^2 + \frac{\cos \varsigma}{2}$$

$$y = -\sqrt{\Omega - \frac{\cos \zeta}{2}}$$

$$y_x \equiv \frac{dy}{d\zeta} = -\frac{\sin \zeta}{4\sqrt{\Omega - \frac{\cos \zeta}{2}}} = -\frac{\sin \zeta}{4y}$$

$$g_{\parallel} = \frac{\frac{w}{2} dy}{\sqrt{\left(\frac{r}{m} d\zeta\right)^2 + \left(\frac{w}{2} dy\right)^2}} = \frac{y_x}{\sqrt{\left(\frac{2r}{mw}\right)^2 + y_x^2}} = -\frac{\sin \zeta}{\sqrt{\left(\frac{8r}{mw} y\right)^2 + \sin^2 \zeta}}$$

Substituting g_{\parallel} thus obtained, into the heat conduction equation beyond the heating layer, as obtained above, gives:

$$\int_{\pi}^{2\pi} \frac{g_{\parallel} \sin^2 \zeta \cos \zeta}{(\sigma + \sin^2 \zeta)^2} d\zeta = -\int_{\pi}^{2\pi} \frac{\sin^3 \zeta}{\sqrt{\left(\frac{8r}{mw} y\right)^2 + \sin^2 \zeta} (\sigma + \sin^2 \zeta)^2} d\sin \zeta = 0$$

$$\begin{aligned} \int_{\pi}^{2\pi} \frac{g_{\parallel} \sin^2 \zeta}{\sigma + \sin^2 \zeta} d\zeta &= -\int_{\pi}^{2\pi} \frac{\sin^3 \zeta d\zeta}{\sqrt{\left(\frac{8r}{mw} y\right)^2 + \sin^2 \zeta} (\sigma + \sin^2 \zeta)} \\ &= -2 \int_{\frac{3\pi}{2}}^{\pi} \frac{\sin^3 \zeta d\zeta}{\sqrt{\left(\frac{8r}{mw} y\right)^2 + \sin^2 \zeta} (\sigma + \sin^2 \zeta)} \\ &= 2 \int_{\frac{3\pi}{2}}^{\pi} \frac{\sin^2 \zeta}{\sqrt{\left(\frac{8r}{mw} y\right)^2 + \sin^2 \zeta} (\sigma + \sin^2 \zeta)} d\cos \zeta \\ &= 2 \int_0^1 \frac{(1 - \xi^2) d\xi}{\sqrt{\left(\frac{8r}{mw} y\right)^2 + 1 - \xi^2} (\sigma + 1 - \xi^2)} = 2\gamma(y, \alpha) \end{aligned}$$

$$\frac{\partial}{\partial y} \left[\frac{d\Theta}{dy} \gamma(y, \alpha) \right] = -\frac{2\pi T_0 \kappa_{\perp}}{w q_{rs}}$$

$$\frac{d\Theta}{dy} \gamma(y, \alpha) = -\gamma(0, \alpha) - \frac{2\pi T_0 \kappa_{\perp}}{w q_{rs}} y$$

$$\frac{d\Theta}{dy} = -\frac{\gamma(0, \alpha)}{\gamma(y, \alpha)} - \frac{2\pi T_0 \kappa_{\perp}}{w q_{rs}} \frac{y}{\gamma(y, \alpha)}$$

$$\Theta = \Theta(0) - \int_0^y \frac{\gamma(0, \alpha)}{\gamma(y, \alpha)} dy - \frac{2\pi T_0 \kappa_{\perp}}{w q_{rs}} \int_0^y \frac{y dy}{\gamma(y, \alpha)}$$

$$\Theta(1) = 0 \implies \Theta(0) = \int_0^1 \frac{\gamma(0, \alpha)}{\gamma(y, \alpha)} dy + \frac{2\pi T_0 \kappa_{\perp}}{wq_{rs}} \int_0^1 \frac{y dy}{\gamma(y, \alpha)}$$

$$\Theta = \int_y^1 \frac{\gamma(0, \alpha)}{\gamma(y, \alpha)} dy + \frac{2\pi T_0 \kappa_{\perp}}{wq_{rs}} \int_y^1 \frac{y dy}{\gamma(y, \alpha)}$$

Total solution for the temperature perturbation, substituting $\Psi(\zeta)$ and $\Theta(y)$, back into the assumed form of \tilde{T} , i.e. the solution for the heat conduction equation, gives:

$$\tilde{T} = T_0 \left(y^2 + \frac{\cos \varsigma}{2} \right) + \frac{1}{1 + \frac{\sin^2 \varsigma}{\sigma}} \left(\frac{wq_{rs}}{2\kappa_{\perp}} \int_y^1 \frac{\gamma(0, \alpha)}{\gamma(y, \alpha)} dy + \pi T_0 \int_y^1 \frac{y dy}{\gamma(y, \alpha)} \right)$$

$$\theta_0(y, \alpha) = \int_y^1 \frac{\gamma(0, \alpha)}{\gamma(y, \alpha)} dy, \theta_1(y, \alpha) = \int_y^1 \frac{y dy}{\gamma(y, \alpha)}$$

$$\gamma(y, \alpha) = \int_0^1 \frac{(1 - \xi^2) d\xi}{\sqrt{\left(\frac{8r}{mw}y\right)^2 + 1 - \xi^2 (\sigma + 1 - \xi^2)}}$$

$$\tilde{T} = T_0 \left(y^2 + \frac{\cos \varsigma}{2} \right) + \frac{\frac{wq_{rs}}{2\kappa_{\perp}} \theta_0 + \pi T_0 \theta_1}{1 + \frac{\sin^2 \varsigma}{\sigma}}$$

$$T_{\kappa} = \frac{wq_{rs}}{2\kappa_{\perp}} \theta_0 + \pi T_0 \theta_1$$

Temperature perturbation at RS, for different values of $\Omega = -0.8, -0.4, 0, 0.4$, can be written in the following way:

$$\tilde{T}_{-0.8} = -0.4T_0 + \frac{T_{\kappa}}{1 + \frac{0.36}{\sigma}}$$

$$\tilde{T}_{-0.4} = -0.2T_0 + \frac{T_{\kappa}}{1 + \frac{0.84}{\sigma}}$$

$$\tilde{T}_0 = \frac{T_{\kappa}}{1 + \frac{1}{\sigma}}$$

$$\tilde{T}_{0.4} = 0.2T_0 + \frac{T_{\kappa}}{1 + \frac{0.84}{\sigma}}$$

By manipulation of the above equations $T_0, \kappa_{\perp}, \sigma \rightarrow \kappa_{||}$, can be determined as shown below, where $\Delta_{a,b} = \tilde{T}_a - \tilde{T}_b$:

$$T_0 = -2.5\Delta_{-0.4,0.4}$$

$$\begin{aligned} \frac{(\Delta_{-0.8,0} - \Delta_{-0.4,0.4})(\sigma + 0.36)(\sigma + 1)}{0.64\sigma} &= T_\kappa \\ \frac{(\Delta_{-0.8,0.4} - 1.5\Delta_{-0.4,0.4})(\sigma + 0.36)(\sigma + 0.84)}{0.48\sigma} &= T_\kappa \\ \sigma &= \frac{\Delta_{-0.8,0} - 1.12\Delta_{-0.8,0.4} + 0.68\Delta_{-0.4,0.4}}{1.333\Delta_{-0.8,0.4} - \Delta_{-0.4,0.4} - \Delta_{-0.8,0}} \\ \kappa_\perp &\approx \frac{0.32\theta_0(0) wq_{rs}}{(\Delta_{-0.8,0} - \Delta_{-0.4,0.4})(\sigma + 1.36 + 0.36/\sigma) + 5\theta_1(0)\Delta_{-0.4,0.4}} \end{aligned}$$

Determination of $\frac{1}{L_T} = \frac{1}{T} \left| \frac{\delta\tilde{T}}{l} \right|$. The temperature perturbation $\delta\tilde{T}$ along a field line $\Omega = \text{constant}$, considering the contribution from the θ_1 term to be small, can be give as:

$$\begin{aligned} \tilde{T} &= T_0 \left(y^2 + \frac{\cos \zeta}{2} \right) + \frac{\frac{wq_{rs}}{2\kappa_\perp} \theta_0 + \pi T_0 \theta_1}{1 + \frac{\sin^2 \zeta}{\sigma}} \\ \delta\tilde{T} &\approx \frac{wq_{rs} [\theta_0(0) - \theta_0(0.5)]}{2\kappa_\perp \left(1 + \frac{1}{\sigma} \right)} \end{aligned}$$

The corresponding length of the field line l and hence the L_T can be given as:

$$\begin{aligned} dl &\approx \frac{w}{2} \frac{dy}{b_r \sin \zeta} \Rightarrow l \approx \frac{w}{2b_r} \int_0^{0.5} \frac{dy}{\sqrt{1-4y^2}} \approx \frac{0.53w}{2b_r} \\ \frac{1}{L_T} &\approx \frac{1.42\theta_0(0) q_{rs} b_r}{\kappa_\perp \left(1 + \frac{1}{\sigma} \right)} \approx \frac{1.42\theta_0(0) q_{rs} b_r}{(\sigma + 1) \kappa_\parallel b_r T} \end{aligned}$$

Substituting the parameters obtained above in the expression for the heat flux limit ξ , gives:

$$\begin{aligned} \xi &\approx \frac{3.16\kappa_\parallel}{\kappa_\parallel^{SH}} \frac{\lambda}{L_T} \approx \frac{3.16\lambda}{\kappa_\parallel^{SH}} \frac{1.42q_{rs}\theta_0^0}{(\sigma + 1) b_r T} = \frac{1.42q_{rs}\theta_0^0}{(\sigma + 1) nV_{th} T b_r} \\ &= \frac{1.42 \cdot 2\theta_0^0 P_{ECRH}}{(\sigma + 1) \pi^2 s_s n V_{th} T w^2} = \frac{0.14\theta_0^0}{\sigma + 1} \frac{P_{ECRH}^{MW}}{n_{13} T_{kev}^{1.5} w^2} \end{aligned}$$

Appendix C

ELMs

C.1 Discretized equations for the model of ion convective heat loss

C.1.1 Equations in dimensionless variables

It is useful to define certain dimensionless variables to write the kinematic, motion and energy equation in a simplified form, and also to express them in terms of important parameters at the barrier top:

$$\tau_1(x) \sim \frac{\left(\frac{m_i V^2}{2} + \varepsilon\right)^{3/2}}{n(x)} \Rightarrow \tau_1(x) = \tau_1^b \frac{(u^2 + \xi)^{1.5}}{\eta(\zeta)}, \lambda_b = \tau_1^b V_T^b$$

$$\tau_1^b = 6.5 \cdot 10^5 \frac{\sqrt{A_i} T_b^{1.5}}{n_b}, \lambda_b = 9 \times 10^{11} \frac{T_b^2}{n_b}$$

$$\omega = \frac{t}{\tau_1^b}, \varkappa = \frac{e \Delta_b E}{T_b \alpha(x)}, v = \frac{V}{V_T^b}, \xi = \frac{\varepsilon}{T_b}$$

$$x = a - r; \zeta = x / \Delta_b; S_{sep} = 4\pi^2 \kappa a R$$

$$\mu = \frac{2}{\sqrt{\pi}} \int_0^\chi e^{-y} \sqrt{y} dy = erf(\sqrt{\chi}) - \frac{2}{\sqrt{\pi}} e^{-\chi} \sqrt{\chi}, \mu' = \frac{2}{\sqrt{\pi}} e^{-\chi} \sqrt{\chi}, \chi = \frac{v^2 + \zeta}{\theta(\zeta)}$$

$$\nu^* \equiv qR (R/a)^{3/2} / \lambda_b, \nu_0 = (1.9\alpha qR / \Delta_b) (R/a)^{3/2}$$

Here b indicates the value at the barrier top. τ_1 is the characteristic collision time, λ is the mean free path between collisions, μ is the Maxwell integral and ν^* is the plasma collisionality.

The kinematic, motion and energy equation can be written respectively, in terms of dimensionless variables and their discretized form, to solve them numerically with a finite difference scheme, as follows:

$$\begin{aligned} \frac{d\varsigma}{d\omega} &= \frac{u\lambda_b\alpha(\varsigma)}{\Delta_b} = v_\alpha u \\ \frac{\varsigma_{i+1} - \varsigma_i}{\Delta\omega} &= v_\alpha u_i \Rightarrow \varsigma_{i+1} = \varsigma_i + v_\alpha u_i \Delta\omega \\ \frac{du}{d\omega} &= \frac{\lambda_b\alpha(\varsigma)}{2\Delta_b} \kappa(\varsigma) - \frac{2\mu\eta(\varsigma)}{(u^2 + \xi)^{1.5}} u = e - gu \\ \frac{u_{i+1} - u_i}{\Delta\omega} &= e - gu_{i+1} \Rightarrow u_{i+1} = \frac{u_i + e\Delta\omega}{1 + g\Delta\omega} \\ \frac{d\xi}{d\omega} &= \frac{2\eta(\varsigma)}{(u^2 + \xi)^{1.5}} \left[(\mu + \mu') u^2 - (\mu - \mu') \xi \right] = v_l u^2 - v_d \xi \\ \frac{\xi_{i+1} - \xi_i}{\Delta\omega} &= v_l u^2 - v_d \xi_{i+1} \Rightarrow \xi_{i+1} = \frac{\xi_i + v_l u_i^2 \Delta\omega}{1 + v_d \Delta\omega} \end{aligned}$$

C.1.2 Profiles

Piecewise linear parameter profiles in ETB can be written as:

$$\begin{aligned} \eta(\varsigma) &= \eta_s + (1 - \eta_s) \min(1, \varsigma) + (\eta_e - 1) \max(0, \varsigma - 1) \frac{\Delta_b}{\Delta_e}; \eta_{s,e} = \frac{n_{s,e}}{n_b} \\ \theta(\varsigma) &= \theta_s + (1 - \theta_s) \min(1, \varsigma) + (\theta_e - 1) \max(0, \varsigma - 1) \frac{\Delta_b}{\Delta_e}; \theta_{s,e} = \frac{T_{s,e}}{T_b} \end{aligned}$$

C.1.3 Electric field

The electric field can be obtained from the force balance equation for electrons along field lines for a static condition:

$$\begin{aligned} 0 &= -enE_{\parallel} - \alpha \frac{d(nT)}{dr} \\ eE_{\parallel} &= -\frac{1}{n} \alpha \frac{d(nT)}{dr} \\ F_e &= -\frac{\alpha}{\eta n_b \Delta_b} \frac{d(n_b T_b \eta \theta)}{d\varsigma} \end{aligned}$$

Since the n, T profiles are piecewise linear, depending on the radial position characterised by ς , there are two forms for the equation for the electric field F_e :

$$\varsigma > 1$$

$$\begin{aligned} F_e &= -\frac{T_b \alpha}{\eta \Delta_b} \frac{d}{d\varsigma} \left[(1 + (\eta_e - 1)(\varsigma - 1) \frac{\Delta_b}{\Delta_e}) (1 + (\theta_e - 1)(\varsigma - 1) \frac{\Delta_b}{\Delta_e}) \right] \\ F_e &= -\frac{T_b \alpha}{\eta \Delta_b} \left[(\eta_e + \theta_e - 2) \frac{\Delta_b}{\Delta_e} + 2(\varsigma - 1)(\eta_e - 1)(\theta_e - 1) \left(\frac{\Delta_b}{\Delta_e} \right)^2 \right] \end{aligned}$$

$\varsigma < 1$

$$F_e = -\frac{T_b \alpha}{\eta \Delta_b} \frac{d}{d\varsigma} [(\eta_s + (1 - \eta_s)\varsigma)(\theta_s + (1 - \theta_s)\varsigma)]$$

$$F_e = -\frac{T_b \alpha}{\Delta_b} \left[1 - \theta_s + (1 - \eta_s) \frac{\theta_s + \varsigma(1 - \theta_s)}{\eta_s + \varsigma(1 - \eta_s)} \right]$$

The net energy loss due to ion convection, normalised to the pedestal energy content $W_{ped} = S_{sep} a / 2 \times 3n_b T_b$ is given as:

$$\frac{\Delta W_{elm}^{conv}}{W_{ped}} = \frac{\Delta_b}{a} \frac{1 + \kappa}{\sqrt{\pi \kappa}} \int_{-1 - \Delta_b / \Delta_e}^0 \frac{\eta(\varsigma)}{\theta^{3/2}(\varsigma)} d\varsigma \int_{-u_{max}}^{u_{max}} du \int_{-\xi_{max}}^{\xi_{max}} d\xi \exp \left[-\frac{u^2 + \xi}{\theta(\varsigma)} \right] (u_0^2 + \xi_0)$$

C.2 Discretized equations for time evolution of n, T and α_{elm}

Discretized equations for time evolution of n, T and α_{elm} , to solve them numerically using a finite difference scheme, are given below:

Discretized equation for density n_b :

$$\frac{\Delta_b + \Delta_e}{2} \frac{n_{b_{i+1}} - n_{b_i}}{\Delta t} = j_0 - D_{\perp} \frac{n_{b_{i+1}} - n_s}{\Delta_b} - \alpha \Gamma_{\parallel i}^s$$

$$n_{b_{i+1}} = \left(j_0 + \frac{D_{\perp} n_s}{\Delta_b} - \alpha \Gamma_{\parallel i}^s + n_{b_i} \frac{\Delta_b + \Delta_e}{2\Delta t} \right) / \left(\frac{\Delta_b + \Delta_e}{2\Delta t} + \frac{D_{\perp}}{\Delta_b} \right)$$

Discretized equation for the parallel particle flux Γ_{\parallel} :

$$\frac{\Delta_b}{2} \frac{\Gamma_{\parallel i+1}^s - \Gamma_{\parallel i}^s}{\Delta t} = \alpha \left[2 \frac{T_e n_e - T_s n_s}{m_i} - \frac{(\Gamma_{\parallel i}^s)^2}{n_s} \right]$$

$$\Gamma_{\parallel i+1}^s = \frac{2\alpha \Delta t}{\Delta_b} \left[2 \frac{T_e n_e - T_s n_s}{m_i} - \frac{(\Gamma_{\parallel i}^s)^2}{n_s} \right] + \Gamma_{\parallel i}^s$$

Discretized equation for T_b :

$$\begin{aligned} & \left[\frac{\Delta_b n_s + \Delta_e n_e}{2} + (\Delta_b + \Delta_e) n_{b_{i+1}} \right] \frac{T_{b_{i+1}} - T_{b_i}}{\Delta t} + \\ & + \left[\frac{\Delta_b T_s + \Delta_e T_e}{2} + (\Delta_b + \Delta_e) T_{b_{i+1}} \right] \frac{n_{b_{i+1}} - n_{b_i}}{\Delta t} \\ = & q_{core} - j_0 E_i - 3D_{\perp} \frac{n_{b_{i+1}} - n_s}{\Delta_b} T_s - \kappa_{\perp} \frac{T_{b_{i+1}} - T_s}{\Delta_b} - q_s^s \end{aligned}$$

$$\begin{aligned}
& \frac{T_{b_{i+1}}}{\Delta t} \left[\frac{\Delta_b n_s + \Delta_e n_e}{2} + \frac{\kappa_{\perp} \Delta t}{\Delta_b} + (\Delta_b + \Delta_e) (2n_{b_{i+1}} - n_{b_i}) \right] \\
& = q_{core} - j_0 E_i - 3D_{\perp} \frac{n_{b_{i+1}} - n_s}{\Delta_b} T_s + \kappa_{\perp} \frac{T_s}{\Delta_b} - q_s^s \\
& + \frac{T_{b_i}}{\Delta t} \left[\frac{\Delta_b n_s + \Delta_e n_e}{2} + (\Delta_b + \Delta_e) n_{b_{i+1}} \right] - \frac{(n_{b_{i+1}} - n_{b_i})(\Delta_b T_s + \Delta_e T_e)}{2\Delta t}
\end{aligned}$$

Discretized equations for time evolution of α_{elm}

$$\begin{aligned}
\frac{\eta_{i+1} - \eta_i}{\Delta \tau} &= \xi \left[\sigma - \frac{\xi \alpha_i^2}{\delta \xi \alpha_i + \sqrt{\eta_i \Theta(\eta_i)}} \right] \\
\frac{\alpha_{i+1} - \alpha_i}{\Delta \tau} &= \alpha_i \left[\sqrt{\eta_i \Theta(\eta_i)} - \frac{\Theta(-\eta_i)}{\tau_{ELM}} \right]
\end{aligned}$$

C.3 Simple model for ballooning modes

Perturbations:

$$\tilde{n} \sim \tilde{\varphi} \sim \tilde{j} \sim \tilde{B}_r \sim f(l = qR\vartheta) \cdot \exp(-i\omega t + ik y)$$

Continuity equation:

$$\begin{aligned}
\frac{\partial \tilde{n}}{\partial t} + \frac{dn}{dr} \tilde{V}_E &= 0 \\
\tilde{V}_E = c \frac{\tilde{E}_y}{B} &= c \frac{-ik \tilde{\varphi}}{B} \\
-i\omega \tilde{n} + c \frac{-ik \tilde{\varphi}}{B} \frac{dn}{dr} &= 0 \\
\omega_* = \frac{cTk}{eBL_n}, \frac{1}{L_n} &= -\frac{1}{n} \frac{dn}{dr} \\
\hat{n} = \frac{\tilde{n}}{n}, \hat{\varphi} = \frac{e\tilde{\varphi}}{T} \\
\hat{\varphi} &= \frac{\omega}{\omega_*} \hat{n}
\end{aligned}$$

Momentum equation:

$$\begin{aligned}
m_i n \frac{\partial \vec{V}_i}{\partial t} + \vec{\nabla} P &= \frac{[\vec{j} \times \vec{B}]}{c} \\
[\vec{j} \times \vec{B}] &= \begin{array}{ccc} \vec{e}_r & \vec{e}_{\vartheta} & \vec{e}_{\parallel} \\ j_r & j_y & 0 \\ 0 & 0 & B \end{array} = B (j_y \vec{e}_r - j_r \vec{e}_y)
\end{aligned}$$

poloidal component:

$$\frac{\partial \tilde{P}}{\partial y} = -\tilde{j}_r \frac{B}{c}$$

$$ik2\tilde{n}T_e = -\tilde{j}_r \frac{B}{c} \implies \tilde{j}_r = -in \frac{2cTk}{B} \hat{n}$$

radial component:

$$m_i n \frac{\partial \tilde{V}_E}{\partial t} = \tilde{j}_y \frac{B}{c}$$

$$-i\omega m_i n c \frac{-ik\tilde{\varphi}}{B} = \tilde{j}_y \frac{B}{c}$$

$$\tilde{j}_y = -\omega n \frac{cT}{B} \frac{k\tilde{\varphi}}{\omega_{ci}}$$

Zero current divergency:

$$\vec{\nabla} \cdot \vec{j} = 0 : \nabla_{\parallel} \tilde{j}_{\parallel} = -\frac{\partial \tilde{j}_r}{\partial r} - \frac{\partial \tilde{j}_y}{\partial y}$$

$$\tilde{j}_r \sim \frac{1}{B^2} \sim \left(1 + \frac{r \cos \vartheta}{R}\right)^2 \implies$$

$$\frac{\partial \tilde{j}_r}{\partial r} \approx j_r \frac{2 \cos \vartheta}{R} = -in \frac{4cTk}{RB} \cos \vartheta \hat{n}$$

$$\frac{\partial \tilde{j}_y}{\partial y} = -i\omega n \frac{cT}{B} \frac{k^2 \tilde{\varphi}}{\omega_{ci}} = -i\omega^2 n \frac{cT}{B} \frac{k^2}{\omega_{ci} \omega_*} \hat{n}$$

$$\nabla_{\parallel} = \frac{1}{qR} \frac{\partial}{\partial \vartheta}$$

$$\frac{1}{qR} \frac{\partial \tilde{j}_{\parallel}}{\partial \vartheta} = in \frac{cT}{B} k^2 \left(\frac{4}{kR} \cos \vartheta \hat{n} + \frac{\omega}{\omega_{ci}} \tilde{\varphi} \right)$$

$$\frac{1}{qR} \frac{\partial \tilde{j}_{\parallel}}{\partial \vartheta} = in \frac{cT}{B} k^2 \left(\frac{4}{kR} \cos \vartheta + \frac{\omega^2}{\omega_{ci} \omega_*} \right) \hat{n}$$

$$\frac{1}{qR} \frac{\partial \tilde{j}_{\parallel}}{\partial \vartheta} = in \frac{cT L_n}{BR^2} k \left(\frac{4R}{L_n} \cos \vartheta + \omega^2 \frac{R^2}{c_s^2} \right) \hat{n}$$

where $c_s = \sqrt{T/m_i}$ is the ion sound speed

Parallel component of Maxwell equation $\vec{\nabla} \times \vec{B} = \frac{4\pi}{c} \vec{j}$:

$$-ik\tilde{B}_r = \frac{4\pi}{c} \tilde{j}_{\parallel} \implies \tilde{B}_r = i \frac{4\pi}{kc} \tilde{j}_{\parallel}$$

Radial component of Maxwell equation $\vec{\nabla} \times \vec{E} = -\frac{1}{c} \frac{\partial \vec{B}}{\partial t}$:

$$ik\tilde{E}_{||} - \nabla_{||}\tilde{E}_y = i\frac{\omega}{c}\tilde{B}_r \implies ik\tilde{E}_{||} - \frac{1}{qR} \frac{\partial(-ik\tilde{\varphi})}{\partial\vartheta} = i\frac{\omega}{c}\tilde{B}_r \implies \tilde{E}_{||} = i\frac{4\pi\omega}{k^2c^2}\tilde{j}_{||} - \frac{1}{qR} \frac{\partial\tilde{\varphi}}{\partial\vartheta}$$

Low collisionality \implies high electric conductivity $\implies E_{||} = 0 \implies$

$$\begin{aligned}\tilde{j}_{||} &= -i\frac{k^2c^2}{4\pi\omega qR} \frac{\partial\tilde{\varphi}}{\partial\vartheta} = -i\frac{k^2c^2T}{4\pi e\omega qR} \frac{\partial\hat{\varphi}}{\partial\vartheta} = -i\frac{kcBL_n}{4\pi qR} \frac{\partial\hat{n}}{\partial\vartheta} \\ \tilde{B}_r &= \frac{kcT}{e\omega qR} \frac{\partial\hat{\varphi}}{\partial\vartheta} = B\frac{L_n}{qR} \frac{\partial\hat{n}}{\partial\vartheta}\end{aligned}$$

Equation for \hat{n}

$$\begin{aligned}\frac{\partial^2\hat{n}}{\partial\vartheta^2} + \frac{4\pi nT}{B^2}q^2 \left(\frac{4R}{L_n} \cos\vartheta + \omega^2 \frac{R^2}{c_s^2} \right) \hat{n} &= 0 \\ \frac{d^2f}{d\vartheta^2} + \frac{\beta}{2}q^2 \left(\frac{4R}{L_n} \cos\vartheta + \omega^2 \frac{R^2}{c_s^2} \right) f &= 0\end{aligned}$$

where

$$\beta = \frac{8\pi nT}{B^2}$$

with new variable $z = \frac{\pi-\vartheta}{2}$ we get canonical form of Mathieu equation:

$$\frac{d^2f}{d\vartheta^2} + (a - 2p \cos 2z) f = 0$$

with

$$\begin{aligned}a &= 2\beta q^2 \omega^2 \frac{R^2}{c_s^2} \\ p &= 4\beta q^2 \frac{R}{L_n}\end{aligned}$$

Ballooning modes with the maximum of density perturbation at the low field side correspond to the even Mathieu of the second order, $ce_2(z, p)$, with approximate dispersion relation between eigen values:

$$a = \frac{128 + 40p - 2p^2}{32 + p}$$

Instability frequency:

$$\omega = \frac{c_s}{2qR} \sqrt{\frac{a}{\beta}} = \frac{c_s}{2qR} \sqrt{\frac{128 + 40p - 2p^2}{\beta(32 + p)}}$$

Instability threshold:

$$\begin{aligned} 128 + 40p - 2p^2 &= 0 \\ p^2 - 20p - 64 &= 0 \end{aligned}$$

$$p_{cr} = 10 + \sqrt{100 + 64} \approx 23$$

$$\beta_{cr} \approx \frac{23}{4} \frac{L_n}{q^2 R}$$

$$\frac{8\pi q^2 R}{B^2} \left[\frac{nT}{L_n} \right]_{cr} = \frac{23}{4} = 5.75$$

Growth rate close to the threshold:

$$\mathbf{Im}\omega = \frac{c_s}{2qR} \sqrt{\frac{-\frac{da}{dp}(p_{cr}) \cdot (p - p_{cr})}{\beta}} = \frac{c_s}{2qR} \sqrt{\frac{\frac{4p_{cr}-40}{32+p_{cr}} \cdot (p - p_{cr})}{\beta}}$$

$$\gamma \equiv \mathbf{Im}\omega \approx \frac{1.37c_s}{\sqrt{RL_n}} \sqrt{\frac{\beta - \beta_{cr}}{\beta_{cr}}}$$

C.3.1 Particle losses due to ballooning mode

Perpendicular flux density:

$$\begin{aligned}
\Gamma_{\perp} &= \tilde{n}\tilde{V}_E^* + \tilde{n}_*\tilde{V}_E = \tilde{n} \left(-i\frac{ck}{B}\tilde{\varphi}\right)^* + \tilde{n}_* \left(-i\frac{ck}{B}\tilde{\varphi}\right) \\
&= \frac{cTkn}{eB} [\hat{n}(-i\hat{\varphi})^* + \hat{n}_*(-i\hat{\varphi})] \\
&= \frac{cTkn}{eB} \left[\hat{n} \left(-i\frac{\omega}{\omega_*}\hat{n}\right)^* + \hat{n}_* \left(-i\frac{\omega}{\omega_*}\hat{n}\right) \right] \\
&= 2\gamma n L_n |\hat{n}|^2
\end{aligned}$$

Parallel motion equation:

$$\partial_t \Gamma_{\parallel} + \nabla_{\parallel} \left(\frac{\Gamma_{\parallel}^2}{n} + \frac{2nT}{m_i} \right) = 0$$

Contribution of parallel flow to radial particle flux:

$$\Gamma_{\parallel,r} = \Gamma_{\parallel} \frac{\tilde{B}_r}{B}$$

Equation for $\Gamma_{\parallel,r}$

$$\Gamma_{\parallel,r} \mathbf{Re}\omega + \left(\frac{\tilde{B}_r}{B} \right)^2 \frac{\partial}{\partial r} \left(\frac{\Gamma_{\parallel,r}^2 B^2}{n \tilde{B}_r^2} + \frac{2nT}{m_i} \right) = 0$$

Integration radially over the region involved into ELM with the width Δ_{ELM} where $\gamma = \mathbf{Re}\omega$ and $\alpha = \sqrt{\left(\frac{\tilde{B}_r}{B}\right)^2}$ are roughly constant, provides equation for the $\Gamma_{\parallel,r}$ value at the separatrix, Γ_s :

$$\Gamma_s \frac{\Delta_{ELM}}{2} \gamma + \frac{\Gamma_s^2}{n_s} - \frac{2n_b T_b}{m_i} \alpha^2 \varsigma = 0$$

with

$$\varsigma = \min \left(1, \frac{\Delta_{ELM}}{\Delta_b} \right)$$

and it was taken into account the pressure at barrier top, $2n_b T_b$, is much larger than that at the separatrix, $2n_s T_s$.

$$\Gamma_s^2 + \Gamma_s \frac{\Delta_{ELM}\gamma}{2} n_s - 2n_s n_b c_{sb}^2 \alpha^2 \varsigma = 0$$

where $c_{sb} = \sqrt{T_b/m_i}$. Therefore

$$\Gamma_s = \sqrt{\left(\frac{\Delta_{ELM}\gamma}{4} n_s \right)^2 + 2n_s n_b c_{sb}^2 \alpha^2 \varsigma} - \frac{\Delta_{ELM}\gamma}{4} n_s$$

or by using the approximation $\sqrt{1+x} - 1 \approx \frac{x}{2+\sqrt{x}}$ with the maximum error of 25%,

$$\Gamma_s = \frac{2\zeta (c_{sb}\alpha)^2 n_b}{c_{sb}\alpha \sqrt{2\zeta n_b/n_s} + \gamma \Delta_{ELM}/2}$$

Total radial particle flux:

$$\Gamma_r = \Gamma_{\perp} + \Gamma_s \approx 2.74 c_{sb} \sqrt{\zeta} \left(n_s \sqrt{\frac{L_n}{R} \frac{\beta - \beta_{cr}}{\beta_{cr}}} |\hat{n}|^2 + \frac{n_b \alpha^2}{\sqrt{\frac{L_n}{R} \frac{\beta - \beta_{cr}}{\beta_{cr}} \frac{\Delta_{ELM}}{L_n} + 2\sqrt{\frac{n_b}{n_s}} \alpha}} \right)$$

C.3.2 Averaging over poloidal angle

$$\hat{n} = A \cdot ce_2 \left(\frac{\pi - \vartheta}{2} \right)$$

$$\frac{\tilde{B}_r}{B} \frac{qR}{L_n} = \alpha \frac{qR}{L_n} = \frac{\partial \hat{n}}{\partial \vartheta} = A \frac{d}{d\vartheta} ce_2 \left(\frac{\pi - \vartheta}{2} \right)$$

From the above relation we get for the surface averaged value $\langle \dots \rangle = \int_0^{\pi} \dots \frac{d\vartheta}{\pi}$:

$$\alpha^2 \left(\frac{qR}{L_n} \right)^2 = A^2 \left\langle \left[\frac{d}{d\vartheta} ce_2 \left(\frac{\pi - \vartheta}{2} \right) \right]^2 \right\rangle$$

Thus:

$$A = \frac{qR}{L_n} \sqrt{\frac{\langle \alpha^2 \rangle}{\left\langle \left[\frac{d}{d\vartheta} ce_2 \left(\frac{\pi - \vartheta}{2} \right) \right]^2 \right\rangle}}$$

$$\hat{n} = \frac{qR}{L_n} \sqrt{\frac{\langle \alpha^2 \rangle}{\left\langle \left[\frac{d}{d\vartheta} ce_2 \left(\frac{\pi - \vartheta}{2} \right) \right]^2 \right\rangle}} ce_2 \left(\frac{\pi - \vartheta}{2} \right)$$

$$\alpha = \sqrt{\frac{\langle \alpha^2 \rangle}{\left\langle \left[\frac{d}{d\vartheta} ce_2 \left(\frac{\pi - \vartheta}{2} \right) \right]^2 \right\rangle}} \frac{d}{d\vartheta} ce_2 \left(\frac{\pi - \vartheta}{2} \right)$$

and

$$\Gamma_r \approx 2.74 n_b c_{sb} \sqrt{\zeta} \frac{\langle \alpha^2 \rangle}{\left\langle \left[\frac{d}{d\vartheta} ce_2 \left(\frac{\pi - \vartheta}{2} \right) \right]^2 \right\rangle} \times \left\{ \frac{\frac{n_s}{n_b} \left(\frac{qR}{L_n} \right)^2 \sqrt{\frac{L_n}{R} \frac{\beta - \beta_{cr}}{\beta_{cr}}} \left[ce_2 \left(\frac{\pi - \vartheta}{2} \right) \right]^2 + \left[\frac{d}{d\vartheta} ce_2 \left(\frac{\pi - \vartheta}{2} \right) \right]^2}{\sqrt{\frac{L_n}{R} \frac{\beta - \beta_{cr}}{\beta_{cr}} \frac{\Delta_{ELM}}{L_n} + 2\sqrt{\frac{n_b}{n_s}} \sqrt{\frac{\langle \alpha^2 \rangle}{\left\langle \left[\frac{d}{d\vartheta} ce_2 \left(\frac{\pi - \vartheta}{2} \right) \right]^2}} \frac{d}{d\vartheta} ce_2 \left(\frac{\pi - \vartheta}{2} \right)}}} \right\}$$

Parallel flow is effective in the region $0 \leq \vartheta \leq \vartheta_0$ where $\tilde{B}_r \geq 0$; ϑ_0 corresponds to the second optimum (the first one is $\vartheta = 0$) of ce_2 . Therefore

$$\langle \Gamma_r \rangle \approx 2.74 n_b c_{sb} \sqrt{\zeta} \frac{\langle \alpha^2 \rangle}{\left\langle \left[\frac{d}{d\vartheta} ce_2 \left(\frac{\pi - \vartheta}{2} \right) \right]^2 \right\rangle} \times \left\{ \begin{aligned} & \frac{n_s}{n_b} \left(\frac{qR}{L_n} \right)^2 \sqrt{\frac{L_n}{R} \frac{\beta - \beta_{cr}}{\beta_{cr}}} \left\langle \left[ce_2 \left(\frac{\pi - \vartheta}{2} \right) \right]^2 \right\rangle + \\ & + \int_0^{\vartheta_0} \frac{\left[\frac{d}{d\vartheta} ce_2 \left(\frac{\pi - \vartheta}{2} \right) \right]^2 \frac{d\vartheta}{\pi}}{\sqrt{\frac{L_n}{R} \frac{\beta - \beta_{cr}}{\beta_{cr}} \frac{\Delta_{ELM}}{L_n}} + 2 \sqrt{\frac{n_b}{n_s}} \sqrt{\frac{\langle \alpha^2 \rangle}{\left\langle \left[\frac{d}{d\vartheta} ce_2 \left(\frac{\pi - \vartheta}{2} \right) \right]^2 \right\rangle}} \frac{d}{d\vartheta} ce_2 \left(\frac{\pi - \vartheta}{2} \right)} \end{aligned} \right\}$$

$\langle \alpha^2 \rangle = \left\langle \left(\frac{\tilde{B}_r}{B} \right)^2 \right\rangle$ is governed by the equation for the magnetic field perturbation.